Laboratory Constraints on Thermal and Photon-Induced Processes in Interstellar Ices

Ilsa R. Cooke
Waikuku Beach, New-Zealand

Bsc(Hons) Chemistry, University of Otago, 2012

A dissertation presented to the Graduate Faculty
of the University of Virginia in Candidacy for the Degree of

Doctor of Philosophy

Department of Chemistry

University of Virginia
May 2018

Laboratory Constraints on Thermal and Photon-Induced Processes in Interstellar Ices

Abstract

Chemistry in icy mantles condensed on the surface of dust grains is an important route to the molecular complexity observed in the interstellar medium. The molecules that are produced in the ice may be transferred to protoplanetary disks during star-formation, where they could be incorporated into nascent planetary systems. Understanding the fundamental processes in these ices can help us determine the fraction of prebiotic molecules that were delivered to our solar system from interstellar sources, and thereby establish the likelihood of their existence elsewhere in the universe.

Astrochemical models that are used to explain observed abundances of interstellar molecules rely on laboratory measurements to provide the necessary kinetic data. Such models typically implement large chemical kinetics networks and are often limited by the lack of quantitative laboratory data that exist. The work in this thesis aims to provide constraints on various thermal and non-thermal processes at the surface, and within the bulk of astrochemically-relevant ice mantles. Thermal processes in ices include the diffusion, reaction and desorption of atoms and molecules that are thermalized to the dust temperature. Non-thermal processes involve the input of energy; typically from UV-photons, electrons or cosmic rays, that can induce diffusion, reactions or desorption.

In Chapter 3, we provide kinetic data for the formation of CO_2 via the Eley-Rideal reaction between CO(g) and photoproduced OH radicals. This process provides a new route to the formation of CO_2 in warm ice mantles that could be relevant in photon-dominated astrophysical environments. Chapter 4 presents a potential observational constraint on ice composition using the sensitivity of the CO_2 longitudinal optical (LO) phonon modes to the ice mixing

environment. Laboratory spectral measurements like this are especially critical with the upcoming launch of the *James Webb Space Telescope* (JWST), which will improve our understanding of the composition of icy dust grains and their evolution during star formation.

We also highlight the use of CO_2 LO phonons in the laboratory by utilizing their sensitivity to the ice composition to follow CO diffusion into CO_2 ices at low temperature. Coupling the extracted diffusion barrier with measurements of CO desorption from CO_2 ices, we provide the diffusion-desorption barrier ratio for direct input into astrochemical models. These experiments show that the diffusion and desorption behaviour depends on the ice porosity, emphasizing the importance of understanding the morphology of ices in both the laboratory and in astrophysical environments.

Moving towards molecular complexity from the simple species studied in chapters 3-5, we conduct experiments to constrain photodestruction kinetics in simple ices and ice mixtures (chapter 6). UV-processing of ices is thought to be a dominant route to complex organic molecules; however, quantitative data of photo-induced processes in the solid phase are lacking. We report cross sections and quantum efficiencies for the ice photodestruction that can be input into astrochemical models to better constrain the formation of complex organic molecules.

Each of these chapters emphasize the importance of quantitative laboratory measurements of kinetic parameters associated with the mobility and reactivity of molecules in ices. Such measurements will become even more critical in the era of highly sensitive infrared telescopes like JWST.

Contents

List of figures

In memory of John T. Yates Jr.

Acknowledgments

It is true that most of the work presented in this thesis wouldn't exist without the large number of people I have worked with over the last five years. I first want to first thank my thesis committee: Rob Garrod, Ian Harrison, Brooks Pate and Bob Johnson for spending time to read through this work and make it better. For most of you this has not only happened during the final stages, but you have provided me with feedback and advice throughout my PhD that has given me fresh insight on approaching problems. Eric, thank you for taking me into your group, I have learnt a great deal from you that I'm sure will serve me well in my next position.

I want to thank the wonderful colleagues I have had at UVA, particularly Shiliang Ma who I have worked along-side since the start of my PhD. Also, Yates lab members Chunqing Yuan, Ana Stevanoic and Monica McEntee. I wish to thank members of the Herbst and Garrod groups who have greatly expanded my knowledge of astrochemical reactions and have made sure I have had a least a basic understanding of computational networks and models in astrochemistry. In the same vein, I want to thank Brett McGuire and Andrew Burkhardt and for introducing me to the world of observational radio astronomy.

I have been very fortunate to have been able to spend a lot of time visiting the Harvard-Smithsonian CfA during my PhD and have worked with some wonderful people who gave up much of their own time to help me succeed. Particularly I want to thanks Jenny, Edith, Mahesh, Zoe, Dawn, Ilse, Viviana, Pavlo and Rafa. Edith, you have been a wonderful role model for me and I appreciate your great attitude and sense of humour, both professionally and in life. Ilse, I will be forever grateful for your existence and will owe all of my future successes to people confusing me with you.

I wish also to thank a number of people who have quietly contributed to this PhD: Jeff Shabanowitz who kindly donated surplus equipment that I have used in the majority of the work presented here. Seth Matula who helped me work through all my funding crises and provided me with much needed laughs on a weekly basis. Cindy, Susie, Eddie, Danny, Mike, Jerry and the many other department staff members who have made this work possible.

I want to thank as well the good friends I have made during my time here in Charlottesville. You are as instrumental to this work as anyone else listed here. I want to thank especially my good friends Stephanie and Joel Lehman who have supported me during the good and the bad.

I want to thank my family for their love and support. Kerry, you have been such an important role model for me and taught me to love education and learning. Mum & Dad, thanks for never telling me the kind of career I should have. I know you still don't understand what a PhD is but I love you for supporting in spite of that. I also am sure you will ask what this thesis is about so here is a description of what I did just for you: I did lots of experiments where I use light and different temperatures to help understand how fast chemicals are made and destroyed in space.

Lastly I want to thank three people who are very important to this thesis:

Karin Öberg, you are such an inspiring person and I will be forever grateful that you took me under you wing when I was flailing. I can't express how grateful I am to you for allowing me to work in your laboratory, sending me to conferences and for sharing your wisdom with me.

Matthew, you have supported me scientifically on so many occasions, as well as putting up with me in life. You are a wonderful person and a brilliant scientist and I have learnt so much from you.

Lastly, to John, you were my first introduction to vacuum technology, surface science and astrochemistry of ices. You taught me the importance of careful experimentation and on seeing the big picture in the data you collect. I feel fortunate to have worked with you, even if it were for shorter than I would have liked. Thank you for sharing your infectious personality with me, thank you for your wonderful stories and teaching me the kind of mentor I want to be.

...it is difficult to admit the existence of molecules in interstellar space because when once a molecule becomes dissociated there seems no chance of the atoms joining up again

Sir Arthur Eddington, 1926

1

Introduction

1.1 Our Astrochemical Heritage

Within the last century, our understanding of the role of molecules in interstellar regions has changed dramatically. Indeed, before the 1930s, astronomers could not comprehend the presence of anything but atoms and dust particles in the interstellar medium (ISM). This notion changed at the dawn of the 1940s with the surmise[207] and subsequent identification[146] of the first interstellar molecules, methylidyne (CH) and the cyano radical (CN), based on sharp lines in stellar spectra measured at the Mount Wilson Observatory[64]. Following the advancement of radio detectors in WWII, the first molecule was discovered via its microwave spectral lines (OH) [225]. Most astronomers at the time believed these fragment species were all that could exist in the ISM because "gas densities were so low in nebulae, and ultraviolet radiation so intense, that any normal molecules surviving would be too scarce to be detectable[215]." It was not considered feasible that intact molecules like those found on earth could be observed, until Charles Townes reported the detection of water and ammonia in the late 1960s [36, 37]. It is now almost eighty years since these first molecular detections and around two hundred molecules have since been identified in the interstellar medium and circumstellar shells. These molecules include both terrestrial-like simple molecules (H_2,N_2, H_2O, CO_2) and organic species (alcohols, acids, aldehydes, ethers) as well as chemically exotic molecules not found on Earth, including highly unsaturated carbon chains and cages as well as reactive open shell molecules, radicals and ions (see Herbst & van Dishoeck [108]). The existence of terrestrial molecules in the extreme environments of interstellar space poses the question as to whether more complex and potentially prebiotic molecules can also be formed outside of our solar system.

Understanding the origins of life on earth is a fundamental question facing humankind and has been the pursuit of scientists for centuries. Interstellar clouds are the birthplace for new solar systems and therefore provide the raw material from which planets form. Several experiments in the 19th century, including the famous Miller-Urey experiment, have shown that a myriad of prebiotic molecules (amino acids, purines, pyrimidines, sugars etc.) are feasibly produced under Earth's primordial conditions from simple molecules such as H_2, CH_4, NH_3, H_2O and HCN[148, 149]. The proportion of organics synthesized on the primordial earth compared to that delivered by extraterrestrial sources such as asteroids, comets and meteoritic material remains an open question [173]. The delivery of organic material to earth has gained traction due to the indisputable evidence that meteorites and comets host a large number of prebiotic molecules [27, 103, 133]. Most likely a combination of sources provided the organic building blocks leading to the formation of biological life. To better understand these fundamental questions, astrochemistry can provide knowledge of the molecular inventory in various star-forming environments. Astrochemical observations rely on input of laboratory experiments both directly (i.e. spectra) and indirectly, through measured rates and barriers that can be input into kinetic models. Laboratory measurements of the rates of low temperature reactions (in the gas-phase and catalytically on surfaces) as well as rates of destruction by UV-photons and other energetic sources, are therefore essential to answering questions about the origins of life on Earth.

1.2 Chemistry in Astrophysical Environments

The stars in our Galaxy are embedded in the interstellar medium which contains ordinary (baryonic) matter as well as relativistic charged particles (cosmic rays) and magnetic fields. The ISM represents only a small fraction, 10-15 %, of the total mass of our Galaxy; however, it plays a pivotal role in chemical evolution during star formation. A small fraction of this mass ($\sim$1%) is composed of solid particles in the form of silicaceous or carbonaceous dust grains that can be covered by ice mantles.

The history of interstellar molecules begins with old stars that emit gas and dust during supernova explosions. The resultant gas and dust collapse inward under the influence of gravity to form diffuse clouds with temperatures 50-100 K and gas densities of 10-10^2 cm^{-3} (for reference, at atmospheric pressure there are approximately 10^{19} cm^{-3}) [220]. The diffuse medium is typically atomic, though some molecules do exist. Further gravitational collapse leads to dense clouds with gas densities of 10^4-10^6 cm^{-3} and with temperatures typically 10-20 K [16]. The sequence of star-formation following the collapse of diffuse clouds is shown in Figure 1.3.1. Reactions begin to become more efficient in the dense prestellar cores of low mass stars where barrierless gas-phase reactions are prevalent, predominantly between ions and neutrals. The ion-neutral chemistry produces a myriad of gas-phase species including terrestrial-like molecules such as CO, as well as exotic radicals, ions, metastable isomers and unsaturated carbon chains.

Initial collapse of the prestellar core leads to low mass star formation. A dense, central condensation builds up out of which radiation cannot escape, causing the collapsed area to warm up, eventually reaching temperatures of 100-300 K where it is dubbed a "hot core". The hot cores host dramatically different chemistry, in particular, high abundances of organic species are observed such as alcohols, aldehydes, esters, acids and ethers [86]. To conserve angular momentum, a rotating disk forms around the protostar forming nascent protoplanetary disks. Within the disk, dust particles begin to coalesce and aggregate to form the beginnings of meteoritic material and eventually young planets.

Interstellar dust grains are thought to be ejected into the ISM from the outflows of late-type Asymptotic Giant Branch (AGB) stars [38]. Either silicaceous or carbonaceous grains form depending on whether the AGB star is oxygen-rich or carbon-rich. The dust grains range in size from nanometers to a few micrometers following a power law distribution for which the smaller grains are more prevalent [239]. These grains absorb and scatter light from nearby stars, and were first noted as a nuisance to astronomers who, as early as the 19^{th}-century, observed that "stars are dimmed" (Wilhelm Struve, 1867).

These dust grains are believed to play several roles in the chemical evolution of star-forming regions. An important example is the case of molecular hydrogen formation. Van de Hulst first proposed the idea that dust grains could act as sites for chemical reactions to occur in 1948 for the case of H_2 formation [218]. The gas-phase production of H_2 by the reaction of two H atoms and subsequent radiative association is not sufficiently rapid to explain its abundance. Laboratory experiments have since shown that H_2 can form by the reaction of two H-atoms on astronomically relevant surface analogs, providing a vital route to the most abundant ISM molecule. [176, 177].

Dust grains can catalyze various other reactions by bringing molecules (or atoms) into close proximity and therefore enhancing the probability that two reactive species will meet. They are also able to absorb excess energy released during reactions and therefore stabilize the reaction intermediates and products. They act to shield molecules from the harsher UV-radiation fields emitted from massive stars, permitting longer survival times of species that would otherwise be rapidly destroyed. These facets allow the growth of ice mantles on the order of a hundred monolayers (ML) thick in which new, and potentially complex, molecules can be formed. These icy dust grains coagulate in protoplanetary disks to form planetesimals, asteroids, comets and eventually planets.

1.3 The Role of Ices in Astrochemistry

1.3.1 Just Common Clouds: Early Observations of Ices

The presence of ice in the ISM was remarkably first proposed in the astronomical literature by Arthur Eddington the same year as the the detection of the first gas-phase molecules OH and CN. Eddington argued that the gas column of hydrogen in nebulae would be sufficient to shield the internal cloud from ionizing-radiation, allowing atoms to exist as neutrals and to further collide to form stable molecules. Eddington expected that that molecular species, especially those with high boiling-points like water, should aggregate together. He wrote in an article appearing in the journal *The Observatory*:"Perhaps my inclination to a "water theory" is influenced by the feeling that inasmuch as the gas responsible for the mysterious light of the nebulae has turned out to be just *common air*, it is fitting that the mysterious dark obscuring masses in the Galaxy should turn out to be just *common clouds.*[66]." He wondered what a new generation of astronomers would make of this problem on the centenary of *The Observatory* in 1977. Indeed, only three years earlier than the centenary, water ice had been detected by its 3.0 μm stretching mode in Orion BN/KL [96]. Significant deviations in the 3.0 μm band were attributed to scattering from grains and to

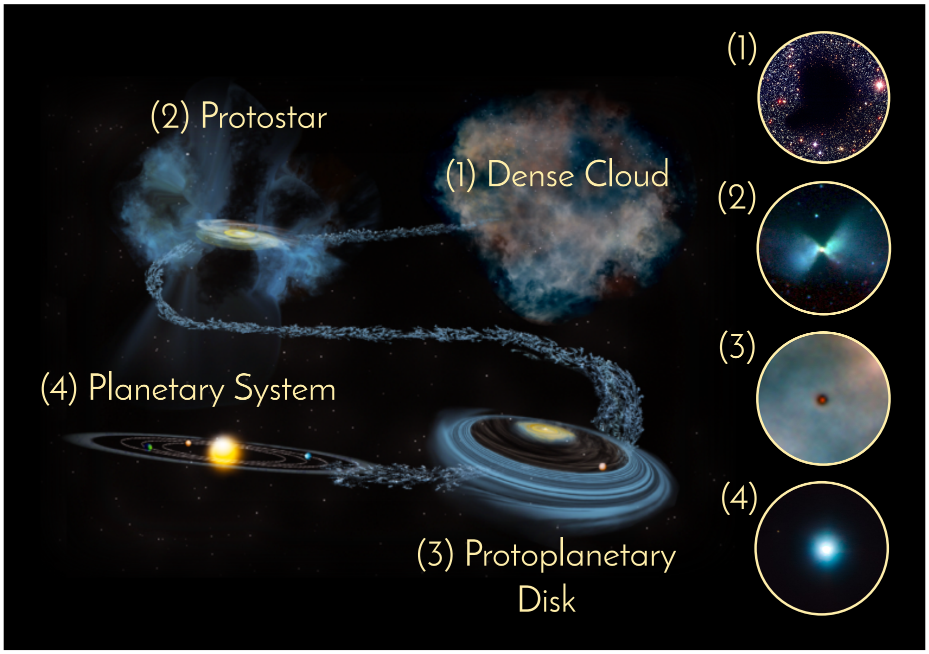

Figure 1.3.1: Astronomical stages of star formation. (1) A Dense molecular cloud at the early stages of star formation. Barnard 68 is shown as an example of an isolated prestellar core observed using the Very Large Telescope (VLT). The dust in the core attenuates the light from the background stars giving the appearance of a hole in the sky. (2) After initial collapse of the prestellar core a protostar is formed with a cold molecular envelope and a central hot core region. An infrared image protostar L1527 IRS (IRAS04368 + 2557) taken by Spitzer is shown for example. The blue region of the image shows bipolar outflows from the protostar. (3) A rotating disk is formed around the protostar resulting in a protoplanetary disk and eventually a planetary system (4). A protoplanetary disk around a young star in Orion is shown for example as imaged by Hubble. Inset (4) shows direct imaging exoplanet (small yellow dot) around T Tauri star CVSO 30. *Image credits: Bill Saxton/NRAO,(1) MacMillan Publishing/Alves et al. [4].(2) AAS/Tobin et al. [214], (3) NASA/ESA/C.R. O'Dell & S. K. Wong,(4) ESO/Schmidt et al. [194]*

interactions of water ice with ammonia mixed within the ice lattice. Another 40 years later, six major ice constituents (H_2O, CO_2, CO, NH_3, CH_4 and CH_3OH) have been clearly identified and their complex spectral profiles have been attributed to diverse ice compositions, thermal histories and grain geometries (see Boogert et al. [25] for a review).

Ice observations and abundance derivations rely almost exclusively of infrared spectroscopy of their solid vibrations in the near- to far-IR. The spectra are obtained in absorption in which the

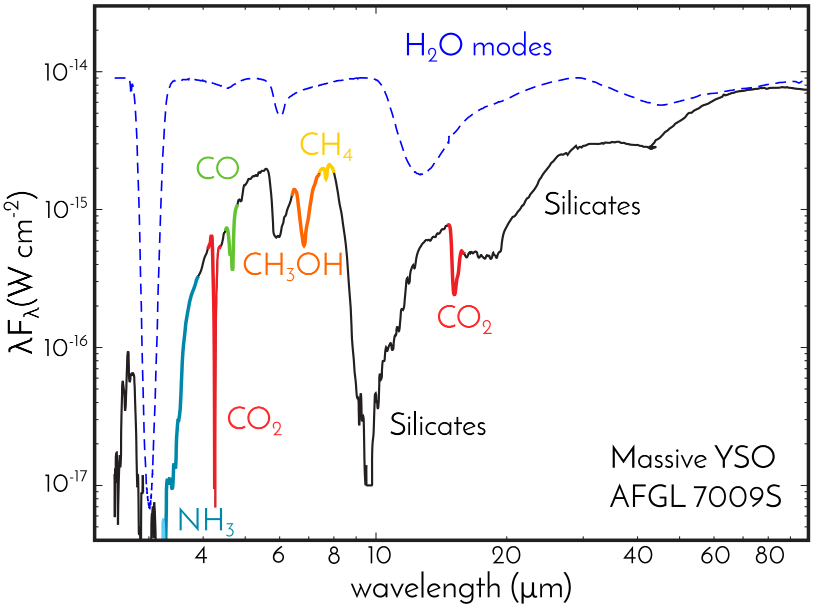

Figure 1.3.2: Example ice spectrum taken in absorption showing the strongest ice and dust features in the massive young stellar object (YSO) AFGL 7009 S. The blue dashed line shows the calculated spectrum of IR absorption by H_2O ice spheres at 10 K . This image is modified from Figure 1 of Boogert et al. [25] and originally reported in Dartois et al. [58].

cloud absorbs light from a background continuum IR-source, typically a protostar. The ice mantle compositions are then inferred by their infrared features, usually by comparing with spectra of analogs produced in the laboratory under astrophysically relevant conditions. Figure 1.3.2 shows an example absorbance spectrum taken toward the massive young stellar object (YSO) AFGL 7009 S using infrared spectrometers aboard the Infrared Space Observatory (ISO). The strong ice and dust absorption features are indicated with the NH_3 hydrate in blue, the CO_2 ν_3 and ν_2 modes in red, the CO stretching mode in green, the CH_3OH CH_3 bending mode in orange and CH_4 bending mode in yellow. The calculated spectrum for H_2O ice spheres is shown in the blue dashed line with features that can be identified in the ice absorbance spectrum: the H_2O O-H stretching, bending and libration modes as well as the transverse optical mode at 44 μm in the far-IR.

Table 1.3.1 and Figure 1.3.3 show the range of observed ice compositions in different astrophysical environments: high- and low-mass protostars, quiescent clouds and comets. The

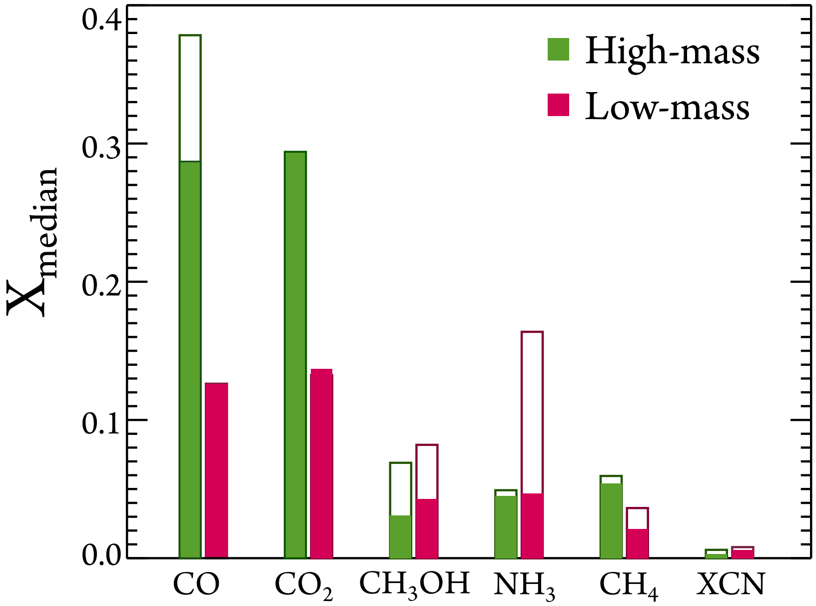

Figure 1.3.3: Median abundances of solid phase molecules with respect to water toward the low- and high-mass protostars from the Spitzer c2d survey. The outlined bars show the median detected abundances while the filled bars include upper limits. Modified from Öberg et al. [166].

cometary ices are observed indirectly by measuring the gas-phase abundances in the coma of the comet. The abundances of the ice species are typically reported normalized to water ice, the most abundant ice constituent in all sources. The ice compositions vary substantially, not only across the different environments, but also within objects of the same type. Following water, CO and CO_2 ices are most often the next most abundant ice species, ranging from as low as 3% to as high as $\sim$70% relative to water. CH_3OH, CH_4 and NH_3 are also detected at lower abundances of around 5%, though the CH_3OH abundance is quite variable and may be as high as $\sim$30% in some protostars. A number of other features have been observed in the IR-spectra of ice mantles, though due to low sensitivity and convolution of broad IR bands, their assignment is not certain. These include likely identified species H_2CO, OCN^- (originally XCN) and OSC, as well as possible species such as HCOOH, CH_3CH_2OH, NH_4^+, SO_2 and CH_3CHO.

Table 1.3.1. Observed ranges of securely identified ice constituents with respect to H_2O, along with their lower and upper quartile values, measured towards High- and Low-mass protostars, Quiescent dense clouds and cores, and comets (Adapted Boogert et al. [25])

Ice constituent	Low mass	High mass	Quiescent Clouds	Comets
H_2O	100	100	100	100
CO	$<$3-85	3-26	9-67	0.4-30
CO_2	12-50	11-27	14-43	4-30
CH_3OH	$<$1-25	$<$3-31	$<$1-12	0.2-7
NH_3	3-10	$\sim$7	$<$7	0.2-1.4
CH_4	1-11	1-3	$<$3	0.4-1.6

1.3.2 ACCRETION OF THE FIRST ICES

The observation of characteristic infrared band profiles has led to the currently accepted *two-phase* process of ice-accretion that results in layered ice structures. The high abundance of water ice in all astrophysical environments suggests a stage of accretion where the gas is H- and O-rich. During the early stages of diffuse cloud collapse the atomic H abundance (H/H_2) is large, and hydrogenation reactions on the grain surface are expected to dominate. NH_3, CH_4 and CO_2 also form concurrently, leading to the formation of the so-called *polar* ice in which these ice species are mixed with water. During this early stage the CO accretion rate varies temporally and is reflected in the CO_2/H_2O ratio. At short times, the CO gas-phase formation is incomplete leaving more oxygen available for water formation on grains. At later stages, when the density is higher and the temperature lower, CO accretion begins, resulting in CO_2 ice formation and thus an enhanced CO_2/H_2O ratio. This phase is CH_3OH poor and is recognizable by the distinct IR band profile of CO_2 mixed with CO. In a second stage, when the gas-phase CO/H ratio is drastically higher (and the atomic H abundance low), "catastrophic" CO freeze-out occurs, resulting in the grain formation of CH_3OH, CO_2 and H_2CO.

1.4 PROCESSES ON SURFACES

1.4.1 ADSORPTION:

The condensation of gaseous species directly onto a surface is known as adsorption. If the strength of interaction between the surface and the adsorbing species (adsorbate) occurs by weak van der Waals forces the adsorption is known as physisorption. If instead, a strong chemical bond is formed between the surface and the adsorbate the adsorption is known as chemisorption. The threshold energy for transition from physisorption to chemisorption is typically taken as 0.5 eV, and therefore physisorption is only detected when the temperature is low and chemisorption is absent. Chemisorption usually occurs above room temperature (k_BT = 25 meV at room temperature) and often occurs dissociatively forming new adsorbed species. In low temperature interstellar environments, molecules are absorbed by physisorption, though the importance of chemisorption in high temperature interstellar environments has not been well investigated. The concentration of species adsorbed onto a surface is typically characterized by *coverage* and expressed in units of *monolayers* (ML). A monolayer is typically defined as one adsorbate for each 1×1 unit cell of the ideal non-reconstructed substrate surface. It is often thought of as a single sheet covering the surface, however this definition holds better for well-defined surface structures and its utility for highly disordered and amorphous ice surfaces is limited. In this thesis a monolayer is used to refer to a surface density of 10^{15} molecules/cm^2.

The kinetic theory of gases can be used to derive the flux, F, of gas molecules impinging upon a surface at a defined partial pressure, p:

$$F = \frac{p}{\sqrt{2\pi m k_B T_g}} \tag{1.1}$$

where m is the mass of the adsorbate, k_B is Boltzmann's constant and T_g is the gas temperature.

The fraction of the flux of molecules that is adsorbed is defined as the sticking coefficient, s.

$$s = \sigma f(\theta)\ \exp(-E_{ads}/k_B T) \tag{1.2}$$

where σ is the condensation coefficient and relates to steric effects, $f(\theta)$ is a function that describes the probability of finding an adsorption site and E_{ads} is the activation barrier to adsorption. The rate of adsorption is then:

$$R = s \times F \tag{1.3}$$

The sticking coefficients are generally higher for heavy and polar species than light, non-polar molecules or atoms. Several experiments have found that the sticking coefficients of atoms and molecules to ice surfaces (most often ASW) at 10 K are close to 1 [105].

1.4.2 DESORPTION

Once a molecule is adsorbed onto a surface it will reside there for a characteristic residence time defined by the surface temperature and the strength of the interaction between the adsorbate and surface. The desorption rate is:

$$k_{des} = \nu\ \exp(-E_{ads}/k_B T) \tag{1.4}$$

where ν is a frequency factor describing the adsorbates motion on the surface and typically ranges 10^{12}-10^{14} s^{-1}.

1.4.3 SURFACE DIFFUSION:

When adsorbed molecules have enough energy to overcome an activation barrier, E_{diff}, but not enough to desorb, they are able to move across the surface between adsorption sites. The rate of thermal diffusion (hopping) is:

$$k_{hop} = \nu \ \exp\left(\frac{-E_{diff}}{k_B T}\right) \tag{1.5}$$

The ratio of E_{diff} to E_{des} is often treated as an empirical constant ranging from 0.3-1.0. For irregular, amorphous surfaces like ASW ice, E_{diff} has a distribution of values related to the distribution of binding potentials with different depths. At low temperature, molecules may diffuse on the surface and become trapped in deeper potential sites. In addition to the thermal diffusion mechanism, quantum tunneling has been suggested to play an important role in the diffusion of light species at low temperature. The tunneling efficiency is often approximated by a rectangular barrier with width *a*, giving a tunneling rate:

$$k_{\text{tunnel}} = \nu \ \exp\left(\frac{-2a\sqrt{2mE_{diff}}}{\hbar}\right) \tag{1.6}$$

1.4.4 SURFACE REACTIONS:

Several mechanisms can result in two molecules meeting one another on a surface and reacting. The three main processes are shown in Figure 1.4.1. The Langmuir-Hinshelwood mechanism involves prior accommodation of both molecules by the surface where both of the molecules are thermalized after adsorption. At least one of the species must be able to diffuse thermally in order to meet the other and react. In astrochemical models the rate equation for a surface species, A,

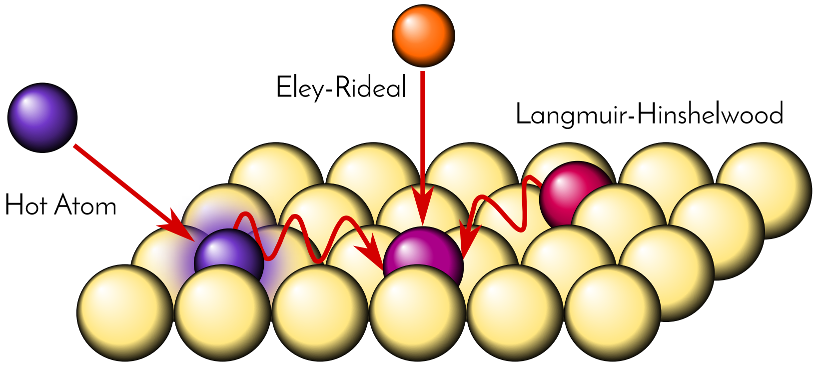

Figure 1.4.1: Surface processes leading to bimolecular reactions. The Langmuir-Hinshelwood mechanism involves two species energetically accommodated by the surface. One (or both) of the adsorbed species diffuses and meets the other one to react. In the Eley-Rideal mechanism only one species adsorbs and the other reacts with it from the gas-phase. The hot atom mechanism involves a species that is not thermalized with the surface before reaction.

reacting with another surface species, B, by the Langmuir-Hinshelwood mechanism is given by:

$$\frac{d\,N(A)}{dt} = K_{A-B}N(A)N(B) \tag{1.7}$$

where K_{A-B} is:

$$K_{A-B} = \frac{\kappa[k_{A,hop} + k_{B,hop}]}{N_s} \tag{1.8}$$

Where N(A) and N(B) are the average number of species A and B per grain, k_{hop} is the surface hopping rate, κ is an efficiency factor that refers to the probability of reaction once A and B meet and N_s is number of binding sites per grain. The hot-atom mechanism is similar and involves non-thermal diffusion of a molecule that has not yet thermalized upon surface adsorption. In this case, the molecule may diffuse and react even if the temperature is below that which would allow thermal diffusion.

Lastly, in the Eley-Rideal mechanism one molecule is accommodated by the surface and reacts with a colliding gas-phase molecule. The rate equation for an Eley-Rideal reaction between a gas-phase species, A(g), and a surface species, B(s), forming AB is:

$$\frac{d\,N(AB)}{dt} = k_{A(g)-B(s)}\, n(A(g)) \tag{1.9}$$

where the E-R rate coefficient, $k_{A(g)-B(s)}$ is:

$$k_{A(g)-B(s)} = \frac{\varepsilon \left\langle v_{A(g)} \right\rangle \sigma N(B(s))}{N_s} \tag{1.10}$$

ε is an efficiency factor, $\langle v_{A(g)} \rangle$ is the average gas-phase velocity of A(g), σ is the grain geometric cross section and $N(B(s))/N_s$ is the coverage of the surface species, B. Under interstellar conditions, the Langmuir-Hinshelwood mechanism is believed to be the dominant route for surface reactions due to the low gas flux of reactive species; however, models have shown that the Eley-Rideal mechanism can efficiently form hydrogen when the H surface coverage is high [132]. The importance of the E-R mechanism in other reactions of interstellar importance has yet to be fully investigated.

1.5 ICE THERMAL PROCESSES

After accretion of the ice mantle during the early stages of star-formation, the ices undergo heating as the cloud warms up and begins to form a protostar. Sublimation of apolar ice constituents typically begins around ~20 K. As CO desorbs from the CO/CO_2 ice environment, pure CO_2 ice is left behind, as evidenced by the 15.11 μm and 15.26 μm CO_2 bending modes in infrared spectra. Pure CO_2 ice may also be formed via segregation of CO_2 from H_2O-rich environments at temperatures above 30 K. This can be observed by shifting and narrowing of the 3.0μm CO_2 stretching mode as well as the features attributed to the pure CO_2 bending mode. The thermal processing, combined with energetic processing by UV radiation, cosmic rays or

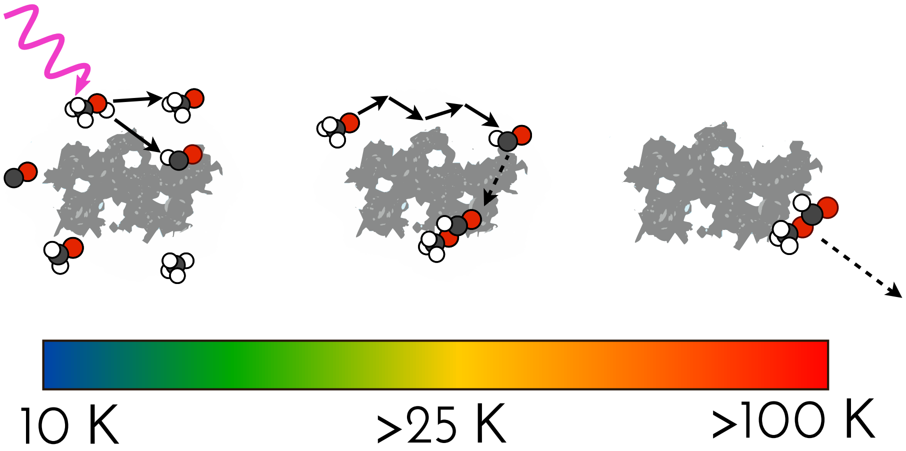

Figure 1.5.1: Cartoon depicting the warm-up model currently accepted as the most likely route to molecular complexity in the ISM. An icy grain is hit by a photon at low temperature where most of the ice molecules are immobile. This produces radicals and reactive species in the ice. When the ice is warmed to above 25 K some of the radicals are able to diffuse and react to form COMs. The COMS can desorb from the ice mantle once temperatures are greater than ~100 K, typically during the protostellar and hot-core phase. Modified from Öberg [167]

electrons, is also thought to be an important mechanism to produce complex organic molecules (COMs). COMs were first proposed to form via gas-phase ion neutral chemistry, initiated by the sublimation of methanol from grains [33, 147]. This process involved recombination of the protonated COM with an electron, a step that was ultimately shown by laboratory experiments to produce low yields of the COM [109]. The current understanding is that most COMs form through ice chemistry, though some gas-phase reactions have been shown recently to produce COMs using chemical kinetics models [9]. Recent observations of COMs in cold clouds has reopened the question about efficient routes for their formation and delivery to the gas-phase [8]. At temperatures below ~25 K, most radicals are immobile and therefore unable to diffuse and react to form more complex species. Even if formed, the heavy species require the higher temperatures present during warm-up to desorb from the grain surface. The presence of COMs in cold clouds is proposed to require either non-thermal desorption processes (photodesorption,

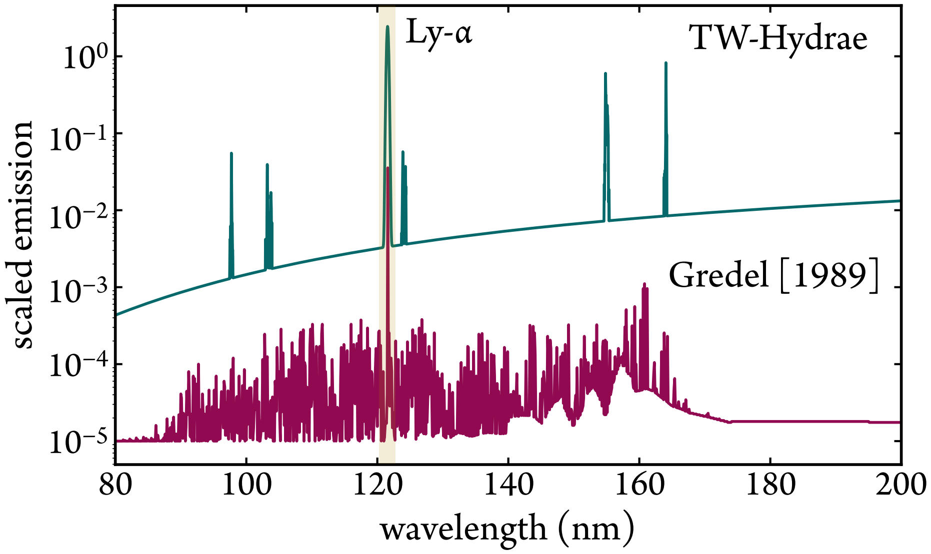

Figure 1.6.1: Examples of Lyman-alpha rich UV-fields that ices are exposed to during different stages of star-formation. The bottom (purple) shows the UV-emission spectrum calculated by Gredel et al. [99] due to cosmic ray interactions with H_2, relevant to shielded regions in dense clouds.The top spectrum (green) shows emission from the young T-Tauri star TW-Hydrae (green), calculated by Heays et al. [107] based on the work of France et al. [80], Nomura & Millar [156].

reactive desorption, sputtering) or efficient gas-phase formation mechanisms.

1.6 Ice Non-Thermal Processes

Ices are exposed to varying degrees of UV radiation during all stages of star-formation. In the proximity of massive stars, the UV-field is dominated by blackbody radiation. In the absence of a massive star, the ice is exposed to the lower intensity interstellar radiation field (ISRF) with a VUV flux of $\sim 10^8$ photons cm^{-2} s^{-1} [221]. In the interior of dense molecular clouds, gas and dust are shielded from external radiation and are instead subject to secondary radiation, peaking at Lyman-alpha (10.2 eV, 121.5 nm). This field, due to H_2 interactions with secondary electrons from cosmic ray ionizations, was calculated by Gredel et al. [98] and is shown in Figure 1.6.1.

Models of the interstellar radiation field predict an integrated flux between 91.2-205 nm of 10^8 photons cm^2 s^{-1} in diffuse clouds. Below 91.2 nm photons are totally absorbed by the atomic H column. In dense clouds, the UV produced from cosmic ray interactions with H_2 has a lower predicted flux of $\sim10^4$ photons cm^2 s^{-1} [199].

Figure 1.5.1 shows the a currently accepted route to COM formation initiated by photolysis of simple ice molecules [84]. When an ice mantle is exposed to UV photons, the molecules within the ice are dissociated to form reactive radical fragments. Reactions between radicals typically proceed without barriers and therefore can occur under ISM conditions as long as the radicals are sufficiently mobile (typically when T_{dust} >25 K) to diffuse through the ice. When the icy dust grains approach a newly formed protostar the heavier radicals within the ice mantle are able to diffuse and form new species. After the grain is heated to >100 K, the newly formed COMs can desorb and are delivered to the gas-phase, potentially enabling their radio observation.

As mentioned above, this model of COM formation has been challenged by the detection of some COMs in cold clouds with dust temperatures below that of their desorption temperature. Photodesorption has been proposed as one route to desorb molecules from ice surfaces at low temperature. This can occur either by direct photodesorption, in which the molecule absorbs the UV photon and desorbs, or by the indirect DIET mechanism (desorption induced by electronic transitions). In the indirect DIET mechanism, a molecule is first electronically excited by the absorption of a UV photon. The electronic energy is redistributed to neighbouring molecules providing sufficient energy for surface molecules to desorb. It has recently been shown that photodesorption of methanol occurs predominantly by dissociation and desorption of methanol fragments rather than by the intact molecule [20, 51], causing the efficiency of photodesorption for delivery of COMs to the gas-phase to come into question. Another mechanism proposed to delivered COMs from the ice to the gas is reactive desorption, whereby exothermic energy released in a reaction between two species is sufficient to cause desorption. Reactive desorption efficiencies are currently being measured in the laboratory and typically have low values from strongly binding ice matrices like H_2O [39, 63, 150, 159].

1.7 The Need for Laboratory Experiments

There remain a large number of questions regarding the role of ices in the astrochemical evolution of star-forming regions. The list will grow larger still with new data delivered by sensitive radio telescopes like the Atacama Large Millimeter Array (ALMA) and soon by JWST. Figure 1.7.1 outlines some key areas where laboratory experiments can provide data to better constrain interstellar observations. Laboratory spectra of ices and their optical properties at different temperatures is required for direct comparison with IR observations of astrophysical objects. In addition, spectra and optical properties of dust grain analogs are required to determine their role in chemical processes as well as how their geometries affect the spectra of ice mantles. The evolution of ices with the input of energetic photons or particles still requires a number of experiments, particularly, carefully controlled quantitative measurements of rates and cross sections. Diffusion in low temperature ices is perhaps one of the most poorly constrained facets of many astrochemical models and is critical to the time-dependent abundances of complex molecules. In particular, the diffusion of reactive species such as radicals is not well known and is a challenge for laboratory astrophysics. How molecules are delivered from the ice to the gas is a fundamental question that still requires experimental data. In particular, the role of ice morphology and composition on thermal desorption as well as non-thermal desorption routes are important to measure in the laboratory to better explain gas-phase observations.

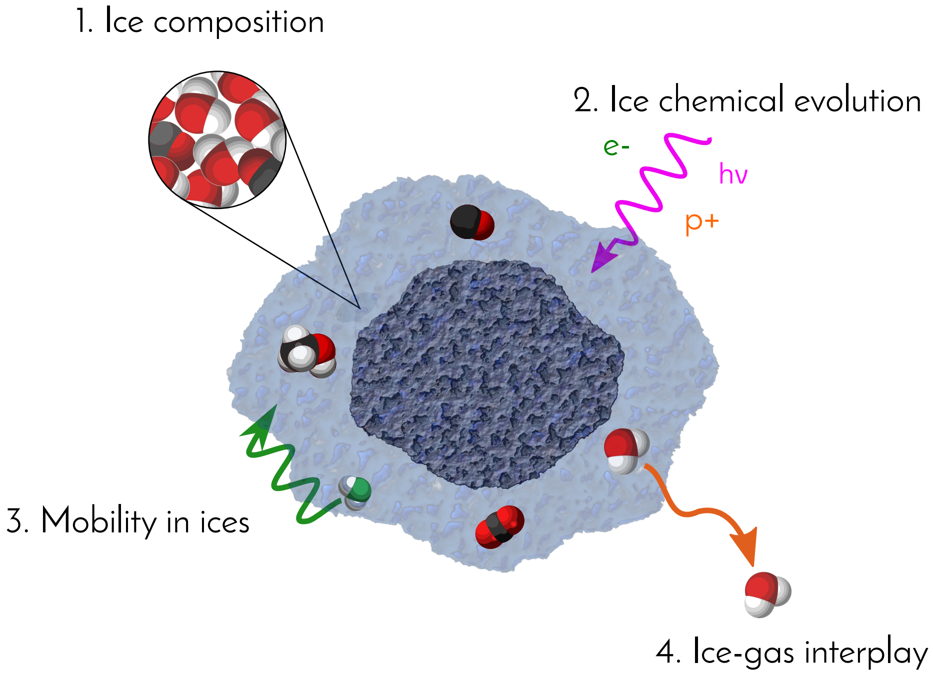

Figure 1.7.1: A cartoon diagram depicting types of information laboratory ice experiments can provide to the astronomical community including spectral information required to constrain the ice compositions from astronomical spectra (1), kinetic data of ice chemical evolution upon energetic and thermal processing (2), rates and barriers for low temperature diffusion on surfaces and in bulk matrices (3) and data on ice thermal and non-thermal desorption kinetics (4).

1.8 OUTLINE OF THIS THESIS

This thesis is focused on laboratory experiments to constrain various solid phase processes including formation, structure and composition, low temperature diffusion and mobility, desorption and non-thermal (UV) processing.

Chapter 3 reports a route to CO_2 formation via the Eley-rideal reaction between photo-produced surface OH radicals and gas-phase CO using both the King-Wells method to monitor the CO(g) loss and and IR spectroscopy to monitor the CO_2 formation. We use temperature dependent experiments to deduce a reaction barrier of 0.006 eV (70 K), essentially barrierless within the statistical uncertainty. The reaction cross section derived is 6×10^{-20} m^2

and is of the order of a geometric cross section, providing further evidence that CO does not diffuse on the surface before reacting. We use a kinetic model to fit the rate of OH consumption by CO(g) and by surface recombination and find that OH recombination consumes the majority of the surface OH radicals.

Chapter 4 reports laboratory spectra of the CO_2 longitudinal optical (LO) phonon mode in pure CO_2 ice and in CO_2 ice mixtures with H_2O, CO, and O_2 components. We show that the LO phonon mode position is sensitive to the mixing ratio of various ice components of astronomical interest. We discuss how this characteristic could be used to constrain interstellar ice compositions and morphologies era of the James Webb Space Telescope and their utility for laboratory diffusion measurements.

Chapter 5 presents measurements of CO diffusion into CO_2 ice at low temperatures (T = 11–23 K) using CO_2 longitudinal optical phonon modes to monitor the mixing of initially layered ices. We model the diffusion kinetics using Fick's second law and find that the temperature-dependent diffusion coefficients are well fit by an Arrhenius equation, giving a diffusion barrier of 300 ± 40 K. In complementary experiments, we measure the desorption energy of CO from CO_2 ices deposited at 11–50 K by temperature programmed desorption and find that the desorption barrier ranges from 1240 ± 90 K to 1410 ± 70 K depending on the CO_2 deposition temperature. The CO–CO_2 diffusion–desorption barrier ratio ranges from 0.21 to 0.24, dependent on the binding environment during diffusion.

We present the following key findings:

1. The low barrier along with the diffusion kinetics through isotopically labeled layers suggest that CO diffuses through CO_2 along pore surfaces rather than through bulk diffusion.
2. The measured CO–CO_2 desorption barriers demonstrate that CO binds equally well to CO_2 and H_2O ices when both are compact.

3. The low CO-CO_2 diffusion–desorption ratio is consistent with a surface process and adds to previous experimental evidence on diffusion in water ice that suggests surface diffusion is important to the mobility of molecules within interstellar ices.

Chapter 6 presents work in progress focused on new measurements of ice photodestruction kinetics for pure ices and ice mixtures of CO_2, H_2O, CO, CH_3OH and NH_3. We show the dependencies of the ice photodestruction cross sections on temperature, ice opacity and on the ice matrix environment.

The following key findings are presented:

1. We find the quantum efficiencies are lower in the ice than in the gas-phase for all of the ice species studied. This emphasizes the importance of replacing the commonly used gas-phase photodestruction cross sections with the relevant solid-phase photodestruction cross sections in astrochemical networks.

2. We find that the ice photodestruction cross sections are temperature dependent for all ice species, except for CO_2 ice. The temperature dependencies suggest ice cage effects indicating that less of the parent molecules are reformed as the temperature is increased. The lack of temperature dependence for CO_2 ice suggests it may be reformed by a non-thermal process.

3. We measure a low quantum efficiency for water ice photodestruction at 120 K. This suggests that less OH may be available in ice mantles than is currently assumed by astrochemical models.

4. We find that the net photodestruction rates depend on the ice composition in binary ice mixtures of CO_2, CH_4 and NH_3. Methanol ice photodestruction is not strongly affected by the presence of other ice constituents.

2

Experimental Details

The experiments presented in this thesis have been conducted using two vacuum apparatus setups, one at the University of Virginia and the other in the Öberg lab at the Harvard-Smithsonian Center for Astrophysics. The experiments in Chapters 3 and 4 were conducted at the University of Virginia, Chapter 5 at Harvard, and Chapter 6 using both setups. Each of the experiments are described in brief in the relevant chapters and in further detail below.

2.1 Vacuum Chamber Setups

University of Virginia:

The experiment consists of a cubic stainless vacuum chamber pumped to a base pressure of $\sim 1 \times 10^{-8}$ Torr with a turbomolecular pump and an ion pump.

The ices are deposited onto a cooled KBr disk that is hydraulically pressed (at ∼3000 psi) into a thin Tungsten grid (0.005 cm thick). The tungsten grid is manufactured with 22μm × $22\ \mu$m grid spacings and transmits ∼60% of the incident IR radiation. Using the tungsten grid rather than a traditional IR transparent optical window has the advantage of excellent thermal contact and heat transfer across the ice sample. In addition, the KBr pellet may be easily replaced, substituted for other substrate materials or used along side another substrate by pressing two pellets into the same grid. The KBr pellet diameter is 0.78 cm and therefore the area is 0.48 cm^2.

The temperature is measured by a K-type thermocouple that is spot welded either directly to the W-grid or to tantalum foil that is welded to the grid. The thermocouple voltage is passed through a cold-junction and amplifier and converted to temperature by means of a custom LabView program. The thermocouple is accurate to ± 0.1 K relatively and ± 2 K absolutely. The grid can be heated by applying current to heating leads that are attached to the sample holder bars.

In Chapter 3, the KBr was attached to Nickel bars connected to a rotatable glass dewar that is filled with liquid nitrogen and gives a temperature of ∼ 84 K. The KBr substrate could be further cooled by ∼12 K by bubbling He gas through the l-N_2. In the following chapters, an in-house custom built coldfinger attached to a pneumatically driven Gifford-McMahon closed cycle He-refrigerator (Air products Displex DE 202-0SP expander and APD Cryogenics HC-4 compressor) was used to cool the sample. The W-grid is suspended into the chamber by an OFHC copper coldfinger that is attached to the second-stage of the He-expander. The grid is

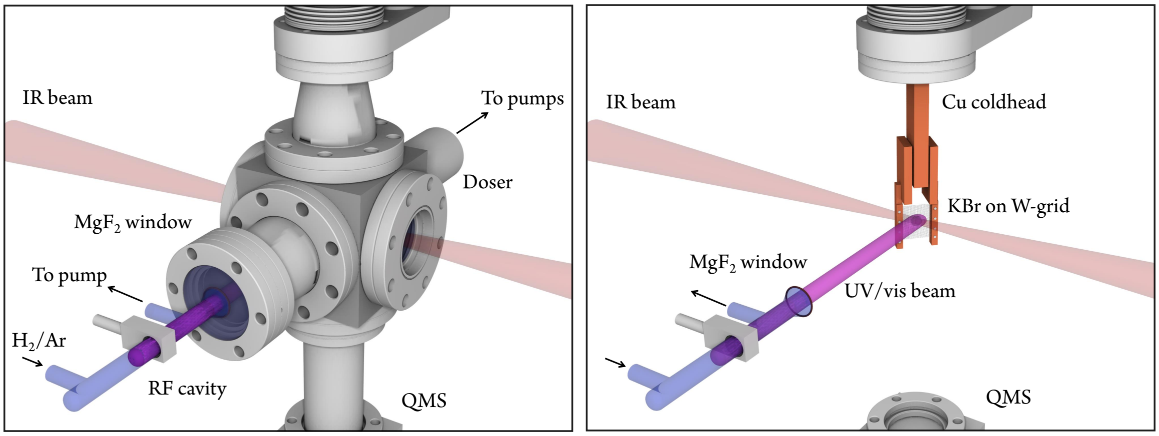

Figure 2.1.1: A cartoon diagram showing the vacuum apparatus used for conducting ice experiments at the University of Virginia. The vacuum system consists of a cubic stainless steel chamber 8.5 cm wide. Two ports are attached to differentially pump KBr windows through which the IR beam enters and exits. The hydrogen discharge lamp is attached to the front port by means of an MgF_2 window and a shutter valve (not shown). A gas doser enters through the back port which is also attached to the pumps. An RGA 200 QMS is positioned beneath the cell. Image modified from M. Reish.

attached to the bottom of the coldhead by sapphire washers so as to maintain thermal contact with the coldhead but electrically isolate the rest of the coldhead when the substrate is resistively heated. The substrate is cooled to as low as 24 K by this method. The new setup is shown in Figure 2.1.1.

Liquid samples (e.g. H_2O and CH_3OH) were prepared in borosilicate glass bulbs that are welded to VCR fittings and glass-blown closed. The liquids are added to the bulbs in a glove box under an inert atmosphere, usually N_2 or helium. Following this, the inert gas and other volatile contaminants are removed by several cycles of freeze-pump-thawing.

Harvard-Smithsonian Center for Astrophysics:

The experimental setup at the CfA (SPACECAT: Surface Processing Apparatus for Chemical Experimentation to Constrain Astrophysical Theories) is shown in Figure 2.1.2. It consists of a spherical stainless steel chamber, ~13" in diameter, pumped to a base pressure of $\sim5\times10^{-10}$ Torr

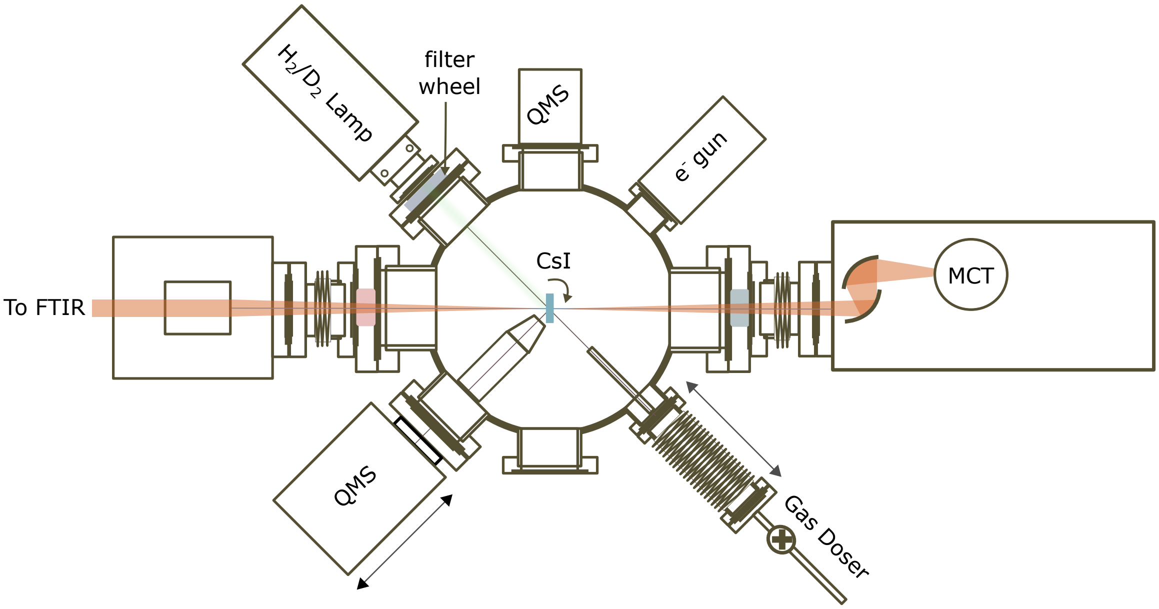

Figure 2.1.2: Schematic birds-eye-view of the UHV chamber used in the ice experiments conducted in the Öberg laboratory at the CfA. The chamber consists of a spherical, 13" diameter stainless steal chamber with ports attached to (clockwise) a movable gas doser, a viewing window, a Hiden QMS with a movable pinhole, an FTIR spectrometer IR source, a H_2/D_2 UV source, a Pfieffer QMS, an electron gun and an MCT infrared detector. Image modified from M. Rajappan.

at room temperature by a Pfeiffer Turbo HiPace 400 pump and DUO 10M rotary vane pump. Ices are deposited on a 2 mm thick IR transparent CsI substrate with a 19 mm clear view. The CsI is mounted onto a sample holder that is connected to the cold head of a rotatable closed cycle He-refrigerator (Model CS204B, Advanced Research Systems, Inc.). The substrate is cooled to as low as ~11 K and the temperature is monitored using calibrated silicon diodes measured by a temperature controller (Lakeshore, Model 335). The CsI can be heated using a 50 Ω thermofoil heater.

2.2 IR SPECTROSCOPY

2.2.1 THEORY

Infrared spectroscopy is a powerful tool for probing the composition, structure and properties of thin molecular films at low temperature. Indeed, it is currently the only method capable of directly studying ices in interstellar environments. Rotations are frozen out for all solid phase molecules (except H_2) and only vibrations within the ice lattice are visible to by remote spectroscopy.

Infrared spectroscopy relies on the motion of nuclei of molecules relative to one another. The simplest model consists of two nuclei linked by a chemical bond that acts like a spring and follows Hooke's law such the force between the two nuclei is proportional to the distance from the equilibrium length. This approximation only holds for bond distances close to the equilibrium bond length.

The Morse potential better represents molecular vibrations with large displacements from equilibrium bond lengths and/or high vibrational excitation. Figure 2.2.1 shows a comparison between the harmonic oscillator and the Morse potentials. Unlike the vibrational levels of the harmonic oscillator, which are evenly spaced, the Morse potential vibrational level spacing decreases as the energy approaches the dissociation energy.

In order for a molecule to be IR-active, the vibrational transition must occur with a change in dipole. Therefore, any homonuclear diatomic molecule is IR-inactive. This extends to the solid phase, however, defects in the ice lattice permit unallowed transitions to appear in the IR-spectrum, for example the stretching mode of O_2 ice, which appears at $\sim$1550 cm^{-1}.

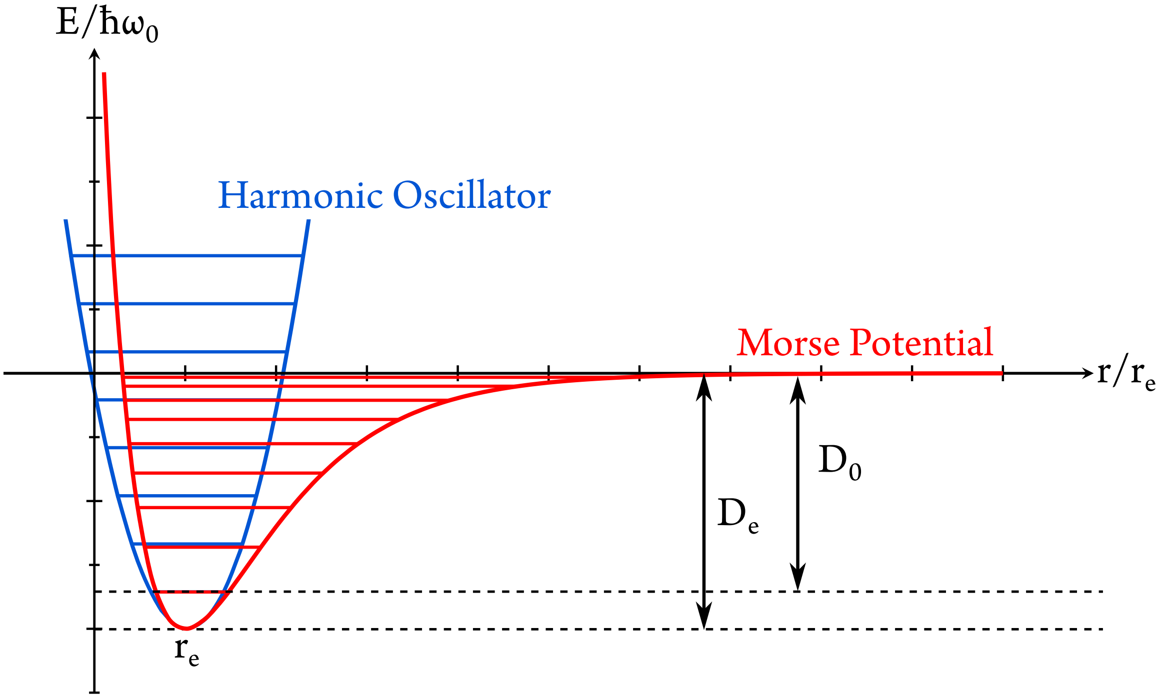

Figure 2.2.1: Potentials used to describe the vibrational energy level distribution of diatomic molecules. The harmonic oscillator potential is shown in blue and the Morse potential in red. The Morse potential better represents vibrations with energies close to the dissociation energy (D_e). The dissociation energy (D_e) is larger than the true energy required to dissociate the molecule (D_o) due to the zero point energy of the v=0 vibrational level.

2.2.2 METHODS

In both vacuum systems, Fourier transform infrared (FTIR) spectroscopy in transmission mode is used to study the ice properties in situ. At the University of Virginia, a Bruker Tensor 27 FTIR spectrometer is used with a liquid nitrogen cooled MCT detector. The IR beam is directed through the chamber using mirrors housed in boxes purged with dry-air. The beam passes through differentially pumped KBr windows either side of the chamber. Spectra are usually taken between 4000-500 cm^{-1}, with a resolution of 2 cm^{-1}. Each spectrum is typically averaged from 100-200 scans. Background spectra are taken either through the KBr disk or by moving the KBr out of the way of the beam using a z-axis bellows.

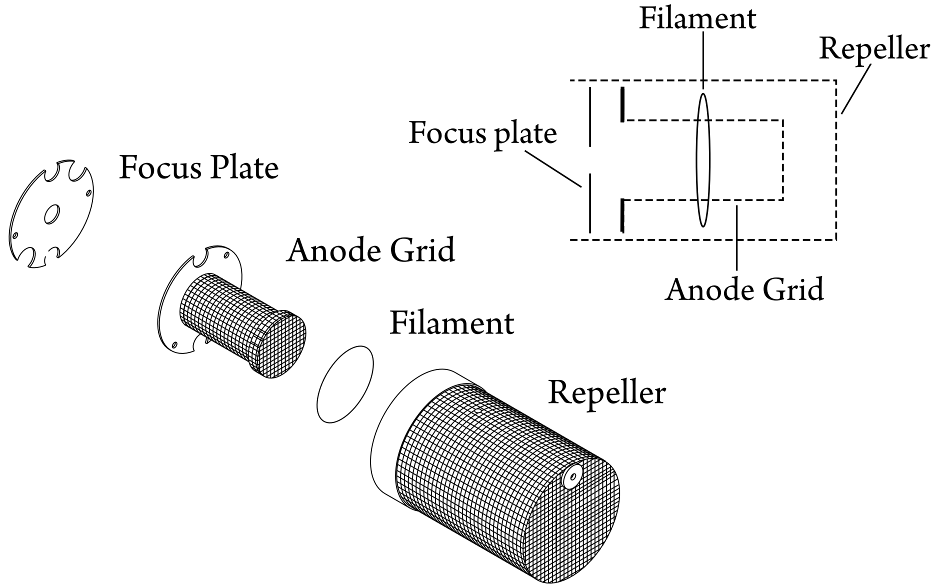

Figure 2.3.1: The RGA-200 ionizer used to produce ions for mass spectrometric analysis. The ionizer consists of a ThO$_2$/Ir filament that is housed inside a repeller cage and sits over a anode grid. The filament is heated to incandescence, producing electrons that accelerate toward the anode and bombard gas-phase molecules. The repeller acts to increase the ionization efficiency by trapping the electrons that make it out of the anode grid without collision. The ions are then sent to the quadrupole by the negative potential applied to the focus plate. *Image modified from RGA200 Operating Manual, Standford Research Systems*

At the CfA, a Bruker Vertex 70v FTIR spectrometer with a liquid nitrogen cooled MCT detector is used to monitor the ice. The focusing optics are housed in pumped compartments to avoid IR absorbance from water and CO$_2$ in air.

2.3 MASS SPECTROMETRY

2.3.1 THEORY

Mass spectrometry is a useful technique that can be used to distinguish gas-phase molecules based on their mass. In mass spectrometry, a molecular species is ionized and the ions are separated based on their mass-to-charge (m/z) ratio. The number of ions are counted for each m/z and presented as a spectrum. The mass spectrometers we use in this research are quadrupole mass spectrometers that use electron bombardment to produce ions. Figure 2.3.1 shows the constituents of the Standford Research Systems RGA 200 ionizer used in this research. The incoming molecules are ionized by electrons emitted by a hot filament made from thoria coated iridium wire. The filament encircles an anode grid and is housed inside of a repeller cage. The electrons emitted at the filament are accelerated toward the positively charged anode where those that pass through the mesh may come into contact with a gas molecule and cause an ionization event. Those that pass through the anode without collision are re-accelerated back toward the anode by the field created between the repeller and the anode grids, increasing the ionization efficiency. The positive ions are then transferred to the quadrupole by the focus plate where they are filtered according to mass. The masses are filtered by altering the DC and RF voltages along four cylindrical electrodes such that only the ions of interest have stable trajectories and reach the ion detector. The ion detector is chosen from either a Faraday cup or an electron multiplier depending on the partial pressure of the gas species to be measured.

2.3.2 TEMPERATURE PROGRAMMED DESORPTION

The kinetics of desorption from surfaces can be studied by temperature programmed desorption (TPD). In this technique molecules are adsorbed to a surface, the temperature is ramped linearly with time and the desorption flux is measured using a mass spectrometer. The desorption rate is given by:

$$\Phi_{des} = -\frac{d\theta}{dt} = \nu\, \theta^{n}\, e^{-E_{des}/T} \tag{2.1}$$

where θ is molecular coverage, T is the surface temperature in K, ν is a pre-exponential frequency factor in s^{-1}, n is the desorption order and E_{des} is the desorption energy in K. Given a linear heating ramp rate, $\beta = dT/dt$, we then have:

$$-\frac{d\theta}{dT} = -\frac{d\theta}{dt}\frac{dt}{dT} = \frac{\nu}{\beta}\,\theta^{n}\,e^{-E_{des}/T} \tag{2.2}$$

In the multilayer regime the ice desorption energy can be derived by solving equation 2.1 in zeroth-order (n=0). The desorption energy and frequency factor are extracted from a linear plot of ln(Φ_{des}) vs 1/T:

$$ln(\Phi_{des}) = -\frac{E_{des}}{T} + ln(\nu) \tag{2.3}$$

The multilayer regime is more complex as the desorption flux depends on the coverage of adsorbed molecules. In the case of inhomogeneous surfaces like those of ice mantles, the molecules interact with adsorption sites described by potential wells of various depths. A number of different techniques have been used to extract the desorption energy for the multilayer regime. We use a first-order adsorption energy distribution (similar to that presented in Doronin et al. [62]) that independently considers the desorption energy (E$_i$) and coverage (θ_i) associated with each binding site, i, at a given temperature:

$$\Phi_{des}(T) = \sum_{i} \nu_i\,\theta_i e^{\frac{-E_i}{T}} \tag{2.4}$$

we assume that the prefactor, ν_i, doesn't change significantly between adsorption sites for modelling the desorption of CO; however, this should not be considered the case for larger molecules with more degrees of freedom.

2.3.3 METHODS

At the University of Virginia a quadrupole mass spectrometer (RGA 200, SRS) is mounted beneath the chamber with the filament ∼2" away from the substrate.

At the CfA, two mass spectrometers are available to monitor the gas partial pressures. A Pfeiffer quadrupole mass spectrometer (QMG 220M1, mass range 1–100 amu, and resolution of 0.5 amu) is position at 90° to the IR beam and 45° to the H_2/D_2 lamp. A second quadrupole mass spectrometer (Hiden IDP 300, Model HAL 301 S/3) equipped with a pinhole on a translational stage that can be moved within 0.5 inches of the CsI window is positioned at 45° to the IR beam and 90° to the H_2/D_2 lamp. In both cases, the temperature ramp rate can be controlled by temperature software. Further description of the TPD measurements can be found in Chapter 5.

2.4 UV LAMPS

Photon-induced processes are an important component of many of the experiments reported in this thesis. Broad-band hydrogen discharge lamps are perhaps the most commonly used UV sources in astrochemical laboratory experiments. These lamps are easy to maintain and produce high photons fluxes, typically 10^{13}-10^{15} photons s^{-1}. Hydrogen lamps can be used to produce a continuum in UV range between 110-180 nm including a peak at the Lyman-alpha line (121.6 nm, 10.2 eV), which simulates the UV-emission in some ISM regions well. The continuum emission in the 140-170 nm range comes from the Lyman-band system of molecular hydrogen. The properties of the lamp emission can be tuned by changing the operating parameters such as the H_2 pressure, microwave power and lamp geometry. In particular, the edition of rare-gas buffers such as helium or argon can change the lamp emission spectrum, enhancing the emission at Lyman-alpha [34, 135, 168].

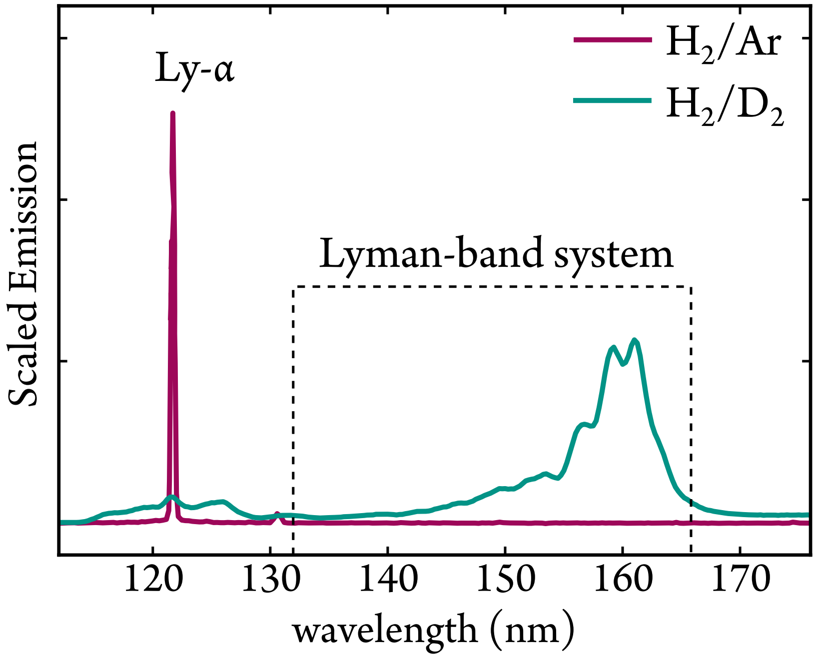

Figure 2.4.1: Expected emission profiles of the two lamps used as UV-sources in this thesis. The purple curve shows the Lyman-alpha dominated emission of an H_2/Ar lamp as measured by Y.-J. Chen for a similar lamp to ours (Private communication). The green curve shows the emission of the H_2/D_2 lamp as measured by the manufacturer (Hamatsu). The emission is scaled for clarity.

At the University of Virginia we use an F-type microwave discharge hydrogen lamp. The Hydrogen is mixed with to 10% in Ar in a custom made gas mixture (Praxair) and flowed through a quartz lamp by means of a gas-line pumped by a mechanical pump. At Harvard, we use an H_2/D_2 lamp from Hamamatsu (model L11798) that produces a more broadband emission, peaking at 160 nm and to a lesser extent at Lyman-alpha. The expected emission profiles from the lamps are shown in Figure 6.2.1.

2.4.1 FLUX MEASUREMENTS

Two methods have been widely used for calibration of the photon fluxes from microwave discharge lamps. The first method is based on chemical actinometry, most commonly the

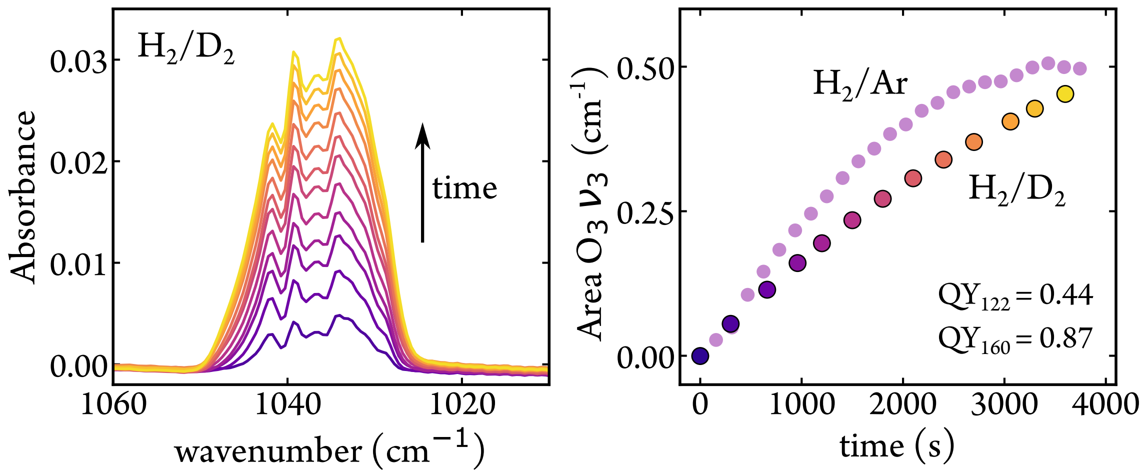

Figure 2.4.2: Example of an oxygen actinometry experiment. O_2 is deposited on the IR substrate at low temperature. The ice is exposed to VUV radiation and the level of ozone production. The quantum yield for ozone production is used to calculate the photon flux. This figure shows an example for O_2 actinometry for the H_2/D_2 lamp. The ozone growth using the H_2/Ar lamp in shown in purple for comparison.

photolytic conversion of O_2 ice into O_3 [48, 91]. Ozone is formed during O_2 photolysis by the following two-step mechanism:

$$O_2 \xrightarrow{hv} O + O \tag{2.5}$$

$$O_2 + O \longrightarrow O_3 \tag{2.6}$$

CO_2 ice has also been used as a chemical actinometer based on the conversion of CO_2 to CO under UV radiation. However, the absorption spectrum of both O_2 and CO_2 ice in the vacuum ultraviolet (VUV) are wavelength dependent, so that the photon flux calibration will depend on the emission profile of the VUV light source employed. In addition, the conversion efficiencies are often taken from gas-phase experiments due to the lack of solid phase data [100]. Recent experiments indicate that the quantum efficiency in the ice is significantly lower than the gas-phase and suggest a wavelength dependence [48, 82]. Fulvio et al. [82] used a gold photo-detector to calculate the quantum yields for O_3 production using dominantly Lyman-alpha and 160 nm emission from a filtered H_2 lamp. They report quantum yields of 0.44±0.16 and 0.87±0.30 for 122 nm and 160 nm, respectively.

OXYGEN ACTINOMETRY

We use oxygen actinometry to measure the photon flux in both chambers. Figure 2.4.2 shows example spectra from one of the actinometry experiments conducted using the H_2/D_2 lamp at the CfA with an MgF_2 window. The oxygen ice thickness is monitored using the weak mode around 1550 cm^{-1}, however the band strength for this mode is highly uncertain. We err on the side of caution and use the lower band strengths reported in order to produce ices thick enough to absorb all of the VUV-photons. The ozone produced is monitored by the O_3 ν_3 mode at ∼1040 cm^{-1}. The flux is calculated by:

$$Flux = \frac{\text{Area}(\nu_3)}{A(\nu_3) \times \Phi \times t} \tag{2.7}$$

Where Area(ν_3) is the integrated absorbance area of the O_3 ν_3 mode, A(ν_3) is the band strength for ozone, Φ is the quantum yield for O_3 production and t is the photo-irradiation time. We calculate the flux using three methods: (1) using the gas-phase values for A(ν_3), Φ (2) using the gas-phase values with the solid phase adjustment factor reported by Cottin et al. [48], and (3) Using the O_3 band strength reported by Loeffler et al. [137] in RAIRS, scaled for transmission-IR, and the solid-phase quantum yields reported in Fulvio et al. [82]. The fluxes obtained using the Cottin adjustment factor are within 10% of those using solid phase data for the 160 nm dominated H_2/D_2 lamp, however they underestimate the flux from the Lyα dominated H_2/Ar lamp by ∼50%. This is not surprising given the lamp used by Cottin et al. [48] was

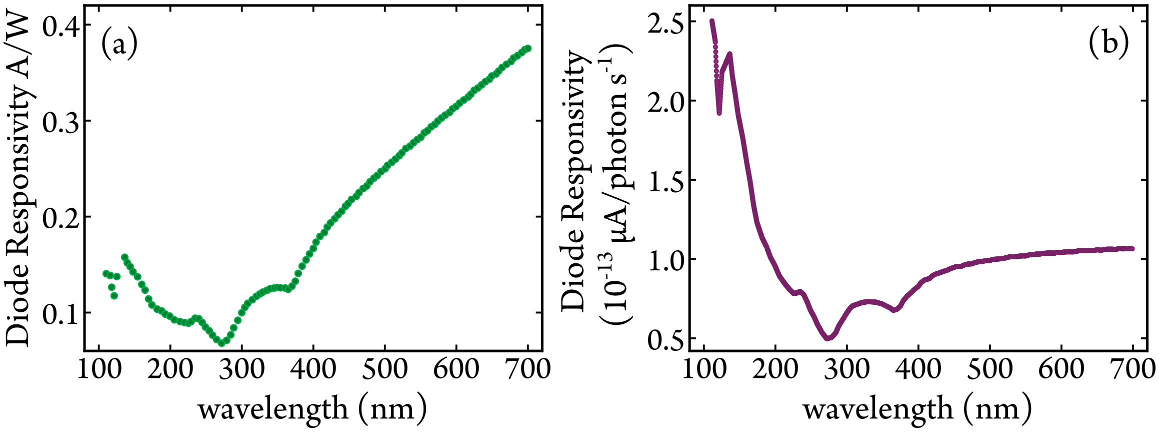

Figure 2.4.3: (a)The absolute responsivity of a standard AXUV100G photodiode calibrated by NIST. (b) the absolute responsivity converted to microamps per photon flux in order to show the importance of each wavelength to the total diode reading. The absolute responsivity in panel (a) is interpolated to convolve with the lamp emission spectrum.

dominated by emission at 160 nm. The fluxes obtained using the gas-phase quantum yield and O_3 band strength are typically lower by 4-7× the fluxes calculated using the solid phase data.

Photodiode Calibration

The second common method to determine VUV photon fluxes is to use a calibrated photodiode (typically by NIST) for which the responsivity of the diode at different wavelengths is well known. The flux obtained by this method can be overestimated if the visible component from the lamp is not taken into account explicitly, since the photodiode response is substantial in the visible. Figure 2.4.3 shows the diode response for a standard AUXUV100G photodiode. The response is recorded in A/W (panel a) and converted to units of μA/ Flux (panel b) in order to better show the wavelength dependencies. From these plots is it evident that that diode response is higher in the VUV but is still significant in the UV and visible. In order to calculate the percentage of the photocurrent from photons >220 nm, we convolve the full lamp spectrum (110-700 nm) with the diode responsivity. We find the photons >220 nm contribute around 25%

of the photon flux read by the photodiode. This correction is taken into account in calculations involving photoprocesses in Chapter 6. We are currently in the process of installing an MgO window to cut off the VUV below ∼220 nm to directly measure the diode response in the visible.

2.4.2 GAS-PHASE ACTINOMETERS

We also use two gas-phase actinometers to measure the photon flux from the H_2/Ar lamp at the University of Virginia. The first method utilizes $N_2O(g)$ photodestruction and is described in detail in Rajappan et al. [181]. N_2O photodecomposition involves two primary photolysis channels followed by secondary reactions of the photoproduced O with N_2O:

$$\begin{aligned} N_2O + h\nu &\longrightarrow N_2 + O && (2.8)\\ N_2O + h\nu &\longrightarrow NO + N && (2.9)\\ \frac{1}{2}O + \frac{1}{2}N_2O &\longrightarrow \frac{1}{2}N_2 + \frac{1}{2}O_2 && (2.10)\\ \frac{1}{2}O + \frac{1}{2}N_2O &\longrightarrow NO && (2.11) \end{aligned}$$

This gives a quantum efficiency of 0.67 photons/N_2O decomposed. In order to minimize wall effects we use 10 Torr of N_2O, which results in an absorption path-length through the cell of only a few mm. The N_2O integrated absorbance is measured over the photolysis period is converted, first to a partial pressure using a baratron gauge calibration, and then to the number of N_2O molecules using the calibrated cell volume. The flux can then be extracted from a plot of the number of N_2O molecules over time using a quantum efficiency of 0.67 photons/N_2O (Figure 2.4.4). Using this method we obtain a flux of 1.4×10^{15} photons cm^{-2} s^{-1} at the MgF_2 window, which translates to a flux of 3.0×10^{14} photons cm^{-2} s^{-1} at the 45° IR substrate.

CO_2 actinometry was conducted in the same way as the $N_2O(g)$. The chamber was filled with

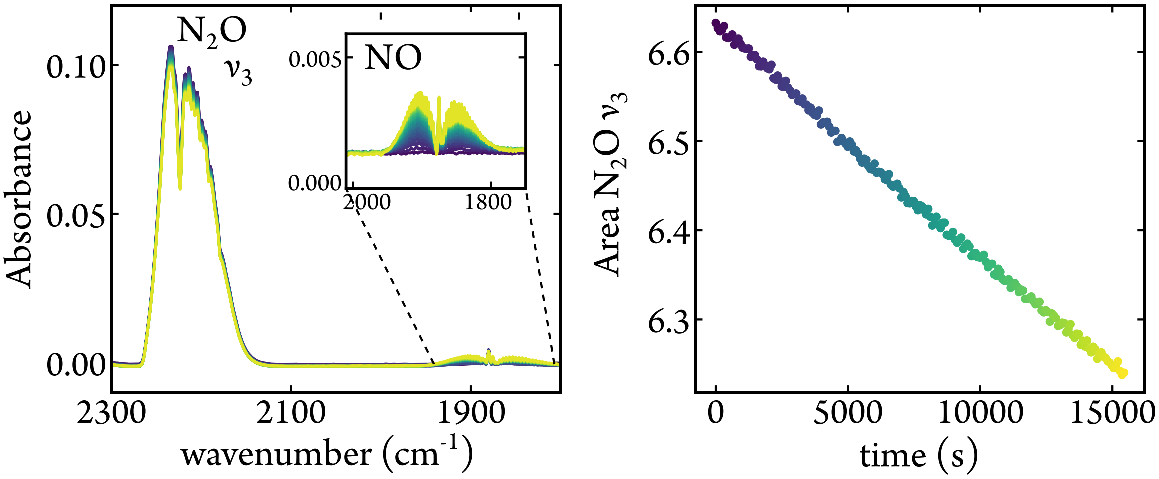

Figure 2.4.4: Example of an $N_2O(g)$ actinometry experiment. The photolysis chamber is filled with ~10 Torr of N_2O and exposed to UV-photons from the H_2/Ar lamp. The loss of N_2O is monitored over time by its IR ν_3 mode (left) and used to calculate the lamp flux assuming a quantum efficiency of 0.67 photon/N_2O. The inset shows the production of NO during the photolysis period.

roughly 10 Torr of $^{13}CO_2$. We use isotopic CO_2 to avoid atmospheric contamination due to a slow leak through the KBr windows when the chamber is closed to the pumps. The photolysis of CO_2 at Lyman-alpha produces CO with a quantum yield of 1. Compared to N_2O, the absorption cross section at Lyman-alpha is low (6.3×10^{-20} cm^2) such that all of the VUV photons aren't absorbed by the gas column. The flux can be calculated by the monitoring the CO_2 destruction (or CO production) and correcting for the proportion of photons absorbed:

$$Flux = \frac{\Delta P_{CO_2}}{\Delta t} \frac{V}{k_B T} \frac{1}{\varphi_{Lya} \beta_{Lya}} \tag{2.12}$$

Where P_{CO_2} is the partial pressure of CO_2, V is the calibrated cell volume, T is the gas temperature, φ_{Lya} is the quantum efficiency for CO_2 destruction at Lyman-alpha. Beta is a factor used to correct for the proportion of photons absorbed in the cell column:

$$\beta_{Lya} = 1 - \exp(\varepsilon_{Lya} \, l \, P_{CO_2}) \tag{2.13}$$

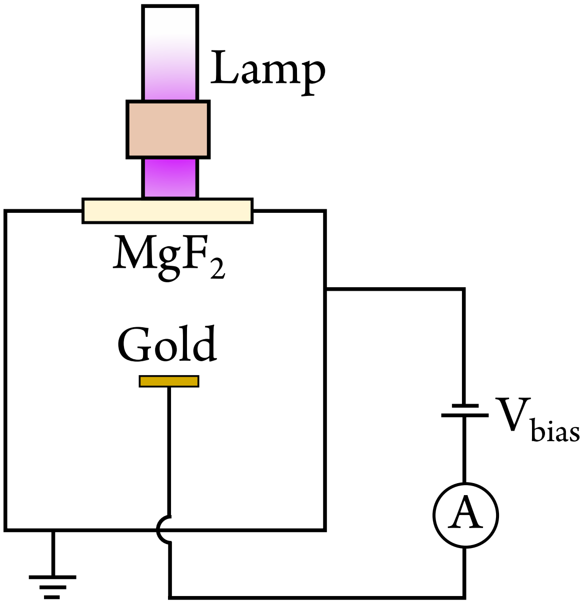

Figure 2.4.5: Diagram depicting the experimental setup and circuit used for measurement of the gold photo-current as a flux calibrator. A negative bias voltage is applied so that all of the photoelectrons emitted by the photoirradiation of the gold are collected by the chamber walls and measured by the multimeter.

We determine the flux using both CO_2 destruction and CO production. We use $\varepsilon_{Lya} = 1.61$ atm cm^{-1} [232]. CO integrated absorbance is converted to partial pressure using an integrated band strength of 243.3 cm^{-2} atm^{-1}. We use a calibration curve from measurements with a baratron gauge to convert the CO_2 integrated absorbance to partial pressure. We find fluxes of 4.8 $\times 10^{14}$ photons cm^{-2} s^{-1} using CO_2 loss and 5.1×10^{14} photons cm^{-2} s^{-1} using CO production.

2.4.3 GOLD PHOTODETECTOR

We are currently developing a gold-photodetector based on the methods of Fulvio et al. [82]. The work function of gold is 4.2-5.2 eV and therefore visible light from the lamp does not contribute to the flux. We chose to deposit gold onto a glass slide by evaporation in order to produce a gold spot the same size as the IR transparent KBr disk. This will account beam divergence and/or misalignment between the IR probe beam and the UV-beam.

The setup consists of a vacuum feed-through that is spot welded to a boat heater evaporation source and housed inside a chamber pumped to $\sim 10^{-5}$ Torr. The boat is heated to >1000 °C using a high current power supply. At this temperature the gold is melted and evaporates, depositing onto a glass slide that is positioned directly above the gold source. We cover the slide with a tantalum foil mask that is drilled with a hole the same size as the KBr substrate.

The slide will be positioned in the chamber at the same position as the KBr substrate and attached to a circuit (shown in Figure 2.4.5) via a thin gold coated copper wire that is epoxyed to the slide and placed in contact with the gold spot. A negative bias voltage is applied and varied until a saturation current is reached. The bias voltage is necessary to negate the effects of electrons collected by the gold coming from other parts of the chamber or from low energy electrons from the gold that are returned rather than being collected by the chamber. The stronger the negative bias voltage, the more electrons collected from the gold by the chamber walls and once the electric field between the gold and the chamber is high enough, none of the electrons can return to the gold surface. The saturation current (I_{sat}) is then used to calculate the photon flux using the photoelectric yield, Φ_λ):

$$\text{Flux} = \frac{I_{\text{sat}}}{e \times \Phi_\lambda \times \text{A}} \tag{2.14}$$

where e is the elementary charge and A is the area of the gold spot. We plan to implement this method to measure the photon flux in the coming months.

3

Carbon Dioxide Formation via the Eley-Rideal Reaction of CO(g) + OH(s)

Modified from: Chunqing Yuan, Ilsa R. Cooke and John T. Yates Jr. 2014, *ApJL*, 791, L21.

CO_2 is one of the most abundant components of ices in the interstellar medium; however, its formation mechanism has not been clearly identified. Here we report an experimental observation of an Eley-Rideal-type reaction on a water ice surface, where CO gas molecules react by direct collisions with surface OH radicals, made by photodissociation of H_2O molecules, to produce CO_2 ice on the surface. The discovery of this source of CO_2 provides a new mechanism to explain the high relative abundance of solid CO_2 ice in interstellar environments.

3.1 Introduction

The abundance of CO_2 in ices in the interstellar medium (ISM) greatly exceeds that in the gas phase [219]. This suggests that a solid phase CO_2 synthesis process is probably involved, but the

CO_2 formation mechanism has not been clearly identified. Recent observations indicate that CO_2 (ice) formation is linked to H_2O formation [23]. Theoretical and laboratory studies suggest an efficient $CO + OH \rightarrow CO_2 + H$ reaction in CO/H_2O mixed ices due to its low activation energy barrier [85, 111, 153, 157, 190, 238]; however, the limited mobility of CO and OH species at low temperatures inhibits the reaction probability. Carbon monoxide is the second most abundant gas species after hydrogen in the ISM [213] and is thought to be the parent molecule for the synthesis of CO_2, as well as for many organic molecules in astrophysical environments [70]. Here we report an efficient surface reaction pathway for gas phase CO conversion to solid CO_2 on amorphous solid water (ASW) films or crystalline water ice films in the temperature range 71–82 K, activated by ice absorption of Lyα (10.2 eV) radiation. A direct Eley–Rideal (E-R) process [71, 72, 183] that does not involve prior energetic accommodation of CO by the ice surface is observed, when the incident CO molecules interact with surface-bound OH radicals that are produced by water photodissociation. The surface reaction is kinetically separate from the previously studied solid phase CO + OH reaction. This finding of a significant new process for CO_2 production will influence kinetic models involving CO(g) consumption and CO_2(ice) formation in molecular clouds [190, 231] or in the atmospheres of icy moons in the solar system [210]. More generally, this result suggests that similar E-R surface reactions on ice films which contain surface-bound radical species are likely to occur for other gas molecules in astrophysical environments.

Photochemical processes are known to drive molecular synthesis in the ISM, especially inside thin ice films condensed on dust grains [90, 189, 221]. During photodissociation of mixed CO/H_2O ices, hydroxyl radicals are produced that can interact with CO. This reaction has been studied in the laboratory by hydrogenation of CO/O_2 binary ices [111, 153] and by CO reaction with non-energetic OH radicals [157, 238]. In contrast to these studies of bulk ices containing condensed CO molecules, here we report that gas phase CO has a remarkable reactivity with photochemically generated OH radicals on the surface of H_2O ice. This finding reveals a significant new kinetic process for CO_2(ice) formation in space.

The classical E-R mechanism for a surface reaction involves, in its simplest form, the direct collision of an incoming species from the gas phase with a surface-bound species to produce a product molecule and was originally proposed as the mechanism for a metal-catalyzed surface reaction [183]. This type of surface reaction occurs with reactive incoming species such as atomic H [35]. In the ISM, it is proposed that molecular H_2 formation by H + H recombination in high temperature regions occurs efficiently through the E-R mechanism [134]. A modification of the classical direct E-R reaction involves an incoming species which partially accommodates on the surface as a mobile precursor and, in its subsequent diffusive motion, encounters an immobile reactive partner which then participates with the mobile species in a chemical reaction [102]. Such a process should exhibit temperature dependence due to the decreasing lifetime and steady-state coverage of the mobile species as temperature is raised. We present kinetic evidence that the CO + OH (on water ice) reaction occurs by a direct E-R process not involving CO surface mobility.

3.2 EXPERIMENTAL

The apparatus has been described previously in detail [234]. Briefly, the apparatus is a baked high vacuum system with a base pressure of $\sim 10^{-8}$ Torr, pumped by turbomolecular and ion pumps. Figure 3.1.1 shows an experiment which demonstrates the photochemically induced reactivity toward CO(g) of a 20 nm thick ASW film. The H_2O film is deposited at 76 K on a 0.3 cm^2 disk of pressed KBr powder held on a tungsten grid in the high vacuum stainless steel cell of 1.9×10^{-3} m^3 volume. In addition, crystalline ice films were made by heating deposited ASW to 170 K until the phase transition was completed and then cooling to 76 K for similar studies. Lyα radiation

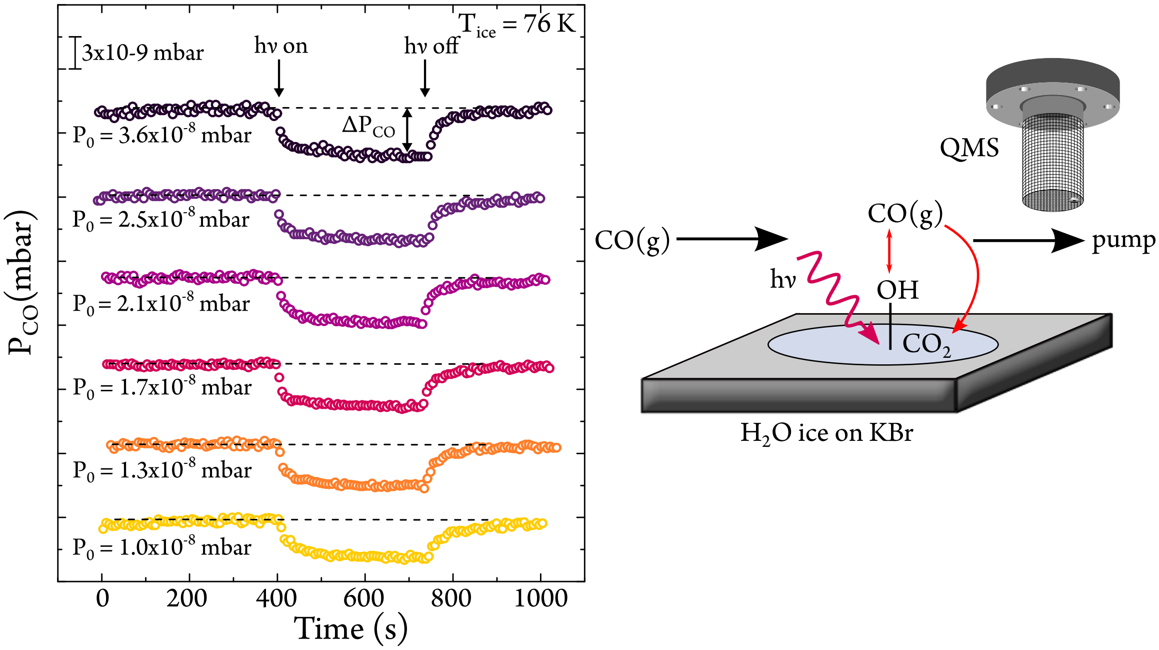

Figure 3.1.1: *Left:* CO(g) consumption during the experiments at various CO pressures flowed across CO_2 ice at 76 K. The curve is determined by measurements of $C^{18}O$ behavior and then converted to total CO pressure using the fraction of $C^{18}O$. Typically X_{C18O} is in the range 10%–80%. *Right:* Schematic of CO(g) consumption measurement procedure on irradiated ASW.

(2.7×10^{14} photons $cm^{-2}\ s^{-1}$)[181, 182], passing through a MgF_2 window and an internal aperture, is incident at 45° to the ice film. Transmission IR spectroscopy at a 45° incidence angle to the ice surface is performed during the irradiation to observe the formation of condensed CO_2 product. A quadrupole mass spectrometer senses the pressure of flowing CO(g) before, during and after irradiation. A mixture of $C^{16}O$ and $C^{18}O$ is employed with a mole fraction, X_{C18O}. We measured the $C^{18}O$ ($m/z = 30$) behavior and converted it to total CO pressure using measurements of X_{C18O}. The CO pressure is established over the ice film using a measured CO pumping speed of $2 \times 10^{-4}\ m^3\ s^{-1}$ [235]. When the UV light is emitted, CO begins to be consumed immediately and a steady-state CO pressure is reached in about 300 s. When the UV light is turned-off, the CO pressure rises back to the original value in about 300 s. This behavior is

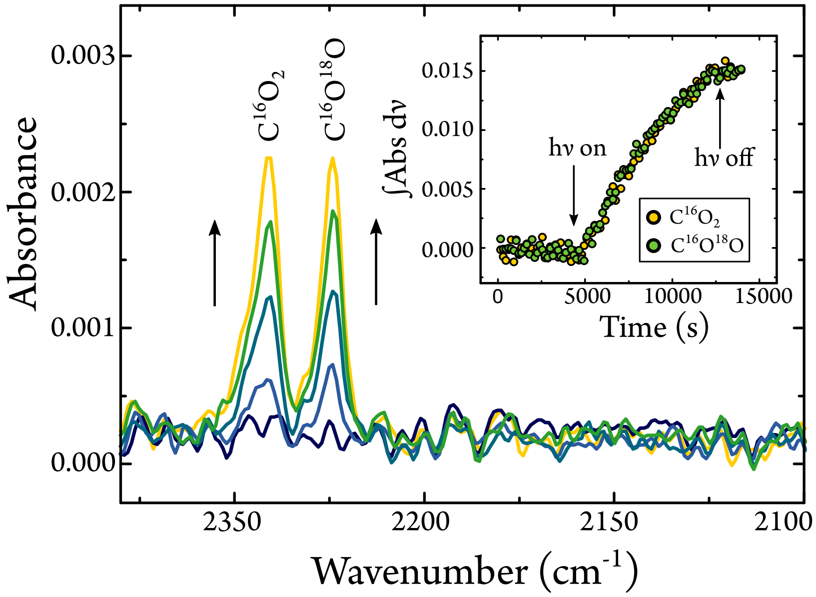

Figure 3.2.1: IR spectra of $C^{16}O_2$ and $C^{16}O^{18}O$ isotopomer ices produced during $C^{16}O(g)$ and $C^{18}O(g)$ reaction on irradiated ASW. The inset shows the growth of integrated absorbance of $C^{16}O_2$ and $C^{16}O^{18}O$ isotopomers during the irradiation time.

observed at many CO pressures and the experiment closely resembles the well-known King–Wells method used in surface science to measure adsorption kinetics [118]. The change of CO pressure (ΔP_{CO}) is found to be similar (±20%) with both thick and thin ASW films, as well as on a crystalline ice film.

Figure 3.2.1 shows the photochemical production of condensed CO_2 isotopomers during the experiment where $X_{C18O} = X_{C16O} = 0.50 \pm 0.05$. The strong ν_3 modes for $C^{16}O_2$ and $C^{18}O^{16}O$ are observed. Their frequencies are close to the typical frequencies of pure CO_2 isotopomer ices [73, 74, 217], showing that the solid CO_2 product is formed. It is seen that the two CO_2 absorption bands grow monotonically. Plots of their integrated absorbance over time display the same slope, indicating that any ^{18}O isotope effect for CO is negligible.

3.3 Results and Discussion

3.3.1 Evidence for the Eley-Rideal type reaction

The rate of CO(g) consumption, R_{CO} (molecules m^{-2} s^{-1}), can be found by measuring the change of CO pressure (ΔP_{CO}) during UV irradiation. The ΔP_{CO} is directly proportional to R_{CO} in a rapidly pumped system [233], as shown in Equation 3.1 :

$$R_{CO} = \frac{\Delta P_{CO}\, S_{CO}}{A\, k_B\, T_g} \tag{3.1}$$

where S_{CO} is the measured pumping speed of CO(g), A is the irradiated sample area, k_B is the Boltzmann constant, and T_g is the CO gas temperature. At any CO pressure, the CO consumption rate during irradiation is proportional to the accumulated surface OH coverage, N_{OH}. When the reaction reaches steady state, the surface-bound OH production rate is equal to its consumption rate, including the OH reaction rate with CO(g), and the OH recombination rate with H or OH. Molecular dynamics studies show a large fraction of photo-produced H desorbs from the ice surface because of its weak binding energy [6], leaving an OH-enriched surface. We therefore postulate that the $OH + OH \rightarrow H_2O_2 \rightarrow H_2O + O$ reaction is the major process that consumes the excess OH [158]. After the interruption of the irradiation, the OH species remaining on the surface continue to be consumed by CO(g) and by the recombination reactions, resulting in a decrease of R_{CO}. An empirical fit with second-order kinetics gives $N_{\mathrm{OH}}^{\mathrm{SS}} = (4 \pm 1) \times 10^{17}\ \mathrm{m}^{-2}$ from the data in six measurements at steady state, corresponding to a fractional surface OH coverage of $\theta_{\mathrm{OH}}^{\mathrm{SS}} = 0.05$ ML (monolayer) at steady state.

The incident flux F_{CO} of CO(g) on the ice surface is calculated from the kinetic theory of gases using Equation 3.2:

$$F_{CO} = \frac{P^{\circ}_{\mathrm{CO}}}{(2\pi m k_B T_g)^{1/2}} \tag{3.2}$$

where P°_{CO} is the total pressure of CO(g) before irradiation, and m is the mass of the CO molecule. Therefore, the cross section, σ_{CO}, for CO(g) reaction can be obtained as d[CO]/dt = $\mathrm{F}_{CO}\ \sigma_{CO}\ \mathrm{N}_{OH} = \mathrm{R}_{CO}$. The reaction cross section, σ_{CO}, is found to be 6×10^{-20} m^2, which is of the order of a geometrical molecular cross section, consistent with a direct E-R-type process.

When CO molecules strike the ice surface, their average residence time can be calculated from Equation 3.3:

$$t_s = \frac{1}{\nu}\, e^{E_{des}/k_B T} \tag{3.3}$$

where ν is the desorption frequency factor $\approx 10^{12}$ s^{-1}, E_{des} is the CO desorption energy from the H_2O ice surface, and T is the ice temperature. The CO desorption energy from H_2O ice has been investigated experimentally and theoretically [1, 2, 42]. Because the CO coverage is low in our experimental conditions, we use E_{des} = 0.125 eV here [116]. Therefore at T = 76 K, the residence time for CO(g) on the H_2O ice surface is $\sim 2 \times 10^{-4}$ s. The fractional coverage of CO adsorbed on the ASW–H_2O ice surface at a given CO(g) pressure is $\Theta_{CO} = (\mathrm{F}_{CO} \times \mathrm{t}_s)/\mathrm{N}_{H_2O}$, where $\mathrm{N}_{H_2O} \approx 9 \times 10^{18}$ m^{-2} is the surface density of H_2O adsorption sites based on the density (0.94 g cm^3; [114]) of ASW. Under our experimental conditions, the CO fractional coverage is only $\Theta_{CO} = 1 \times 10^{-6}$ ML, i.e. five orders of magnitude smaller than the steady-state fractional OH coverage. This low coverage is consistent with the absence of the adsorbed CO IR absorption band. Thus, it is improbable under the conditions of the experiment for the reaction to occur by a mechanism where CO adsorbs on the surface and translates to an OH species.

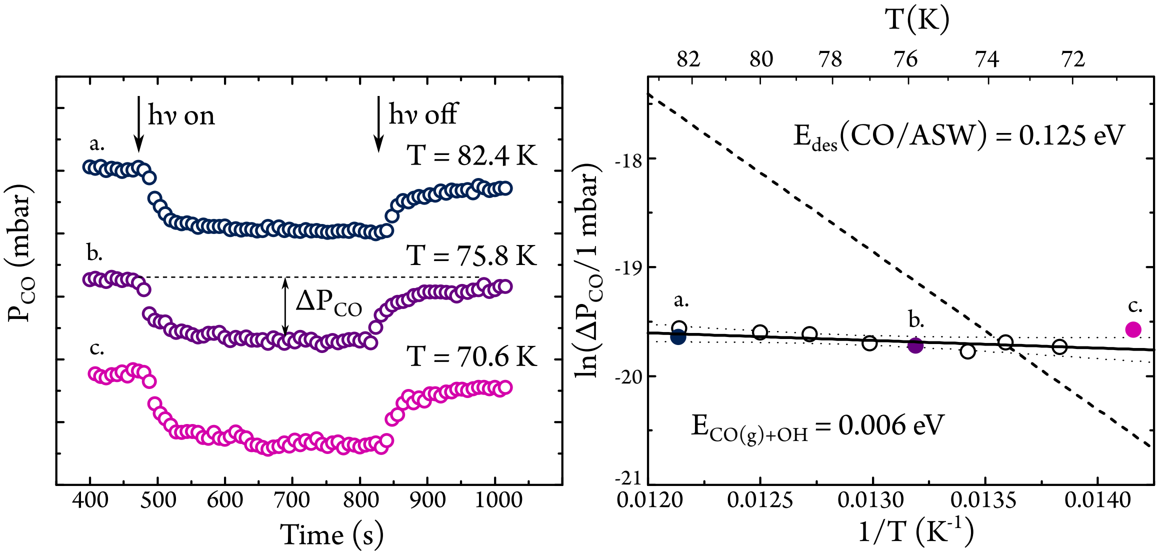

Figure 3.3.1: Temperature effect on CO(g) consumption rate between 70.6 K and 82.4 K. CO consumption is displayed for measurements at three temperatures. An Arrhenius plot of the data yields an activation energy of 0.006 eV. Ninety-five percent confidence intervals (dotted lines) on the weighted data show that the activation energy is zero within experimental error. The slope of Edes (CO/ice) = 0.125 eV is shown for comparison, and represents the expected temperature effect if the CO surface lifetime is rate controlling in the mobile precursor mechanism.

Figure 3.3.1 shows the temperature dependence of the reaction rate. As temperature decreases the CO consumption rate remains constant. This is additional evidence to support the E-R reaction mechanism. The measured activation energy of 0.006 eV, indicative of a zero activation energy within experimental error, implies that activated diffusion processes for CO is not kinetically significant at 76 K for the CO + OH reaction. The formation of the stable intermediate compound HOCO at unobservable concentrations is probably involved [7, 111].

It should be pointed out that in the ISM, competitive reactions may influence the overall results found here. The OH + OH reaction, the H + H reaction, the CO + H and CO + O reactions [111, 153, 157, 185] will change the relative importance of the CO(g) + OH reaction investigated here.

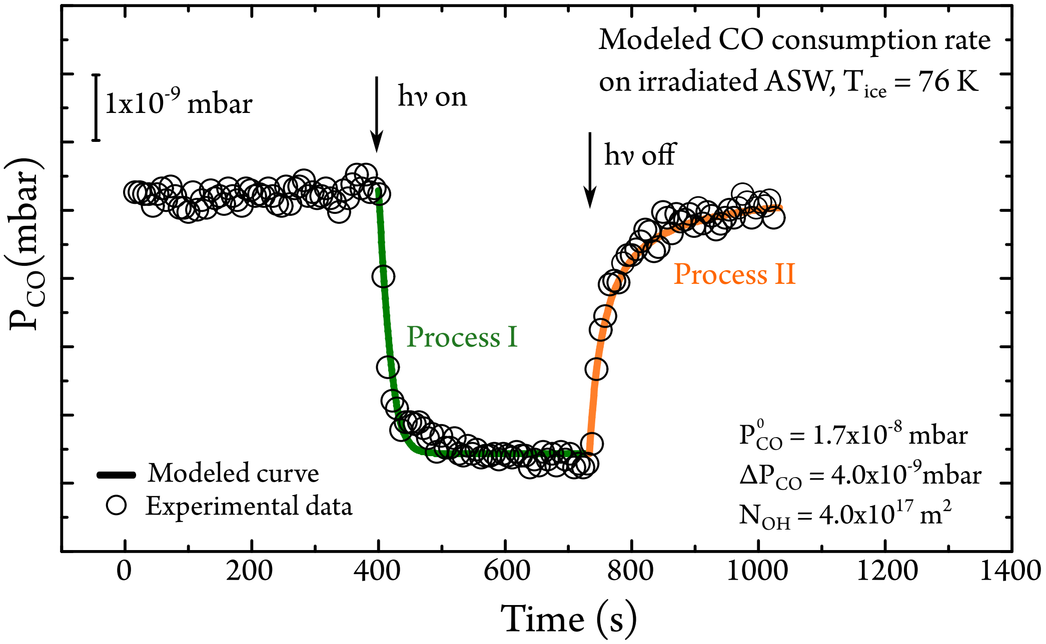

Figure 3.4.1: Modeled CO(g) consumption rate on irradiated ASW and its comparison to experimental data.

3.3.2 Advantage of the Method

The use of a mass spectrometer to observe the rate of processes occurring at an ice surface provides a highly sensitive kinetic method. Measurements of the CO reaction rates, such as those shown here, have a sensitivity of the order of 10^{-7} ML s^{-1} or $\sim 10^{12}$ molecules m^{-2} s^{-1}, whereas measurements of the photochemical rate of production of a molecule in the ice bulk, using the widely applied IR measurement method, have a sensitivity of only $\sim 10^{17}$ molecules m^{-2} s^{-1} if a strong vibrational mode is measured [234].

3.4 Kinetic Modelling

A kinetic model was used to fit the data of Figure 3.1.1 as shown in Figure 3.4.1. The model considers the flux of incident light, the cross section for H_2O photodissociation, and the incoming

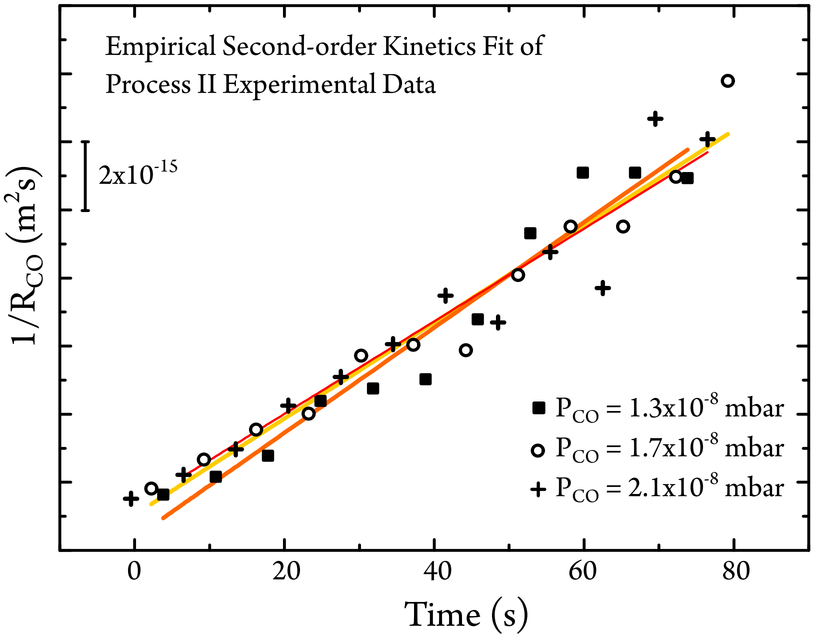

Figure 3.4.2: Empirical second-order kinetic fits of Process II experimental data.

flux of CO(g) in the system of known pumping speed to calculate the solid curve which is superimposed on the data for one measurement. It is found that the rate of the OH + OH reaction on the irradiated ice is mainly responsible for the shape of the P_{CO} curve, in agreement with the observation in Figure 3.1.1 that these curves are only weakly dependent on P°_{CO}. A schematic for the reaction of photo-produced OH with CO(g) via a direct E-R process is shown in the inset of Figure 3.4.1, along with the proposed second order recombination of the OH species.

To study the kinetics of the CO consumption process, CO(g) + OH → CO_2(ice)+ H, we divide the experimental CO pressure curves (as shown in Figures 3.1.1, 3.3.1, and 3.4.1) into two processes. Process I describes the CO pressure decay to steady state during irradiation and Process II describes the CO pressure recovery after irradiation ends.

As mentioned earlier, the CO(g) consumption rate, R_{CO}, is proportional to the initial CO pressure and the surface OH coverage, N_{OH}:

$$R_{CO} = \frac{\Delta P_{CO}\, S_{CO}}{A\, k_B\, T_g} = k_1 P_{CO} N_{OH} \tag{3.4}$$

Because of the observed weak dependence of R_{CO} on CO pressure, P_{CO}, and the zero activation barrier, we propose that the CO(g) + OH reaction only consumes a small portion of OH species on the surface. The majority of surface OH species are consumed by the competitive OH + OH second-order recombination process. This assumption is confirmed by the following analysis.

In Process II, we assume the OH consumption rate is simply determined by the CO(g) + OH reaction rate and by the OH + OH recombination rate, despite other complex processes that could occur in an irradiated water ice:

$$-\frac{dN_{OH}}{dt} = R_{CO} + R_{OH+OH} = k_1 P_{CO} N_{OH} + k_2 (N_{OH})^2 \tag{3.5}$$

Because the CO(g) + OH reaction rate is relatively slow, the OH consumption rate is approximately a second-order kinetic process in N_{OH}. The empirical second-order kinetic fits of $1/R_{CO}$ versus time from the experimental data are consistent for a range of pressures, as seen in Figure 3.4.2. We use this simplified second-order kinetics assumption in our further modeling.

By integrating Equation 3.5,

$$\int_{N_{OH}^{SS}}^{N_{OH}} \frac{dN_{OH}}{k_1 P_{CO} N_{OH} + k_2 (N_{OH})^2} = \int_0^t dt \tag{3.6}$$

where $N_{\mathrm{OH}}^{\mathrm{SS}}$ is the OH coverage during irradiation at steady state, we get

$$N_{OH} = \frac{k_1 P_{CO} N_{OH}^{SS}}{k_1 P_{CO}\, e^{k_1 P_{CO} t} + k_2 N_{OH}^{SS} (e^{k_1 P_{CO} t} - 1)} \tag{3.7}$$

In Process I, the steady-state OH consumption rate is equilibrated with its production rate by irradiation. The kinetic equation is

$$\frac{dN_{OH}}{dt} = F_{h\nu}\sigma_{H_2O}N_{H_2O} - k_1 P_{CO} N_{OH} - k_2 (N_{OH})^2 \tag{3.8}$$

where $F_{h\nu}$ is the flux of photons, $\sigma_{H_2O} = 1 \times 10^{-21}$ m^2 is the Lyα photodissociation cross section of H_2O gas [221], and N_{H_2O} is the surface density of H_2O molecules. Here we assume that only the first layer of water ice contributes to the surface OH production. Integrating Equation 3.8

$$\int_0^{N_{OH}} \frac{dN_{OH}}{F_{h\nu}\sigma_{H_2O}N_{H_2O} - k_1 P_{CO} N_{OH} - k_2 (N_{OH})^2} = \int_0^t dt \tag{3.9}$$

we get

$$N_{OH} = \frac{2c\left(1 - e^{\sqrt{k_1^2 P_{CO}^2 + 4k_2 ct}}\right)}{k_1 P_{CO}\left(1 - e^{\sqrt{k_1^2 P_{CO}^2 + 4k_2 ct}}\right) - \sqrt{k_1^2 P_{CO}^2 + 4k_2 c}\left(1 + e^{\sqrt{k_1^2 P_{CO}^2 + 4k_2 ct}}\right)} \tag{3.10}$$

where $c = F_{h\nu}\sigma_{\mathrm{H_2O}}N_{\mathrm{H_2O}} \approx 2 \times 10^{16}$ m^{-2} s^{-1}.

At steady state,

$$F_{h\nu}\sigma_{H_2O}N_{H_2O} = k_1 P_{CO} N_{OH}^{SS} + k_2 (N_{OH}^{SS})^2 \tag{3.11}$$

Here we assume a steady-state surface OH concentration, $N_{\mathrm{OH}}^{\mathrm{SS}}$, so that the rate constants k_1 and k_2 can be calculated from Equations 3.4 and 3.11. These rate constants are used in Equations 3.7 and 3.10 to model the curves to best fit the experimental data.

The value of $N_{\mathrm{OH}}^{\mathrm{SS}}$ can be estimated from the empirical second-order kinetics fit in Figure 3.4.2, and then be slightly adjusted to best fit the experimental data. An optimum $N_{\mathrm{OH}}^{\mathrm{SS}} = (4 \pm 1) \times 10^{17}$ m^{-2} is obtained from the data of six measurements. The fitting result is shown in Figure 3.4.1 for one experiment. The modeled curve for Process II fits the experimental

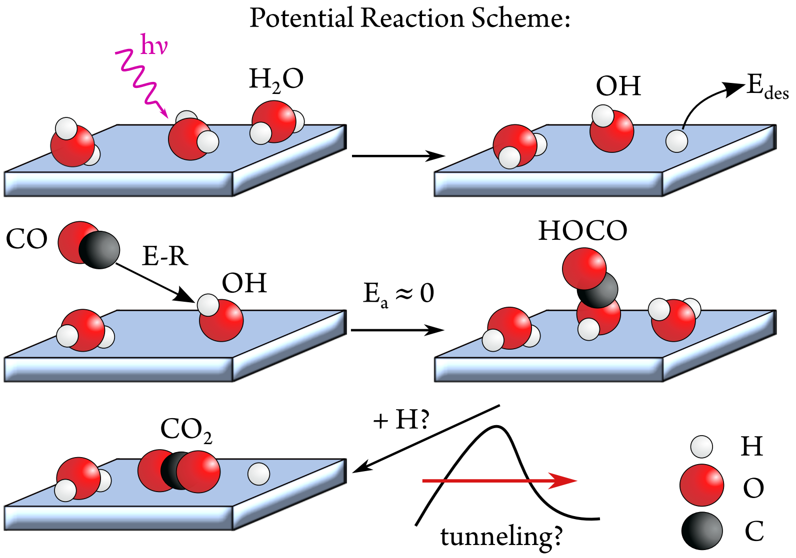

Figure 3.4.3: Schematic showing the kinetics of the CO(g) + OH Eley-rideal reaction. The reaction is hypothesized to occur via the HOCO intermediate, which then forms CO_2 either by tunneling or by reaction with neighbouring H atoms.

data well, while the curve for Process I has a small deviation from the data when P_{CO} approaches the steady state. This may be rationalized by postulating a small contribution from slow diffusion of OH from the underlying layers of the water ice [6]. Since the Lyα light penetrates into the ice, the diffusing OH species produced in the bulk may contribute to the surface OH concentration, causing a slightly increasing CO consumption rate as one moves to longer times in the plateau region of Figures 3.1.1 and 3.4.1.

With the calculated values of k_1 and k_2, the OH consumption rate by the CO(g) + OH reaction and by the OH+OH recombination are 3% and 97% of the total OH production rate by irradiation at steady state, respectively. Therefore our previous assumptions that the CO(g) + OH reaction rate is relatively small and that the OH consumption rate can be simplified as a second-order kinetic process are reasonable.

Figure 3.4.3 shows a summary of the proposed reaction scheme. An incident UV-photon (10.2 eV) photodissociates water molecules at the ice surface producing hydrogen and hydroxyl radicals. The hydrogen radicals desorb (either as H or H_2) leaving behind an OH-enriched surface. Gas-phase CO molecules collide with the surface OH radicals and react by an Eley-Rideal type mechanism with a measured reaction barrier of 0.006 eV. The reaction likely proceeds via the HOCO intermediate, which then forms CO_2 by tunneling through the exit channel barrier, or by reaction with neighboring surface species such as H radicals.

3.5 CONCLUSIONS

In summary we have observed the reaction between photochemically produced surface-bound OH species and incident CO(g) molecules at water ice surfaces between 71 and 82 K. The reaction is found to occur by a direct Eley-Rideal mechanism where a CO(g) molecule collides and reacts directly with a surface OH species to produce CO_2(ice). This observation may explain the origin of some of the CO_2(ice) observed in astrophysical environments as well as the CO consumption in the atmospheres of icy moons. Our experiments demonstrate a new process to convert CO(g) to CO_2 by reaction with surface OH species on astronomical ices.

4

CO_2 Infrared Phonon Modes in Interstellar Ice Mixtures

Modified from: Ilsa R. Cooke, Edith C. Fayolle and Karin I. Öberg, 2016, *ApJ*, 832, 5.

CO_2 ICE is an important reservoir of carbon and oxygen in star and planet forming regions. Together with water and CO, CO_2 sets the physical and chemical characteristics of interstellar icy grain mantles, including desorption and diffusion energies for other ice constituents. A detailed understanding of CO_2 ice spectroscopy is a prerequisite to characterize CO_2 interactions with other volatiles both in interstellar ices and in laboratory experiments of interstellar ice analogs. We report laboratory spectra of the CO_2 longitudinal optical (LO) phonon mode in pure CO_2 ice and in CO_2 ice mixtures with H_2O, CO, O_2 components. We show that the LO phonon mode position is sensitive to the mixing ratio of various ice components of astronomical interest. In the era of JWST, this characteristic could be used to constrain interstellar ice compositions and morphologies. More immediately, LO phonon mode spectroscopy provides a sensitive probe of ice mixing in the laboratory and should thus enable diffusion measurements with higher precision than has been previously possible.

4.1 INTRODUCTION

In cold regions of the interstellar medium dust grains are coated with ices – H_2O, CO, CO_2 and additional minor ice constituents – through a combination of condensation and an active surface chemistry. These ices account for up to 60 and 80% of the volatile oxygen and carbon budget in star forming regions respectively [166]. Of the three major ice constituents, this study focuses on CO_2. CO_2 is an important ice component during all stages of star formation. CO_2 ice has been observed in dense clouds [17, 119, 155, 229, 230], protostellar envelopes [5, 23, 60, 180, 201] and in comets [172], the remnants of the Solar Nebula. In this range of environments, CO_2 abundances with respect to water is surprisingly constant at 20–30%.

Interstellar and cometary CO_2 identifications as well as column density determinations rely on infrared spectroscopy. CO_2 ice has two IR active fundamental modes: the 4.27 μm stretch (ν_3) and the 15.2 μm bending (ν_2) modes, both of which have been identified in ices observationally. Furthermore, CO_2 ice spectra have been shown to depend sensitively on the local ice environment. The 15.2 μm band displays a characteristic Davydov splitting in the pure crystalline phase. Amorphous CO_2 ice and CO_2 in ice mixtures do not show this splitting, and the band is typically shifted with respect to the pure ice band position. The frequency and shape of the CO_2 ν_3 stretch also depend on the bulk ice structure. Several studies have pointed out that the band displays a low frequency shoulder at 2328 cm^{-1} (4.30 μm) in pure amorphous CO_2 and in some CO_2 mixtures with hydrogen-bonding molecules [67, 73, 94]. This environmental sensitivity has been used to identify several different CO_2 ice phases in observational spectra: in star forming regions, most CO_2 is typically mixed with water, but CO:CO_2 and pure CO_2 ice phases are also

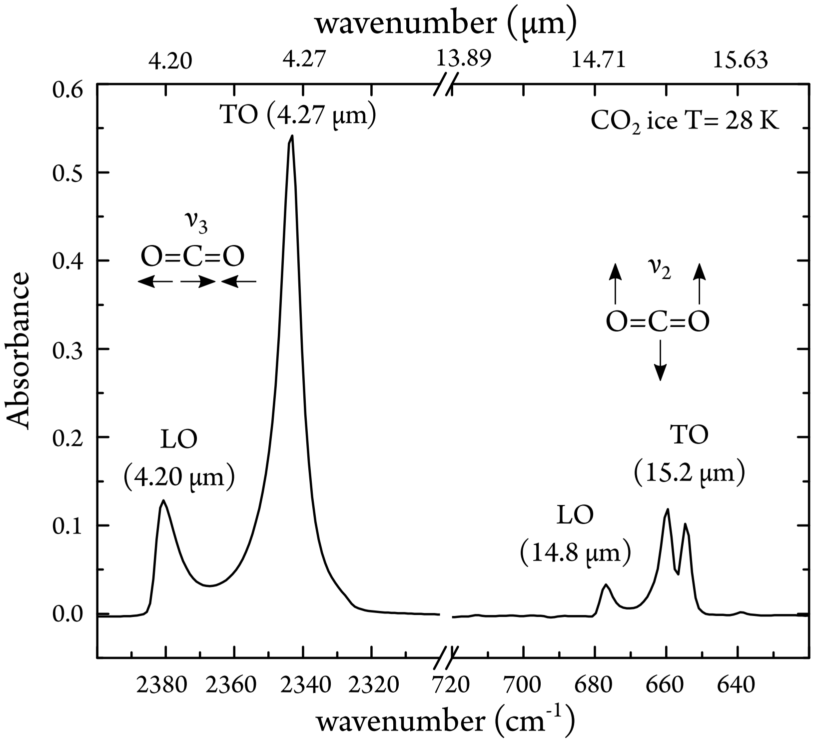

Figure 4.1.1: Infrared spectrum of pure CO_2 ice deposited on KBr at 28 K at 40° grazing angle to the IR beam. The two strongest spectral features are shown, the CO_2 asymmetric stretch (ν_3) at 4.27 μm and the CO_2 bend (ν_2) centered around 15.2 μm.

common [180, 228]. CO_2 ice spectroscopy has also been used in the laboratory to trace CO_2 trapping, segregation and diffusion processes [68, 69, 162, 175].

In addition to the normal vibrational modes, CO_2 optical phonons, arising from long range collective vibrations in the solid, can be excited by infrared radiation. A phonon is a quantized vibrational motion in which the lattice atoms or molecules vibrate at a single frequency. Optical phonons occur when the molecules are moving out of phase within the lattice. These phonons can propagate through thin films of astronomical dimension but cannot travel through films of thickness much greater than the wavelength of incoming radiation. Thick films will instead exhibit Restrahalen bands in which the change in the refractive index results in a strong reflection. Solid CO_2 exhibits both tranverse optical (TO) and longitudinal optical (LO) phonons in which the normal vibrations propagate through the ice lattice perpendicular and parallel to the direction of the IR field respectively. When a thin film is positioned at an oblique angle to the incoming radiation, the electric field has components both parallel and perpendicular to the film normal and longitudinal optical phonons can be excited by the parallel component of the field vector. The angular dependent enhancement of the LO mode is known as the Berreman effect after experiments conducted by Berreman on the angular dependence of the LO mode in ionic crystals [21].

The theory of optical phonon mode splitting has been described previously for polycrystalline films [174]. The magnitude of the splitting is estimated by:

$$\nu_{LO}^2 - \nu_{TO}^2 = \frac{4\pi}{\varepsilon m V}\left(\frac{\partial\mu}{\partial q}\right)^2 \tag{4.1}$$

where ν_{LO} and ν_{TO} are the frequencies of the LO and TO phonon modes, ε is the dielectric constant of the ice, m is the reduced mass associated with the coordinate q, V is the unit cell volume and $\partial\mu/\partial q$ is the transition dipole moment matrix element.

In many cases the splitting can be accurately described by the Lyddane-Sachs-Teller (LST) relationship:

$$\frac{\nu_{LO}}{\nu_{TO}} = \sqrt{\frac{\varepsilon_0}{\varepsilon_\infty}} = \frac{n_0}{n_\infty} \tag{4.2}$$

where n_0/ε_0 and $n_\infty\ /\varepsilon_\infty$ are the limiting low- and high-frequency refractive indices/ dielectric constants of the band. The high-frequency index is often approximated using the electronic dielectric constant, for example Hudgins et al. [110] use reported values of the visible refractive index of the sample at the sodium D line ($\lambda = 589$ nm). The values used by Hudgins *et. al.* for CO_2, O_2, CO and H_2O are $n_\infty = 1.22$, 1.25, 1.30 and 1.32. The LST approximation was originally developed for cubic crystals but has been shown to apply to a range of disordered materials

[202, 226, 227].

LO phonon modes are often invisible in laboratory ice spectra due to the common experimental setup in which the infrared beam is normal to the film surface. CO_2 LO-phonon modes have, however, been reported in Reflection-Absorption Infrared Spectroscopy (RAIRS) studies of ices, when the substrate is naturally positioned at a grazing angle to the IR beam. Baratta & Palumbo [10] report RAIR spectra of CO_2 ices at 12 K and show that new modes appear using p-polarized light at 2377 and 676 cm^{-1}.

[73] have also observed CO_2 LO phonons in both transmission IR and RAIRs experiments. They show that the CO_2 ν_3 mode in p-polarized RAIR specta shifts towards the LO frequency of pure crystalline CO_2 ice (2381 cm^{-1}) with increasing ice thickness.

The CO_2 ν_3 LO phonon mode has also been observed in ASW films exposed to CO_2 at 90 K [121] and for H_2O/CO_2 nanoparticles at 80 K [208]. CO_2 deposited on amorphous solid water (ASW) ice at 90 K exhibits an LO mode at 2379 cm^{-1}, close to that of pure CO_2 ice. Composite H_2O/CO_2 nanoparticles show shape effects which manifest in the IR at frequencies between ν_{LO} and ν_{TO}.

In this paper we present infrared transmission spectra of the CO_2 optical phonon modes in low temperature ices. We demonstrate that the LO phonon mode shape and peak frequency depends sensitively on ice mixing components, such as H_2O, CO and O_2. We analyze these dependencies and find a systematic frequency shift with ice mixing ratio for all mixing-partners, regardless of whether the ice mixture is deposited directly, or produced photolytically *in situ*. In section 6.5, we discuss how these spectroscopic characteristic could be used to characterize CO_2 in astrophysical environments, as well as in laboratory ice experiments aimed at constraining ice diffusion.

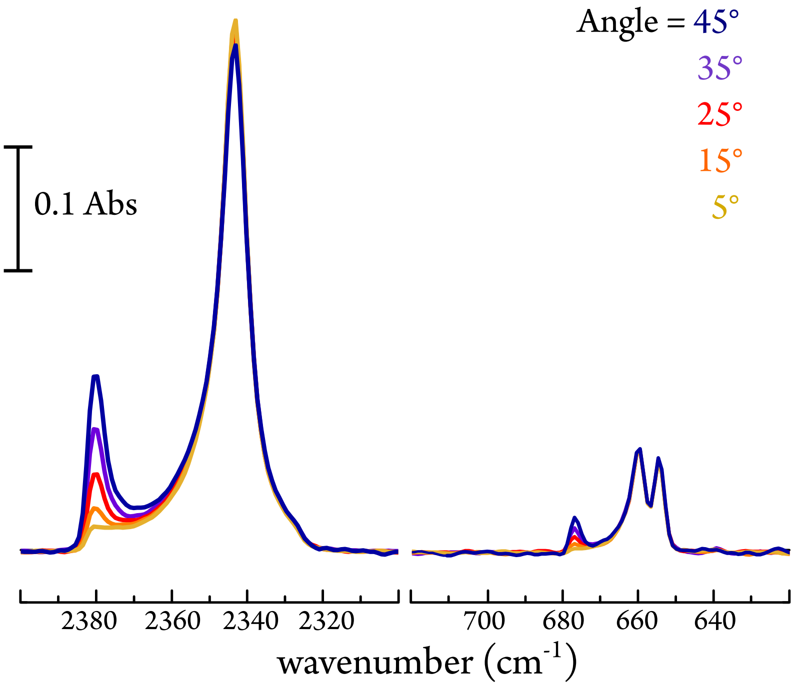

Figure 4.1.2: Angular dependence of the infrared spectrum of pure CO_2 ice deposited on KBr at 28 K. The IR spectra are shown for the ice films positioned at angles of 5-45° between the surface normal and the incident IR beam. The LO phonon mode intensity decreases as the angle between the IR-beam and the surface normal is decreased.

4.2 METHODS

Laboratory ice studies were conducted in a high vacuum system (base pressure $\sim$2 x 10^{-8} Torr, dominated by H_2) modified from Yuan & Yates [234]. A closed cycle helium cryostat (Air products Displex DE 202-0SP expander and APD Cryogenics HC-4 compressor) was added to cool the IR transparent substrate, a 0.3 cm^2 KBr pellet pressed into a tungsten grid that is suspended into the chamber by an OFHC copper coldfinger. The substrate is cooled to 28 K and the temperature is monitored using a k-type thermocouple welded to tantalum foil and attached to the W-grid close to the KBr pellet. Infrared spectra were collected using a Bruker Tensor 27 FTIR spectrometer and a liquid-N_2 cooled MCT detector. In the fiducial experiment the

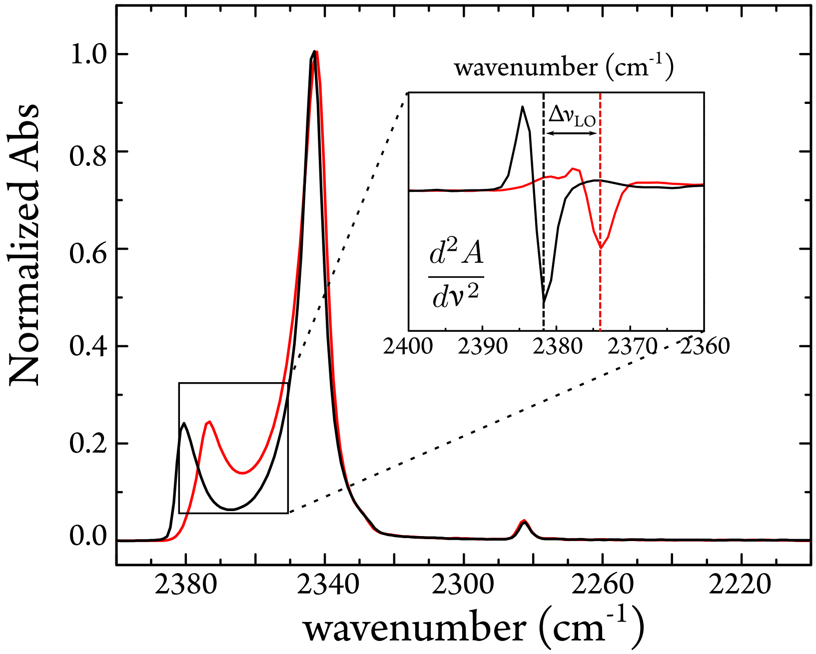

Figure 4.2.1: Infrared spectra of pure CO_2 ice (black) and a CO_2:CO mixed ice (red). The inset shows the second derivative spectra that are used to determine the frequency of the LO phonon mode. The redshift of the LO phonon mode is calculated as the difference between the LO frequency in pure CO_2 and in the mixed ice.

substrate was kept at ∼40° to the IR beam, but other angles were explored as well.

H_2O was prepared in a He-purged glove-box and freeze-pump-thawed for several cycles. The purity of the CO_2, CO, O_2 and H_2O used to prepare the ice mixtures was checked prior to the experiments using an RGA 200 quadrupole mass spectrometer (QMS). Ice mixing ratios are calculated using infrared absorption spectra and literature band strengths [89, 161] when possible, i.e. for H_2O, CO_2 and CO. Uncertainties on ice mixing fractions are calculated by analysis of repeat absorbance spectra of the ice mixtures and the pure ice, combined with a 15% uncertainty in the bands strengths used to calculate the ice mixing fraction. Molecular oxygen is not observed in the infrared due to absence of a permanent dipole. Oxygen is mixed with CO_2 in the gasline and the measured O_2 gas fraction was used to approximate the ice mixture. The gas fraction was measured by monitoring the O_2 and CO_2 partial pressures with the QMS at m/z =

32 and 44 respectively.

For photochemistry experiments, a microwave discharge hydrogen flow lamp (Opthos Instruments) was used. It has been described in detail previously [181]. The microwave power was kept at 60 W for the duration of the experiments. A mixture of 90% Ar, 10% H_2 was used to produce UV light with a sharp Lyman-alpha feature [168].

4.3 RESULTS

Figure 4.1.1 shows the infrared spectrum of pure CO_2 ice at 28 K, taken with the substrate at 40° to the incident IR beam. The LO phonon mode appears at 2381 cm^{-1} (4.2 μm) and is shifted from the ν_3 (TO) mode by 39 cm^{-1}. The CO_2 ν_2 mode also exhibits an LO phonon mode at 677 cm^{-1} (14.8 μm), split 17 cm^{-1} and 22 cm^{-1} from the CO_2 doublet peaks at 660 and 655 cm^{-1} respectively. The LO phonon mode disappears as the ice film is rotated such that its plane of incidence is parallel to the IR beam (figure 4.1.2). The CO_2 ices deposited at 28 K have crystalline spectral characteristics including splitting of the ν_2 mode and both the frequency and bandwidth of ν_3 mode, as well as an amorphous feature around 2328 cm^{-1} that dominates at low coverage. The CO_2 ices in each of the experiments are 70-90 nm thick, calculated by integrating the $\nu_1 + \nu_3$ mode using the band strengths of Gerakines et al. [89] and a density of 1.78 g/cm^3 as reported for crystalline CO_2.

Figure 4.2.1 shows the method for determining the $\Delta\nu_{LO}$ by analysis of spectra of the ice mixtures and pure CO_2 ices. The ν_{LO} frequency is found by identifying the minimum in the second derivative spectrum. Second derivative spectra were taken in both the Opus software and Thermo Scientific Grams/AI Spectroscopy software. A smoothing function was applied in Opus software before taking the second derivative. The frequencies of the ν_{LO} modes from the smoothed spectra in Opus agreed within 1% with those determined using Grams without

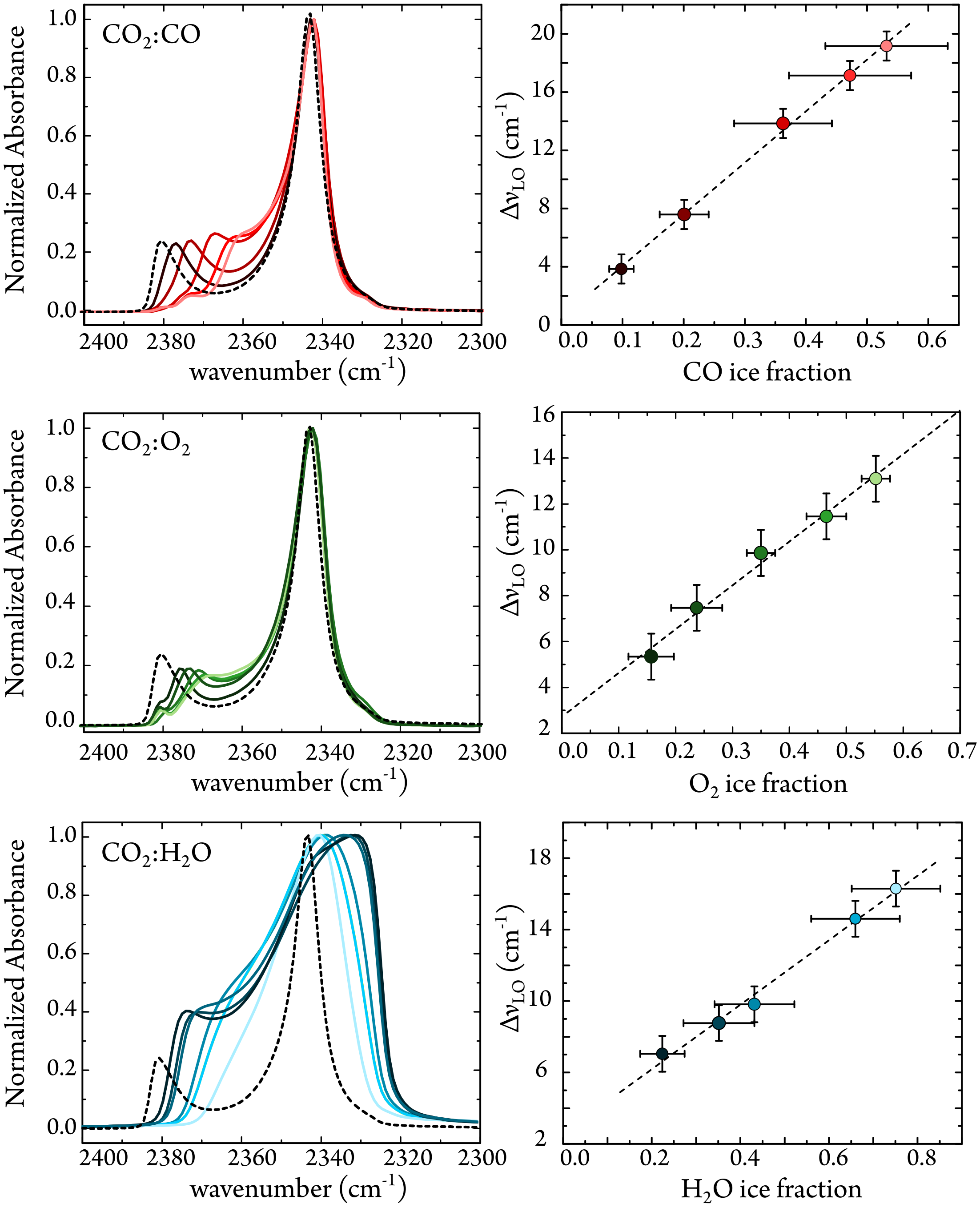

Figure 4.3.1: *Left*: Spectra of (top: CO, middle: O_2, bottom: H_2O) CO_2 ice mixtures deposited from gas mixtures at 28 K. The dashed line shows the spectrum of pure CO_2 ice. The CO_2 LO phonon mode redshifts with increasing defect fraction in the ice. *Right*: Shift of the LO phonon mode with respect to pure CO_2 ice for various concentrations of the defects in CO_2 ices.

Table 4.3.1. Measured CO_2 LO phonon frequencies and redshifts from pure CO_2 ice ($\Delta\nu_{LO}$) for CO_2 ice mixtures of different mixing fractions

Ice	Mixing Fraction	ν_{LO} (cm^{-1})	$\Delta\nu_{LO}$ (cm^{-1})
CO_2:CO	0.10±0.02	2377.0	3.9
	0.20±0.04	2373.3	7.6
	0.36±0.08	2367.0	13.8
	0.47±0.10	2363.7	17.1
	0.53±0.10	2361.7	19.2
CO_2:O_2	0.16±0.04	2375.5	5.3
	0.24±0.05	2373.4	7.5
	0.35±0.03	2371.0	9.9
	0.47±0.04	2369.4	11.5
	0.55±0.03	2367.8	13.1
CO_2:H_2O	0.22±0.05	2373.8	7.0
	0.35±0.08	2372.1	8.8
	0.43±0.09	2371.0	9.8
	0.66±0.10	2366.3	14.6
	0.75±0.10	2364.6	16.3

smoothing. The uncertainty on $\Delta\nu_{LO}$ is conservatively taken as the spectral resolution (± 1 cm^{-1}).

The CO_2 experimental spectra and ν_3 LO mode redshifts versus defect ice fraction for CO, O_2 and H_2O ice mixtures are displayed in Figure 4.3.1 and Table 4.3.1. Figure 4.3.1 shows the effect of introducing CO, O_2 or H_2O into the CO_2 ice lattice by mixing with CO_2 prior to deposition. Increasing the fraction of the defect species in the CO_2 ice results in an increasing redshift of the LO phonon mode from the pure ice position. The right panels of figure 4.3.1 present the ν_{LO} redshift versus the fraction of each species in the CO_2 ice mixture. These plots display a positive linear correlation between the defect concentration and the LO redshift for each of the ice mixtures considered. The slope of the ν_{LO} redshift versus the defect fraction are 36 ± 7 cm^{-1} N$_{CO}$/N$_{total}$, 19 ± 4 cm^{-1} N$_{O_2}$/N$_{total}$ and 18 ± 4 cm^{-1} cm^{-1} N$_{H_2O}$/N$_{total}$ for CO, O_2 and H_2O ice mixtures respectively. The effect of the ice defect on the position of the LO mode may be quantified by comparing these slopes. For example, we would expect the LO mode to shift by 1 cm^{-1} if the CO_2 ice contains ~3% CO, ~5% O_2 or ~6% H_2O.

In addition to shifting the frequency of the LO mode, the three mixing partners also affect the shape of the LO mode spectral band, and these spectral changes are species specific. In CO mixtures with CO_2, a second small peak appears in the spectra of mixtures with more than 30% CO. This peak is also redshifted from the pure LO phonon mode position but does not appear to shift with CO concentration beyond 30%, possibly representing a stable mixing environment between CO and CO_2 such as the formation of a complex.

A similar second peak is present in all of the mixed O_2:CO_2 ice spectra. The spectra of H_2O mixtures with CO_2 differ from those of the CO and O_2 mixtures in several ways. In particular, the spectra of CO_2 in polar H_2O environments show broadening of the ν_3 mode as well as non-linear dependence of the ν_3 frequency on the fraction of H_2O in the ice.

The CO_2 bending mode for the ice mixtures are shown in Figure 4.3.2. The LO phonon mode is split from the ν_{2b} mode at 660 cm^{-1} by 17 cm^{-1}, while the ν_{2a} peak at 655 cm^{-1} does not display appreciable LO/TO splitting. The ν_2 LO mode behaves similarly to the ν_3 mode, with linear shifts that are dependent on the fractional abundance of the defect in the ice. The redshift is likewise the largest for CO ice mixtures with respect to the ice fraction. Both CO and O_2 ice mixtures display decreased Davydov splitting of the ν_2 band with respect to the pure CO_2 ices. The ν_2 bands in H_2O mixtures are broad and do not display Davydov splitting, due to the effect of the hydrogen bonding network of the H_2O lattice on the CO_2 crystal structure. The decrease of Davydov splitting in the ice mixtures supports the fact that the CO_2 crystal structure is disrupted upon addition of the defect molecules as pairwise binding interactions between CO_2 and the

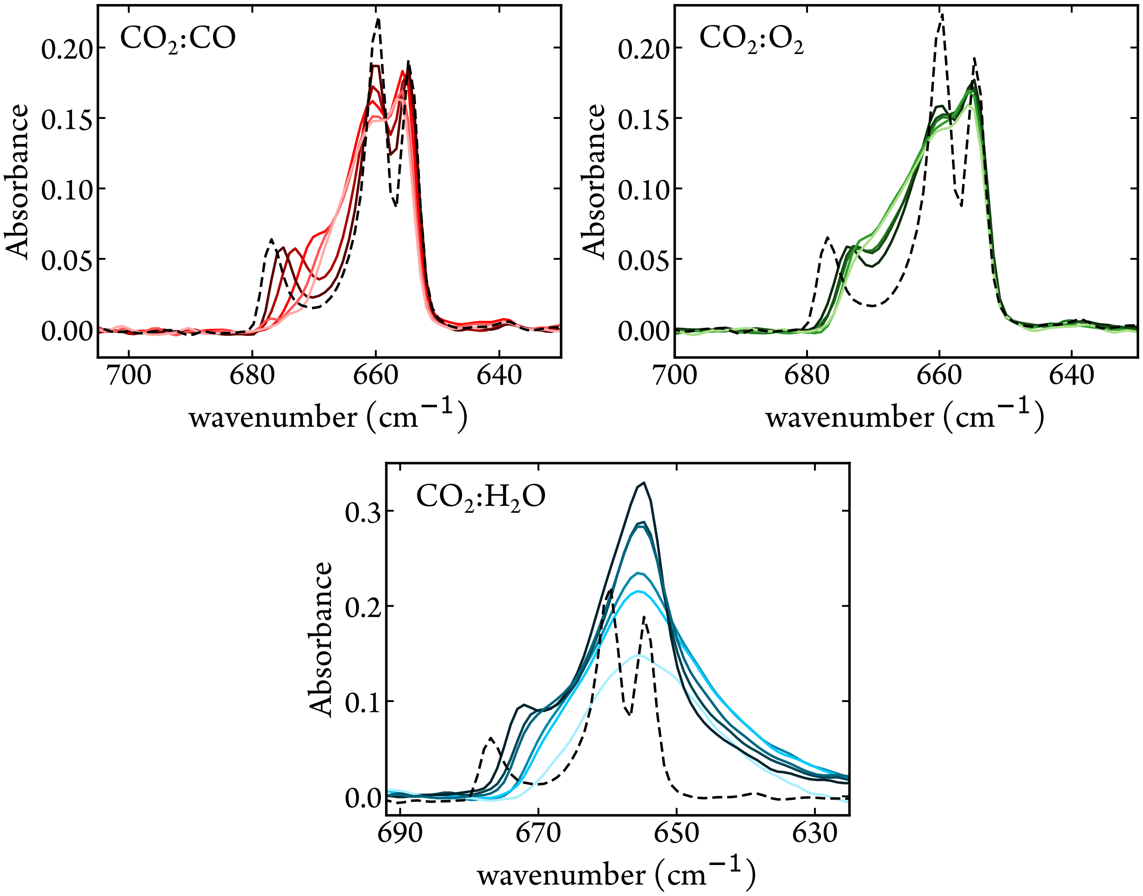

Figure 4.3.2: CO_2 bending modes for CO:CO_2 mixtures, O_2:CO_2 mixtures and H_2O:CO_2 mixtures . The colors correspond the mixing ratios shown in Figure 4.3.1

introduced molecule can result in only one equivalent CO_2 per unit cell. This is consistent with the fact that the Davydov splitting continues to decrease in the ice mixtures with increasing concentration of CO or O_2 as more interactions become available in each unit cell.

We also conducted experiments to measure the introduction of defects *in situ* by UV irradiation of pure CO_2 ices, which is known to produce CO. Figure 4.3.3 shows spectra of pure CO_2 ice irradiated with UV photons from a hydrogen discharge lamp for a period of 140 minutes. The CO_2 LO phonon mode clearly redshifts with exposure time. The redshift is linear with CO photoproduct growth, similar to when a defect is introduced through pre-mixing. There are two differences in the LO phonon mode shifts in these experiments compared to the pre-mixed experiments, however. First, the LO phonon mode depends more steeply on CO concentration in the ice with a linear fit of 54 ± 6 cm^{-1} N_{CO}/N_{total} compared to the pre-mixed case which gives a fit of 36 ± 7 cm^{-1} N_{CO}/N_{total}.

Second, the photolyzed phonon mode is split into the redshifted (CO:CO_2 mixture) component and a second component that remains at the pure CO_2 LO phonon frequency. This suggests that some pure CO_2 is present throughout the photolysis experiment. To test whether this may be due to limited Ly-α penetration depth through the ice, we also photolysed a ∼10 nm thick CO_2 ice while monitoring the LO phonon mode; the penetration depth of 10.2 eV photons through CO_2 ice has been previously measured in our laboratory as 50 nm [234]. Figure 4.3.4 shows that photolysis of the thin ice also results in a split LO phonon mode, with one peak that can be ascribed to pure CO_2 and another to a CO:CO_2 ice mixture, demonstrating that the second peak cannot be due to a limited photon penetration depth. Furthermore, the absorbance at the pure CO_2 phonon mode frequency (2381 cm^{-1}) plateaus after ∼20 minutes of irradiation, while the production of CO and destruction of CO_2 remains linear through the irradiation period. The plateau at the pure CO_2 LO frequency thus indicates that an environment exists in the ice in which the CO_2 is not mixed with the photoproducts and this hypothesis is further discussed in section 4.4.1.

4.4 DISCUSSION

4.4.1 EFFECTS OF CO, O_2 AND H_2O ON THE CO_2 LO PHONON MODE

The LO-TO splitting depends on long range dipole interactions between CO_2 molecules and therefore is perturbed by the addition of other species into the ice lattice. The magnitude of the

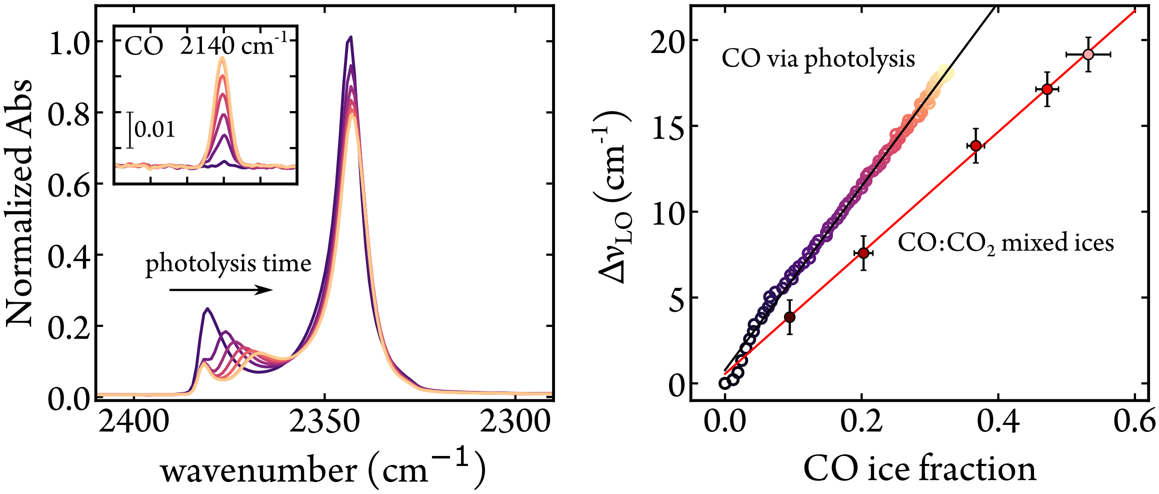

Figure 4.3.3: Photolysis of a pure CO_2 ice using 10.2 eV photons. The CO_2 ice spectra show redshifts in the LO phonon mode that correlate with the linear production of CO photoproducts (inset) and depletion of CO_2 ice. The linear shift of the LO mode for CO_2:CO mixed ices is shown in red for comparison.

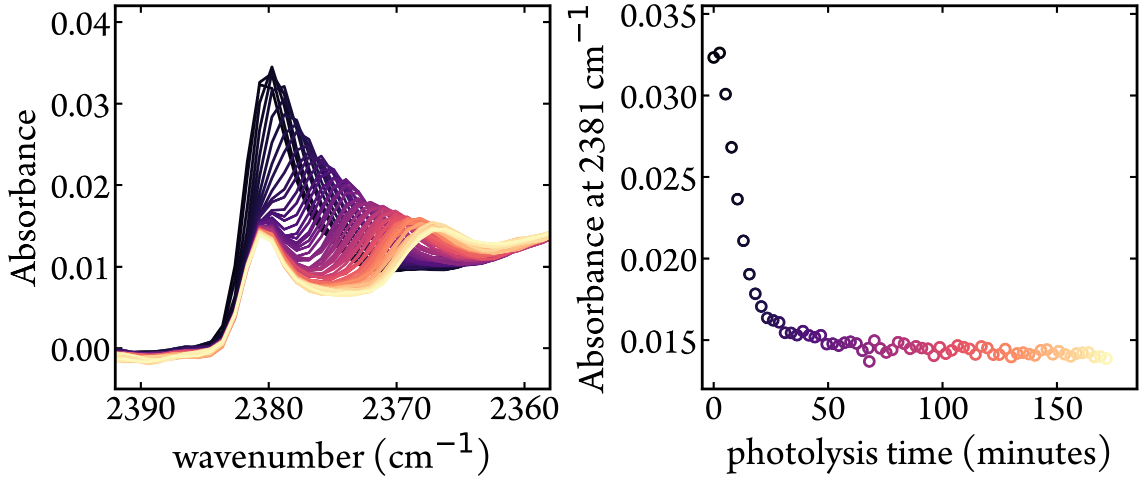

Figure 4.3.4: Photolysis of a pure CO_2 ice ~10 nm thick using 10.2 eV photons. The thin CO_2 ice spectra show redshifts in the LO phonon mode similar to that seen for the thicker ice. The RHS shows the absorbance at 2381 cm^{-1} over the irradiation period. The residual phonon peak at 2381 cm^{-1} plateaus after ~20 minutes of irradiation.

LO-TO splitting depends on the ice physical structure and bonding, the optical properties of the ice and the transition dipole moment of the CO_2 normal modes. Thus, the LO redshift upon addition of CO, H_2O and O_2 into the CO_2 ice lattice is a combination of how each of these species changes structure, binding energies, dielectric constant and transition moments of the CO_2 molecules within the lattice.

According to equation 4.1, the transition dipole moment governs the LO-TO splitting in polycrystalline films. The CO_2 asymmetric stretch has a large transition dipole matrix element, consistent with the large LO-TO splitting in pure CO_2 ice. One might expect that differences in the redshifts of the CO_2 LO frequency correspond to differences in the effects of the transition dipole elements of CO, H_2O and O_2 on that of the CO_2 LO mode. CO, while exhibiting only a small dipole moment, has a very large transition dipole moment that could perturb the effective CO_2 transition element. While H_2O has a large transition dipole, O_2 has μ=0 for all internuclear separations and therefore its transition dipole moment is zero everywhere. If the changes in the CO_2 transition dipole moment were the only explanation for the LO redshift we would expect that O_2 would not shift the LO frequency and that CO and H_2O would have similar LO redshifts, which is not the case in our measurements. We therefore consider other effects on the LO-TO splitting.

The addition of CO, O_2 and H_2O affects the CO_2 ice physical structure. Changes in the crystal structure can shift the LO mode to lower frequencies as shown for different CO_2 ice nanostructures [208]. Our data suggest that CO has the greatest effect on the longitudinal phonon frequency in CO_2 ice. Despite the substantially lower binding energy to CO_2 compared to H_2O, CO may produce the observed large shift because it is able fit well into the CO_2 ice lattice so that each CO_2 molecules in the lattice has dipole interactions with more CO molecules than in the case of H_2O; however, detailed structural simulations are required to constrain the exact mechanism.

Splitting of the LO phonon into more than one band indicates that the mixing is not homogeneous and distinct CO_2 bulk environments are present in the ice. This may be caused by CO_2 segregation away from the defect ice component. Figure 4.3.1 shows splitting of the LO mode in the CO_2:O_2 ice mixtures and in the CO_2:CO mixtures with high CO abundance. In the H_2O mixtures, the LO mode at the pure CO_2 frequency is absent, this suggests that the CO_2 is mixed in the H_2O ice lattice such that pockets of pure CO_2 do not occur. This is expected as CO_2 diffusion through H_2O is slow at 28 K [162] while diffusion and segregation of CO and O_2 may be possible, though further experiments are needed to support this hypothesis.

We see the clearest splitting of the LO mode in the photolysis of CO_2 ice, where one component stays at the pure CO_2 LO position. As demonstrated by the thin ice photolysis experiment, this is not due to shielding of the UV radiation for the deepest ice layers. Instead, pockets of pure CO_2 must either be maintained or produced during the photolysis. Only $\sim$20% of the CO_2 ice is lost during the photolysis period. It is possible that some of the leftover CO_2 is not mixed with the photoproducts and maintained as pure CO_2 ice. Pure CO_2 could also be produced during the photolysis by several mechanisms. Excited CO_2 that is not photolysed carries excess energy that may allow it to segregate away from the photoproducts to form pure CO_2 pockets. CO_2 is also reformed during the photolysis by CO + O recombination and CO_3 dissociation. Another possible explanation is the desorption of photoproducts that are formed in the surface layers, leaving behind pure CO_2. This hypothesis could be investigated further by studying the molecules desorbing from the ice during the photolysis, by using isotopically labeled layers or by capping the CO_2 ice with an inert gas matrix.

4.4.2 Potential Laboratory Applications of Phonon Mode Spectroscopy

The sensitivity of the CO_2 LO phonon mode to ice mixing may be utilized in laboratory studies to provide information on bulk diffusion, physical mixing properties and ice phase properties such as crystallization. We have shown that the LO mode is particularly sensitive to the addition of ice defect molecules added either by deposition of gas mixtures or *in situ* by photolysis of the ice. Mixing may also occur through diffusion of molecules in the ice. Diffusion is proposed to underpin much of the chemistry in interstellar ices, but diffusion barriers and mechanisms are highly uncertain [84, 129]. Bulk diffusion may also regulate the morphology of interstellar ices. Diffusion of CO out of CO_2 ice may cause CO distillation from CO-rich ices protostellar regions, thus explaining the presence of pure CO_2 in some such lines of sight [73, 180].

We have conducted preliminary experiments to check whether the CO_2 LO mode could trace diffusion and desorption processes. The CO_2 ice mixtures were slowly heated passed the desorption temperature of CO or O_2 and the changes in LO mode were monitored. As the defect molecule desorbs, the LO phonon mode moves back toward the pure CO_2 frequency. The process is not completely reversible as some defect molecules remain trapped and desorb with the CO_2 ice around 75 K. This suggests that phonon mode spectroscopy could be used to characterize diffusion in CO_2 ices. Furthermore, phonon modes are not unique to CO_2 ice, and optical phonons in other ices may be used to measure diffusion coefficients for a range of astronomically relevant species.

Phonon mode monitoring may also be used to characterize ice crystallization. The Lyddane-Sachs-Teller relationship (equation 4.2) shows that the LO phonon mode should shift abruptly upon a phase change in the ice due to a rapid change in the static dielectric constant. Optical phonons in ices may therefore provide a useful measure of crystallization kinetics. The observed LO-TO splitting for ice deposited at different temperatures may be used to accurately deduce phase change temperatures and the corresponding index of refraction for ices around the phase change boundary.

4.4.3 Astrophysical Implications

Longitudinal optical phonon modes may contribute to interstellar ice spectra for several important ice constituents if light from the background source is sufficiently polarized. In laboratory reflection absorption spectra p-polarized light, parallel to the surface normal, can interact with longitudinal phonons in the ice. In astronomical environments longitudinal phonons can be excited by p-polarized light or by the component of the unpolarized light wave that is parallel to the surface normal. Because the interstellar ices are not confined to slabs, as in the case of laboratory experiments, the fraction of p-polarization and s-polarization is generally equal for randomly orientated dust particles. Unpolarized light will predominantly produce the TO mode, though it can also excite LO phonons when the incoming IR wave is at oblique angles to the ice surface as seen in our laboratory spectra (Figure 4.1.2). The best sources for observing longitudinal phonons in ices are therefore those with the highest linear polarization fraction. Linear polarization arises from absorption and scattering from irregular dust grains which will absorb light from the background star preferentially along one axis. Dust grains can align with a local magnetic field and produce elliptically polarized light with linear and circular components [131]. The degree of linear polarization in star forming regions is often very large ranging from 20-70% and can extend over regions as large as 1 pc [122, 123]. A good source to characterize interstellar CO_2 LO phonon modes would be, for example IRAS 05329-0505, for which Kwon et al. [123] measure the linear polarization fraction as 70% in the K_s band.

Optical phonon modes have been previously identified in laboratory spectra of H_2O and CO [10, 226, 227]. Water ice phonons are considered carriers of far infrared bands at 62 μm (longitudinal acoustic) and 44 μm (transverse optical) bands [58, 171], which can be observed with far-IR telescopes such as SOFIA. These bands are sensitive to the ice structure with the 62 μm appearing at the crystallization phase transition [152]. Spectra of CO bearing ices in 39 YSOs observed using the VLT have been fit using the optical phonon modes of α-CO [178]. Here, the LO mode was able to accurately reproduce the blue wing of the CO band for all of the observed sources. LO phonon modes thus needs to be taken into account when identifying the carriers of observed ice spectral features.

In the case of CO_2, identifying and characterizing the LO phonon mode in observed spectra could also provide important information about the ice composition, morphology and thermal history. Because the LO phonon mode is sensitive to defects in the CO_2 ice lattice, its frequency can be used to provide information about abundance of other species mixed with solid CO_2. In pristine CO_2 ice the LO mode will appear at 4.2 μm, if light from the background source is sufficiently polarized. For CO_2 ice in apolar and polar phases the LO phonon mode would be present at a redshifted frequency that is dependent on the fractional abundance of other ice components. A lack of LO-TO splitting in all ice species provides constraints on the source (polarization and dust properties), while a lack of LO-TO splitting in CO_2 when present in CO would constrain the CO_2 ice to be dilute, in which case the LO mode is convoluted with the TO mode.

To fit observational spectra, the CO_2 LO phonon spectra reported here need to be adjusted to account for grain size and shape effects. The standard method for treating grain shape and size variations has been to use a continuous distribution of ellipsoids (CDE) (e.g. Bohren & Huffman [22]). Ehrenfreund et al. [67] have shown that the size and shape of grains affect the CO_2 absorption profile causing typical shifts and broadenings of 5 cm^{-1} that can dominate over variations due to ice matrix effects. An in depth analysis of grain geometric effects on the CO_2 LO phonon mode will be needed to before it can be used to constrain ice mixing in observational spectra. Analysis of LO-TO splitting should be especially fruitful on future ice spectra acquired with the JWST, since the analysis requires both high sensitivity and spectral resolution.

4.5 CONCLUSIONS

We have shown that longitudinal optical phonons in CO_2 ices are particularly sensitive to the presence of other ice species in the lattice. The frequency of the CO_2 LO mode redshifts linearly as the concentration of the ice mixing molecule is increased. Similarly, photolysis of CO_2 ices results in a linear redshift of the LO phonon mode with formation of the major photoproduct, CO. These spectral signatures will be useful for constraining ice mixing both in laboratory experiments and in observations of astronomical ices.

I. R. C. acknowledges full fellowship support from the Department of Chemistry, University of Virginia. I. R. C. would like to acknowledge instrument design and machining by Matthew Reish and helpful conversations with Rob Garrod, Eric Herbst, Patrick King and Jennifer Bergner. I. R. C would like to acknowledge Jeffrey Shabanowitz for providing equipment used in producing these data. This work was conducted in the laboratory of the late John T. Yates Jr. to whom we would like to thank for his experimental techniques, motivation and mentorship leading to this study.

5

CO diffusion-desorption kinetics in CO_2 ices

Modified from: Ilsa R. Cooke, Karin I. Öberg, Edith C. Fayolle, Zoe Peeler and Jennifer B. Bergner, 2018, *ApJ*, 852, 75.

Diffusion of species in icy dust grain mantles is a fundamental process that shapes the chemistry of interstellar regions; yet measurements of diffusion in interstellar ice analogs are scarce. Here we present measurements of CO diffusion into CO_2 ice at low temperatures (T=11–23 K) using CO_2 longitudinal optical (LO) phonon modes to monitor the level of mixing of initially layered ices. We model the diffusion kinetics using Fick's second law and find the temperature dependent diffusion coefficients are well fit by an Arrhenius equation giving a diffusion barrier of 300 ± 40 K. The low barrier along with the diffusion kinetics through isotopically labeled layers suggest that CO diffuses through CO_2 along pore surfaces rather than through bulk diffusion. In complementary experiments, we measure the desorption energy of CO from CO_2 ices deposited at 11-50 K by temperature-programmed desorption (TPD) and find that the desorption barrier ranges from 1240 ± 90 K to 1410 ± 70 K depending on the CO_2

deposition temperature and resultant ice porosity. The measured CO-CO_2 desorption barriers demonstrate that CO binds equally well to CO_2 and H_2O ices when both are compact. The CO-CO_2 diffusion-desorption barrier ratio ranges from 0.21-0.24 dependent on the binding environment during diffusion. The diffusion-desorption ratio is consistent with the above hypothesis that the observed diffusion is a surface process and adds to previous experimental evidence on diffusion in water ice that suggests surface diffusion is important to the mobility of molecules within interstellar ices.

5.1 Introduction

The motion of atoms and molecules on and within icy grain mantles is a fundamental process that regulates the chemical evolution in astrophysical environments. Diffusion of these species within the bulk ice or along icy surfaces influences the rates of desorption, chemistry and ice reorganization. The interplay between diffusion and reaction of radical fragments within the ice is a critical factor to explain the existence and abundances of several complex organic molecules in star-forming regions [84, 88].

The diffusion of molecules in ice mantles is, however, poorly constrained. For most species and ice matrices, both the diffusion mechanism and the diffusion barrier are unknown. Astrochemical models therefore often adopt diffusion barriers that are fractions of the better constrained desorption barriers [31, 54, 85, 117, 188, 212]. Previous studies have explored diffusion-desorption barrier ratios between 0.3 and 0.8, and have demonstrated that the chemistry and ice composition is very sensitive to this parameter e.g. Garrod & Pauly [85]; experimental constraints of diffusion and desorption for several major ice species are essential to better understand the temperature dependent evolution of ices.

To obtain a complete understanding of diffusion in interstellar ices, data is required on diffusion in all common interstellar ice environments since molecular diffusion and desorption barriers are expected to depend strongly on the ice composition and morphology. Observations of ice absorption bands toward protostars indicate that the main ice constituents are H_2O, CO and CO_2. Furthermore, the ice mantles are typically divided into H_2O-rich and CO-rich phases, both of which are mixed with CO_2, as well as a pure CO_2 ice phase in some lines of sight [23, 57, 180]. To understand the importance of diffusion in astrophysically relevant ices, experiments and models are required for all three ice phases. Diffusion of molecules through H_2O ices has been the subject of several recent studies [116, 129, 136, 151]; however, diffusion in CO- and CO_2-rich ice environments has not been treated experimentally. Considering the differences between the ice matrices of CO- and CO_2-rich ices and the hydrogen-bonded, porous H_2O-rich ices, it is unclear whether the barriers and diffusion mechanisms in CO and CO_2 ices are similar to those found in the experiments with H_2O ices.

Molecular diffusion in astrochemical ice analogs has been studied predominantly by two methods: firstly, by diffusion-desorption experiments in which the decreasing IR absorbance of the diffusing species is recorded over time [116, 151]; and secondly, by spectroscopic techniques that exploit the fact that some IR bands are very sensitive to their molecular environment [129]. The latter effects have been shown to be strong when CO or CO_2 is mixed with hydrogen bonding molecules like water or methanol, producing blueshifts and broadening of the CO and CO_2 infrared modes [69, 162, 175, 191, 192]. However, the CO and CO_2 normal vibrational modes are not as sensitive to mixing with other, non-polar or weakly polar ice constituents, making diffusion measurements in these environments more challenging [67].

Recently, we have shown that CO_2 longitudinal optical (LO) phonons can be used to sensitively probe ice mixing characteristics including the amount of CO molecules that are mixed within CO_2 ices [46]. LO phonons arise in the CO_2 ice when the substrate is positioned at an oblique angle to the infrared beam. We found that the CO_2 LO phonons redshift linearly with the ice mixing fraction, suggesting that they may be utilized to study diffusion dynamics in CO_2 ices.

Here, we present a study of CO diffusion into CO_2 ices by measuring changes in the CO_2 ν_3 LO phonons. We also measure the desorption energy of CO from CO_2 ices and present the diffusion-desorption energy barrier ratio. Section 5.2 presents the experimental setup, procedures and spectral analyses used to study CO diffusion through CO_2 ices (5.2.2) and desorption from CO_2 ices by temperature-programmed desorption (TPD) (5.2.3). Section 5.3 presents the results of the diffusion experiments and their dependencies on ice temperature and thickness as well as the diffusion modeling strategies. In section 5.4 we outline the results and analysis of the TPD experiments and extract the desorption barriers for CO from CO_2 ices. The results and their astrophysical implications are discussed in Section 5.5.

5.2 Experimental Setup and Procedures

5.2.1 Experimental Setup

The experiments were conducted using the setup described previously in Lauck et al. [129]. Briefly, the setup consists of an ultrahigh vacuum chamber with a base pressure of $\sim 4\times 10^{-10}$ Torr at room temperature. The ices are deposited onto a CsI window cooled to as low as ~11 K using a closed-cycle Helium cryostat. These ices are grown using a 4.8 mm gas doser that is positioned close to the CsI subtrate at normal incidence. The temperature of the crystal is monitored and controlled using a LakeShore Model 335 controller with two calibrated silicon diode sensors that have an estimated accuracy of 2 K and a relative uncertainty of 0.1 K. Transmission infrared spectra of the ices are obtained using a Fourier transform infrared (FTIR) spectrometer (Bruker Vertex 70v) with a resolution of 1 cm^{-1} and with 60 scans taken per spectra. Gas partial pressures were monitored during the diffusion experiments using a quadrupole mass spectrometer (Pfeiffer QMG 220M1). The desorbing molecules are monitored

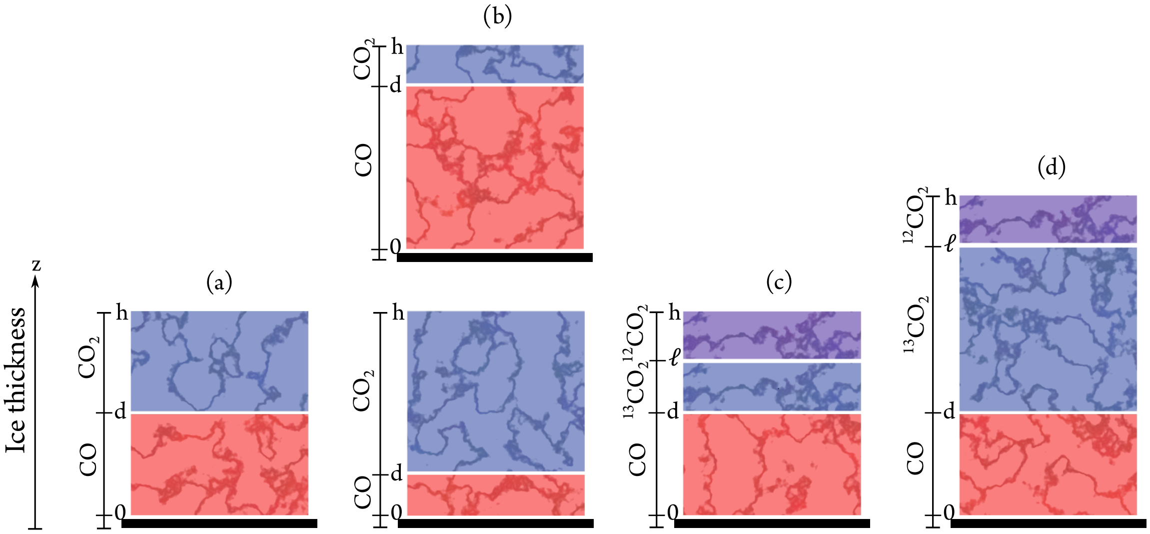

Figure 5.2.1: Schematic of ice configurations used during the diffusion experiments. The ices are displayed vertically along the z-axis, where *d* represents the height of the CO-CO_2 interface and *h* represents the height of the vacuum interface. *(a)* In the fiducial experiment 30ML of CO_2 is layered on top of 30 ML CO and heated to 20 K. This configuration is repeated for diffusion temperatures in 1 K increments between 18-23 K. We also use this configuration but scale the two layers to 20 ML CO: 20 ML CO_2 to explore the ice thickness dependence. *(b)* The ice thickness ratio was changed to 1:5 and 5:1 for the layered CO:CO_2 system. *(c)* The 30 ML CO_2 ice was split into 15 ML $^{13}CO_2$ and 15 ML $^{12}CO_2$, ℓ represents the boundary between the two isotopologues. *(d)* The thickness of the bulk isotopic layer was increased from 15 ML to 40 ML.

using a quadrupole mass spectrometer (Hiden IDP 300, model HAL 301 S/3) with a pinhole that is moved via a translational stage to ~0.5 inches away from the ice. The experiments were performed using CO_2 gas (99.99 atom % ^{12}C, Sigma), $^{13}CO_2$ (99 atom % ^{13}C, <3 atom % ^{18}O, Sigma) and ^{13}CO (99 atom % ^{13}C, <5 atom % ^{18}O, Sigma).

5.2.2 DIFFUSION EXPERIMENTAL PROCEDURES

The diffusion experiments consist of initially layered CO:CO_2 ices whose mixing is monitored using infrared spectroscopy. In each of these experiments ^{13}CO and CO_2 were deposited sequentially at 11 K at a rate of ~1 ML/minute to form the layered ice structures. The deposited

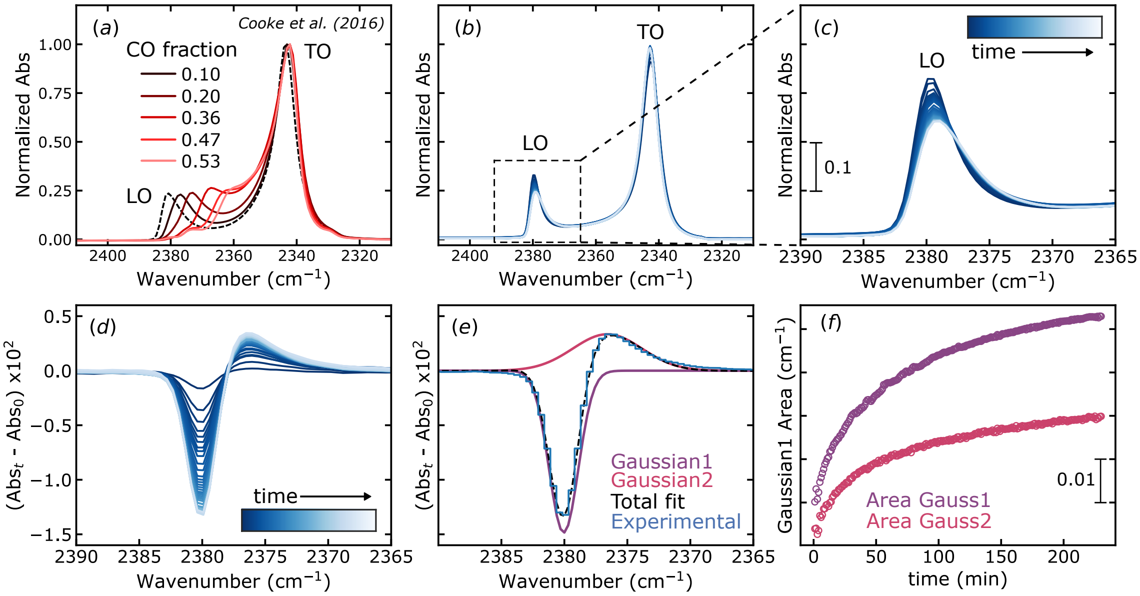

Figure 5.2.2: Strategy for fitting the changes in the CO_2 ν_3 LO mode to determine the kinetics of CO diffusion into CO_2 ices (*a*) Spectra of CO:CO_2 ice mixtures adapted from Cooke et al. [46] showing the redshift in the CO_2 LO phonon mode with increasing CO ice fraction, the dashed line shows pure CO_2 ice for reference. (*b*) Absorbance spectra of the CO_2 ν_3 mode during CO diffusion into 30 ML of CO_2 at 20 K, (*c*) shows a zoom in of the LO phonon mode for clarity. (*d*) Subtraction spectra of the CO_2 LO phonon mode during CO diffusion at 20 K. (*e*) An example fit to an experimental subtraction spectrum taken after CO has diffused into CO_2 for ∼200 minutes, the spectra are fit by optimizing the sum of the two gaussians. (*f*) The resulting areas of the two gaussians plotted against the diffusion time.

ice thicknesses were determined using IR absorption spectroscopy and Eq 5.1, which relates the column density to the ice absorbance:

$$N_i(cm^{-2}) = \frac{cos\theta \int \tau_i(\nu)\, d\nu}{A_i} \tag{5.1}$$

where N_i is the column density of the ice species i, θ is the angle of incidence between the IR field vector and the ice surface normal (here 45°), $\int \tau_i(\nu) d\nu$ is the integrated area of the chosen IR band (in optical depth) and A_i is the associated band strength adopted from Gerakines et al. [89] and Bouilloud et al. [28]. The column densities, N_i, were then converted to thicknesses in monolayers assuming 10^{-15} molecules/ML, or to nanometers using the mass densities of CO and CO_2 ice from Satorre et al. [193] and Roux et al. [186]. Following deposition, the layered ices were kept at 11 K for ∼10 minutes and were subsequently heated at 5 K minute^{-1} to the desired temperature and maintained there for 2–4 hours. Time zero was taken when the isothermal temperature was reached. Infrared scans were taken every minute to monitor the ice composition.

The different families of experiments are illustrated in Figure 5.2.1. The target and actual layer thicknesses, as well as the temperature at which mixing was monitored are listed in Table 1. The fiducial experiment consisted of ices with target thicknesses of 30 ML ^{13}CO followed by 30 ML of CO_2 and held at 20 K. We then carried out a series of experiments at different temperatures and with different ice thicknesses as well as experiments with isotopically labeled layers in order to extract the barrier for diffusion and elucidate the diffusion mechanism. We ran the temperature dependent experiments with the 30 ML:30 ML composition from T = 18–23 K. Above 23 K non-negligible CO desorption occurs and the diffusion rate is so rapid that the fits have large uncertainties. Below 18 K the diffusion rate is too slow to measure during our experimental timescale. In addition to the temperature dependent experiments, we also ran diffusion experiments for different CO:CO_2 thickness configurations at 20 K using the thicknesses shown in Figure 5.2.1.

5.2.3 TPD Experimental Procedures

Temperature programmed desorption experiments are used to obtain the desorption energy of ^{13}CO from CO_2 ice. Ices are grown using the same conditions described in section 5.2.2. In each experiment we first deposited ∼50 ML of CO_2 followed by ≤1 ML of CO. The CO_2 ice substrates were deposited at 11, 21, 23, 25, 40 and 50 K to obtain different CO_2 ice structures; the ice

Table 1. Initial ice thicknesses and diffusion temperatures used in the diffusion experiments and modeling. There are two experimental series aimed at elucidate temperature and ice thickness dependencies, as well as an isotopically labeled experimental series.

Experiment	Target Ice (ML)	T_{diff} (K)	CO (1-0) area (cm^{-1})	CO_2 ν_3 area (cm^{-1})	CO thickness[a] d (nm)	CO_2 thickness[a] $h-d$ (nm)
Temperatures	$CO:CO_2$					
1	30:30	18	0.27	1.39	16	14
2	30:30	19	0.27	1.60	16	16
3	30:30	20	0.27	1.38	15	14
4	30:30	21	0.26	1.45	15	14
5	30:30	22	0.28	1.42	16	14
6	30:30	23	0.27	1.47	15	15
Ice thicknesses	$CO:CO_2$					
3	30:30	20	0.27	1.38	15	14
7	10:50	20	0.09	2.30	5	23
8	50:10	20	0.45	0.50	26	5
9	20:20	20	0.13	0.78	8	8
Isotope layers	$CO:{}^{i}CO_2:{}^{j}CO_2$[b]					
10	30:15:15	20	0.28	0.77+0.70	16	8+7
11	30:15:15	20	0.28	0.71+0.77	16	7+8
12	30:40:15	20	0.27	1.89+0.79	16	19+8

[a] The uncertainty on the ice thickness in nanometers is estimated to be ∼15%

[b] i and j refer to carbon mass 13-Carbon or 12-Carbon.

Note. — We use the following band strengths and ice densities to calculate the CO and CO_2 thicknesses: $A_{^{12}CO_2}(\nu_3) = 1.1 \times 10^{-16}$, $A_{^{13}CO_2}(\nu_3) = 1.15 \times 10^{-16}$, $A_{^{13}CO}$(1-0)= 1.7×10^{-17} cm $molecule^{-1}$ from Gerakines et al. [89] and corrected for denisity in Bouilloud et al. [28], $\rho_{CO_2} = 1.1$ g/cm^3 [193], $\rho_{CO} = 0.8$ g/cm^3 [186]

deposited at the lowest temperature is expected to be the most porous. Following CO_2 deposition the ice was cooled down to 11 K before depositing ^{13}CO. The ices were heated at a constant rate of 1 K minute^{-1}. We subtract the mass background for ^{13}CO and normalize the integrated QMS signal to the amount of CO deposited using the infrared spectra taken prior to heating.

5.3 Diffusion Analysis and Results

In this section, we describe the results and analysis of the CO:CO_2 diffusion experiments. In section 5.3.1 we present the spectral analysis used to follow CO diffusion into the CO_2 based on changes in the ν_3 LO phonon mode. In section 5.3.2 we describe the outcome of all bi-layered diffusion experiments using the spectral analysis from section 5.3.1. In section 5.3.3 we describe the model framework used to quantify the diffusion rate in each experiment. In section 5.3.4 we apply the models to the experimental data and extract the CO-CO_2 diffusion barrier. Finally, in section 5.3.5 we present the results of experiments in which isotopically labelled CO_2 layers are employed to further constrain the diffusion mechanism.

5.3.1 Spectral Analysis

During the isothermal diffusion experiments we monitor changes in the CO_2 LO phonon mode. Figure 5.2.2(a) shows spectra of CO:CO_2 ice mixtures of various CO concentration, reproduced from Cooke et al. [46]; the CO_2 LO phonon mode is perturbed when CO_2 is mixed with CO and thus can be used as a tracer of CO diffusion in CO_2 ices.

Figure 5.2.2(b)-(c) shows an example of the CO_2 LO phonon mode during the diffusion experiment at 20 K. The LO phonon frequency at $t = 0$ is taken as reference for the pure CO_2 ice

Table 2. CO:CO$_2$ diffusion experiments grouped by experiment type, together with the final fitted LO Gaussian areas, mixing rate coefficients and Fickian diffusion coefficients.

Experiment	Target Ice (ML)	T_{diff} (K)	LO_{2381} $area_f$[a] (cm^{-1})	LO_{2375} $area_f$[a] (cm^{-1})	k_{mix}[b] (s^{-1})	$D_{Fickian}$[c] ($cm^2\ s^{-1}$)
Temp dep	CO:CO$_2$					
1	30:30	18	0.027	0.012	$5.9 \pm 2.0 \times 10^{-5}$	$9.0 \pm 0.6 \times 10^{-17}$
2	30:30	19	0.043	0.026	$2.0 \pm 0.6 \times 10^{-4}$	$2.3 \pm 1.2 \times 10^{-16}$
3	30:30	20	0.041	0.021	$3.1 \pm 1.0 \times 10^{-4}$	$2.5 \pm 1.4 \times 10^{-16}$
4	30:30	21	0.041	0.026	$1.2 \pm 0.4 \times 10^{-3}$	$8.3 \pm 0.5 \times 10^{-16}$
5	30:30	22	0.051	0.028	$3.2 \pm 1.6 \times 10^{-3}$	$2.4 \pm 2.0 \times 10^{-15}$
6	30:30	23	0.050	0.030	$6.7 \pm 3.4 \times 10^{-3}$	$3.2 \pm 2.8 \times 10^{-15}$
Ice thickness	CO:CO$_2$					
3	30:30	20	0.041	0.021	$3.1 \pm 1.0 \times 10^{-4}$	$2.5 \pm 1.3 \times 10^{-16}$
7	10:50	20	0.071	0.049	$2.3 \pm 1.4 \times 10^{-4}$	$2.8 \pm 5.8 \times 10^{-17}$
8	50:10	20	0.010	**	$3.7 \pm 1.1 \times 10^{-3}$	$1.3 \pm 6.8 \times 10^{-15}$
9	20:20	20	0.016	0.004	$3.8 \pm 1.2 \times 10^{-4}$	$1.1 \pm 2.3 \times 10^{-16}$
Isotopic layers	CO:^{i}CO$_2$:^{j}CO$_2$[d]		*i:j*	*i:j*		
10	30:15:15	20	0.012:0.027	0.009:0.011	$5.7 \pm 1.8 \times 10^{-4*}$	$5.8 \pm 0.4 \times 10^{-16*}$
11	30:15:15	20	0.012:0.028	0.007:0.016	$4.8 \pm 1.5 \times 10^{-4*}$	$4.7 \pm 2.9 \times 10^{-16*}$
12	30:40:15	20	0.058:0.025	0.040:0.008	$3.0 \pm 0.9 \times 10^{-4*}$	$5.1 \pm 3.0 \times 10^{-16*}$

[a] Area of Gaussian fit at the end of the diffusion experiment period

[b] Mixing rate calculated by fitting equation 5.5 to the experimental data.

[c] Fickian diffusion coefficient found by fitting 5.4 to the experimental data

[d] *i* and *j* refer to carbon mass 13-Carbon or 12-Carbon.

* Calculated for the total CO$_2$ ice thickness by summing together the two layers.

Note. — ** The integrated Gaussian area was too low to obtain a good fit.

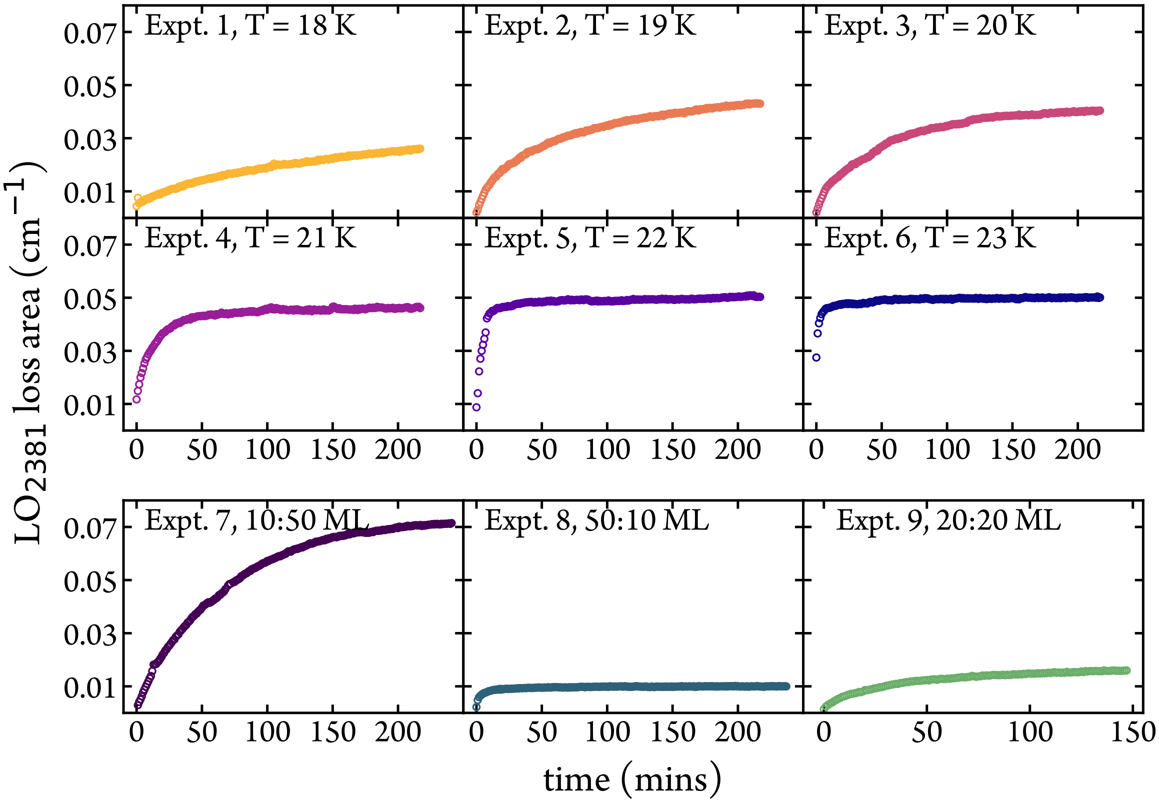

Figure 5.3.1: Experimental kinetic curves for the diffusion of CO into CO_2 as traced by the CO_2 ν_3 LO mode. Here, the area of the Gaussian corresponding to the loss of the pure CO_2 environment upon mixing with CO is plotted against time. The top two rows show the results of experiments conducted for 30 ML CO: 30 ML CO_2 ices at six temperatures between 18–23 K. The bottom row shows the results for diffusion experiments where the CO:CO_2 thickness ratio is 1:5, 5:1 and 1:1.

and is ~2381 cm^{-1} (4.2 μm). With time, we observe a decrease in the LO phonon intensity at 2381 cm^{-1} and an apparent broadening of the feature towards lower frequencies. The subtraction spectra (Figure 5.2.2(d)) reveal two distinct features: a loss centered at ~2381 cm^{-1} and a growth centered around 2375 cm^{-1}. Two Gaussians are fit to the subtraction spectra (Figure 5.2.2(e)) and their sum is optimized in Python using the *scipy.optimize.nnls* optimization package. The resulting negative Gaussian (Gaussian 1) is considered as a loss of the original pure CO_2 ice environment, while the positive Gaussian (Gaussian 2) arises from the new CO-CO_2 mixed environment. The new redshifted LO feature, while growing in intensity during diffusion experiment, does not shift in frequency, which can be contrasted to CO:CO_2 mixtures we deposited from gases in Cooke et al. [46], where the frequency changed with mixture concentration.

While both Gaussians can be used to model mixing of CO into the CO_2 layer, we use the negative Gaussian 1 to extract the diffusion coefficients; the integrated area of Gaussian 1 is larger than that of Gaussian 2, allowing us to better fit the fast mixing kinetics within the first 10 minutes of the diffusion experiments.

5.3.2 CO DIFFUSION EXPERIMENTAL RESULTS

Figure 5.3.1 and Table 2 show the results of the diffusion experiments. The top two rows of Figure 5.3.1 show the outcome of diffusion experiments with close to identical ice thicknesses but run at six different temperatures between 18 and 23 K. At 18 K mixing is not complete after 250 min, while at 23 K it is complete within the first $\sim$10 min. The final mixing fraction, as traced by the loss of the LO mode, is almost constant above 18 K i.e. the ice morphology is almost independent of ice temperature within the explored range; by contrast the loss rate depends strongly on temperature. This is the expected behavior for a system in which diffusion is driven by the random movement of the more volatile species, motivating our model choices below.

The bottom row of Figure 5.3.1 shows the experiments for different CO:CO_2 thicknesses; Experiment 7: 10 ML CO and 50 ML CO_2, Expt 8: 50 ML CO and 10 ML CO_2 and Expt 9: 20 ML CO and 20 ML CO_2. The final mixed fraction depends on the CO_2 ice thickness as expected, i.e. thicker CO_2 ices can host more CO molecules. We explore the dependence of the diffusion rate on ice thickness and CO:CO_2 ratio quantitatively in section 5.3.4.

5.3.3 Fickian diffusion modeling

We use a Fick's second law model to extract the diffusion coefficients and barrier for CO diffusion into CO_2 ice. Fick's law has been applied by Karssemeijer et al. [116], Mispelaer et al. [151] and Lauck et al. [129] to model CO diffusion in amorphous solid water (ASW) ices.This law should apply if the ice mixing is dominated by random walk diffusion of the more volatile CO into the CO_2 matrix resulting in a concentration gradient across the ice depth. We also fit the kinetic data with exponentials to give a rate coefficient and time associated with CO mixing into the CO_2 layer.

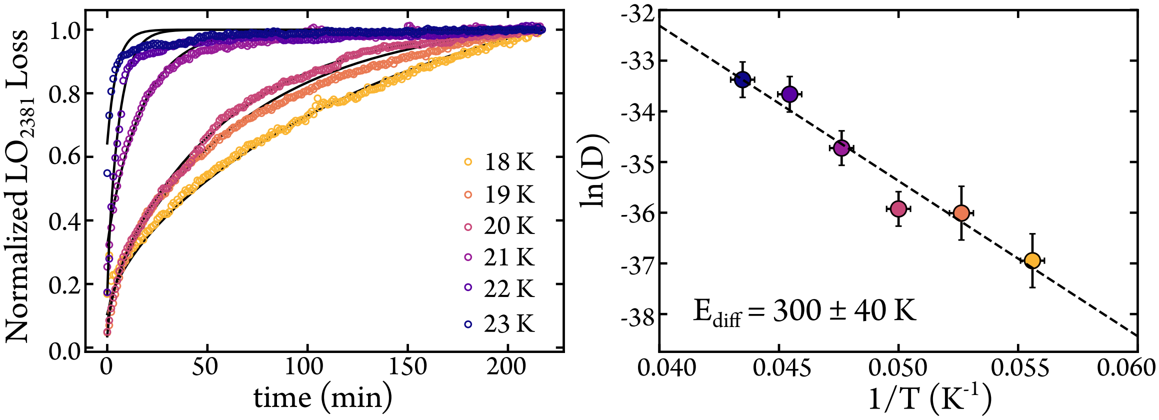

Figure 5.3.2: Temperature dependent kinetics of the CO diffusion into CO_2 ice fit using Fick's second law (left) along with the Arrhenius Law plot (right) for the temperature dependent diffusion coefficients

We adopt a Fickian diffusion model modified from Lauck et al. [129] and [18]. The general form of Fick's second law for a 1-D system is:

$$\frac{\partial c(z,t)}{\partial t} = D(T)\frac{\partial^2 c(z,t)}{\partial z^2} \tag{5.2}$$

where $c(z,t)$ is the concentration of the diffusant CO as a function of time, t, and position, z, and $D(T)$ is the temperature dependent diffusion coefficient. In the layered CO:CO_2 system we define $z = 0$ as the substrate height, $z = d$ as the interface height between CO and CO_2 layers, and $z = h$ as the vacuum interface. To calculate the height of the CO/CO_2 and vacuum interfaces, we use densities of 1.1 g/cm^3 [193] and 0.8 g/cm^3 [186] for CO_2 and CO, respectively. For a system where CO desorption is negligible we impose boundary conditions such that the flux of CO at the CsI subtrate and at the vacuum interface is zero, i.e. $\frac{\partial c(z,t)}{\partial t} = 0$ at $z = 0$ and $z = h$. At $t = 0$, we assume the concentration of CO is c_0 in the CO layer and zero everywhere else. Applying these boundary conditions gives a general solution that may be integrated to find the amount of CO in the CO_2 layer. Dividing this through by the total amount of CO gives a mixed fraction, N_{mix}:

$$N_{mix}(t) = \frac{1}{dc_0}\int_d^h c(z,t)dz = \frac{h-d}{h} - \sum_{n=1}^{\infty} \frac{2h}{n^2\pi^2 d} sin^2\left(\frac{n\pi d}{h}\right) exp\left(-\frac{n^2\pi^2}{h^2}Dt\right) \tag{5.3}$$

This is adjusted to account for mixing during the fast temperature ramp by using a time offset, t_0, and for uncertainties in the measured ice thickness using a nuisance parameter, N_0, yielding

$$N_{mix}(t) = N_0\frac{h-d}{h} - \sum_{n=1}^{\infty} \frac{2N_0 h}{n^2\pi^2 d} sin^2\left(\frac{n\pi d}{h}\right) \times exp\left(-\frac{n^2\pi^2}{h^2}D(t+t_0)\right) \tag{5.4}$$

Here D, N_0 and t_0 are free parameters that are fit to the experimental mixing fraction of CO over time. We use the python non-linear least squares routine *scipy.optimize.curve_fit* to fit equation 5.4.

We also fit the mixing of CO into CO_2 using exponentials. Fitting exponentials to the data allows us to directly extract a time constant associated with the diffusion process. A similar method has been used to fit the kinetics of molecules diffusing into ASW ice [151]. The exponential equation describing the time dependent mixed fraction, N_{mix}, is:

$$N_{mix}(t) = N_0 \, e^{-(k_{mix} t)^n} \tag{5.5}$$

where k_{mix} is the mixing rate coefficient in s^{-1} and n is the kinetic order. The diffusion coefficient, D, can be roughly approximated from the mixing rate coefficient using Einstein's relationship:

$$D \simeq \frac{k_{Av}\,(h-d)^2}{2} \tag{5.6}$$

Where $h - d$ is the thickness of the CO_2 ice in which the CO diffuses. This equation generally gives us the same order of magnitude diffusion coefficients as obtained using the Fickian model.

5.3.4 DIFFUSION KINETICS AND BARRIERS

Consistent with the qualitative analysis above the Fickian diffusion coefficients increase with temperature from $\sim$1x10^{-16} cm^2 s^{-1} at 18 K to $\sim$3x10^{-15} cm^2 s^{-1} at 23 K. The mixing rates obtained from exponentials fits to the kinetic data likewise increase with temperature and are shown in Table 2. There are two major sources of uncertainty on the diffusion coefficients that are propagated into the uncertainty on the diffusion barrier. At the higher temperatures ($T>20$ K), the largest source of uncertainty is the choice of the $t = 0$ point, which can change the diffusion coefficient by up to 50%. The largest source of uncertainty for the experiments where $T \leq 20$ K arises from the thickness determination and is a combination of uncertainties in the CO and CO_2 band strengths and their densities.

A weighted linear regression to the Fick's Law Arrhenius plot (Figure 5.3.2) yields a diffusion energy barrier of 300 ± 40 K. We also fit an Arrhenius Law to the mixing rate coefficients (not shown here) and find a barrier of 380 ± 30 K, indicating that the derived barrier is robust to the choice of model.

Comparing the ices with different thickness configurations we find that the mixing timescale decreases with decreasing CO_2 ice thickness. Based on the exponential fit, the characteristic mixing time constant is 4.5 minutes for the thin 10 ML CO_2 ice and 72 minutes for mixing into the thick 50 ML CO_2 ice. Likewise, the Fickian diffusion coefficients increase from 3×10^{-17} cm^2 s^{-1} in the 10 ML CO: 50 ML CO_2 ice to 1×10^{-15} cm^2 s^{-1} in the 50 ML CO: 10 ML CO_2 ice, i.e. it is larger for larger CO:CO_2 ratios. The diffusion rates extracted for experiments with the same CO:CO_2 thickness ratio but different total ice thicknesses (30 ML:30 ML and 20 ML:20 ML) are the same within experimental error, indicating that the CO:CO_2 thickness ratio together with temperature control the diffusion rate, and that total ice thickness is not an important factor.

5.3.5 Isotopic Studies

The isotopically labeled layered ice experiments provide further insight into the mechanism of CO:CO_2 diffusion. Experiments were conducted with layered isotopic CO_2 ices as shown in Figure 5.2.1 and Table 1. We test two different isotopic thickness configurations in which we layered 30 ML of CO with (1) 40 ML $^{13}CO_2$ then 15 ML $^{12}CO_2$ (Fig 5.3.3(a)) and (2) 15 ML $^{13}CO_2$ then 15 ML $^{12}CO_2$ (Fig 5.3.3(b)).

Figure 5.3.3 shows the kinetic curves for CO mixing into the two CO_2 layers. In Fig 5.3.3(a) we see that the middle 40 ML layer has a larger final LO Gaussian loss area, corresponding to a larger number of mixed CO molecules, than the top 15 ML layer. By contrast, in Fig 5.3.3(b) the top 15 ML is able to host more CO than the bottom 15 ML despite their equal thicknesses. We

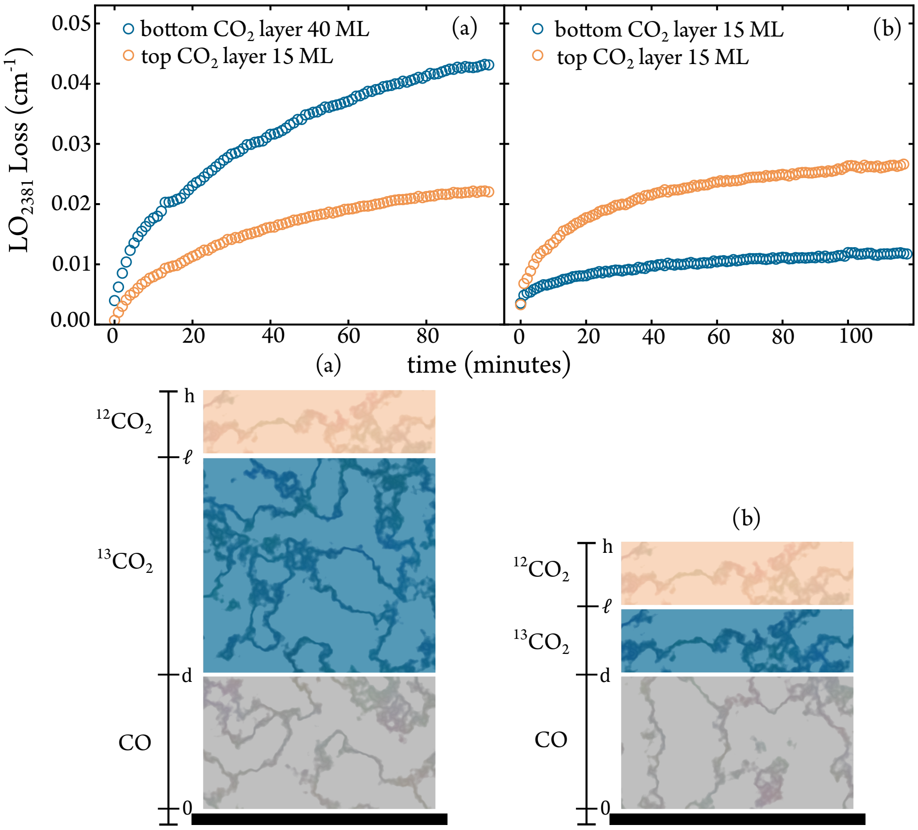

Figure 5.3.3: Experimental CO diffusion into isotopic layers of CO_2. Panel *(a)* shows diffusion of CO into a 40 ML $^{13}CO_2$: 15 ML $^{12}CO_2$ ice. Panel *(b)* shows CO diffusion into two 15 ML thick $^{13}CO_2$: $^{12}CO_2$ isotopic layers.

also switched the isotopic order and layered 15 ML $^{12}CO_2$ then $^{13}CO_2$ and found that the top 15ML layer always hosts more CO regardless of the order of the two isotopologues. In each of these three experiments, we found that the final mixed fraction in the top 15 ML layer was the same. We discuss the physical interpretation of these results further in section 5.5.

We calculate the diffusion coefficients for CO through the total ice thickness by summing the LO loss feature in both layers, reported in Table 2. We do this purely to check whether the diffusion coefficients calculated from the summing the two 15 ML layers are the same as the 30 ML experiment at 20 K and we find that two are indeed the same within experimental uncertainties.

5.4 TPD Analysis and Results

5.4.1 TPD Analysis

The TPD traces for CO desorbing from CO_2 ices are shown in the left panel of Figure 5.4.1. The spectra display one or two peaks between 25–50 K, depending on the ice surface area and corresponding CO coverage. CO desorption from CO_2 ices deposited at 40 and 50 K display two TPD peaks in this temperature regime. The first peak corresponds to multilayer CO desorption and occurs around 28 K, consistent with previous measurements in the literature [44, 75, 154, 160]. The higher temperature peak is associated with submonolayer desorption of CO from the CO_2 ice surface. This peak is broader than in the multilayer regime, indicating a larger range of binding sites and associated energies, even when the CO_2 ice is quite compact.

CO_2 ices deposited at temperatures $\leq$25 K have a single desorption peak associated with sub-monolyer CO desorption from the surface of the CO_2 ices. An additional desorption peak is seen near the CO_2 desorption temperature (not shown here), probably due to CO diffusion into the CO_2 pores and subsequent entrapment due to pore collapse. Similar entrapment has been seen for other volatile species within porous ASW ices [42, 76, 141]. No multilayer peak is observed for these ices, which is consistent with the expectation that ices deposited at lower temperatures are more porous and therefore present a larger surface for adsorbing molecules.

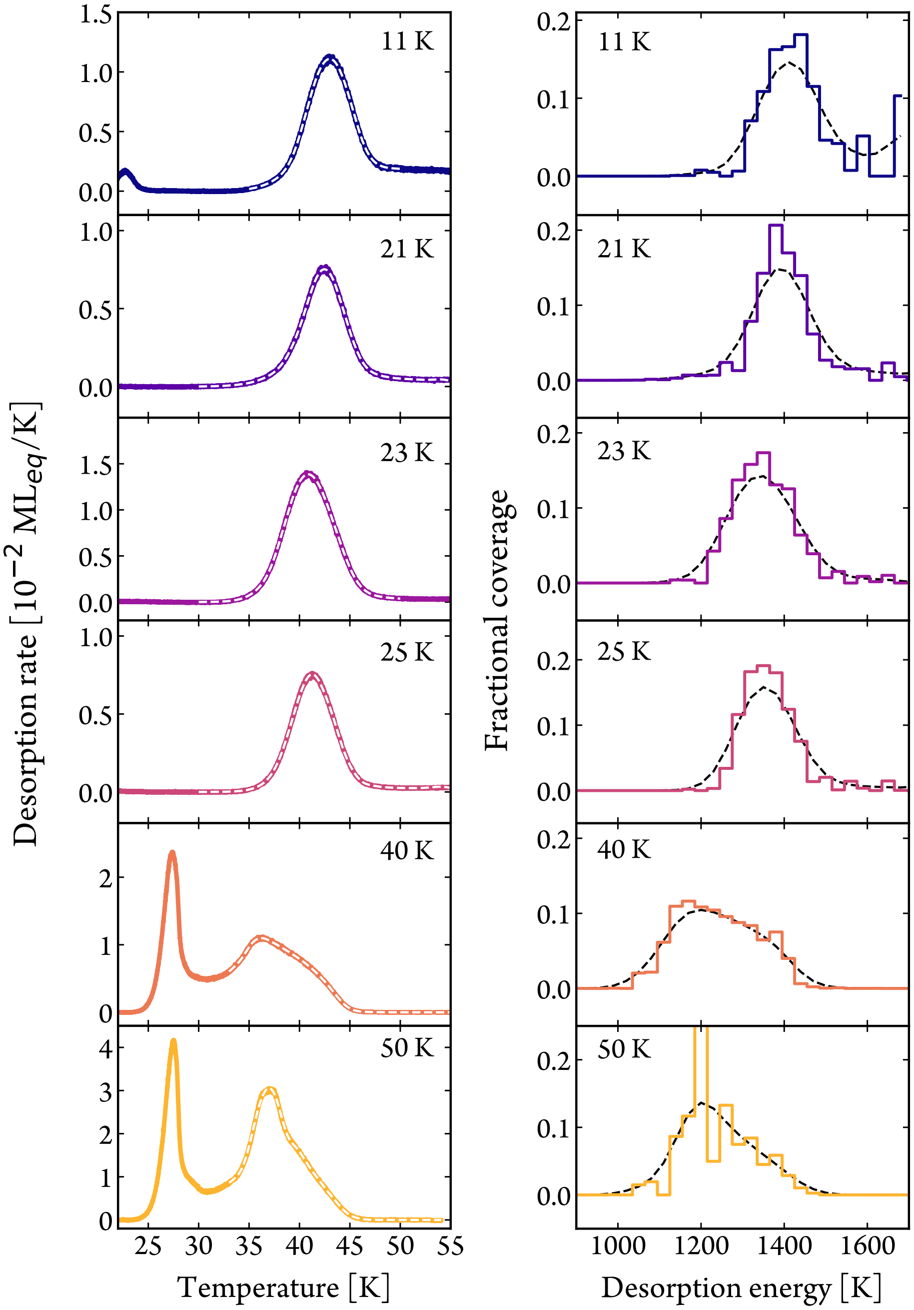

Figure 5.4.1: ^{13}CO temperature programmed desorption curves (*left*) and related desorption energy distributions (*right*) from CO_2 ices at various deposition temperatures listed in table 3. The TPD spectrum of CO desorption from CO_2 ice grown at 11 K also displays a small peak below 25 K that we attribute to CO co-desorption with hydrogen that is deposited from the chamber background.

Table 3. CO column densities, mean desorption energies and full-width half maxima for submonolayer CO desorption from CO_2 ices at different deposition temperatures.

CO_2 Temp (K)	CO column density (10^{15} molecules/cm^2)	E_{des} (K)	FWHM (K)
11	1.0	1407	71
21	0.7	1385	86
23	0.8	1347	84
25	0.5	1361	73
40	0.8	1240	105
50	0.8	1239	94

5.4.2 DESORPTION BARRIERS

Figure 5.4.1 shows the TPD curves for CO desorption from CO_2 ices deposited at 11, 21, 23, 25, 40 and 50 K. The TPD curves are fit using the Polanyi-Wigner equation:

$$-\frac{d\theta}{dT} = \frac{\nu}{\beta}\,\theta^n\,e^{-E_{des}/T} \tag{5.7}$$

where θ is the CO ice coverage, T is the temperature in K, ν is a pre-exponential frequency factor in s^{-1}, β is the heating ramp rate in K s^{-1}, n is the desorption order and E_{des} is the desorption energy in K. We see that the peak desorption temperature increases as the CO_2 deposition temperature is decreased. The trailing edges of the sub-monolayer CO peaks also extends to higher temperature for more porous CO_2 ices deposited at lower temperatures.

To derive the desorption energy distribution for CO on CO_2 we fit the TPD traces with a linear combination of first order kinetics using the methods of Doronin et al. [62] and described in detail in Fayolle et al. [75]. We use an energy step interval of 30 K to fit desorption kinetics between 900 and 1800 K. The resulting desorption energy distributions are shown in the right

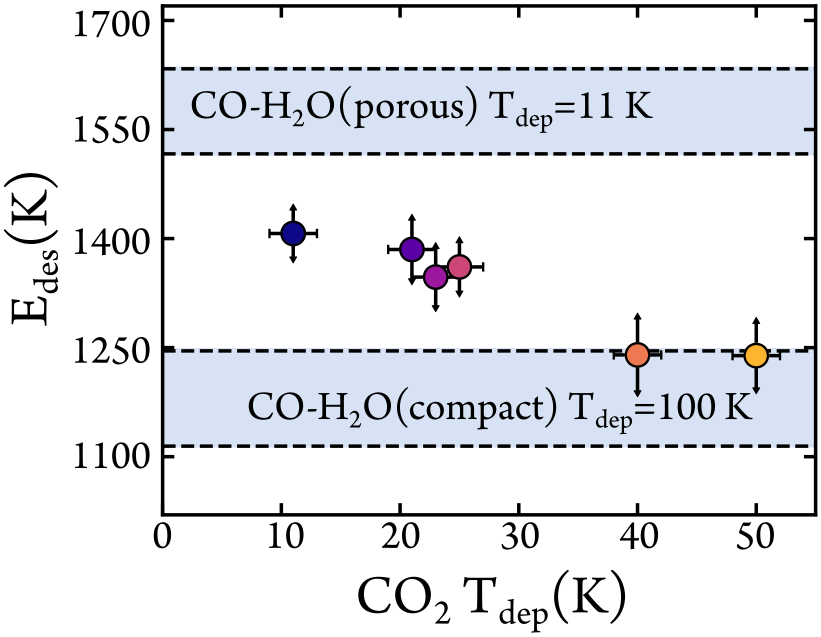

Figure 5.4.2: Desorption energies of ^{13}CO from CO_2 ice for various CO_2 deposition temperatures. The blue panels show the average desorption energy with FWHM distributions for porous H_2O ice deposited at 11 K and for compact H_2O ice deposited at 100 K reported in Fayolle et al. [75]

panel of Figure 5.4.1.

The mean desorption energies and desorption energy distributions, defined by the peak FWHM, for the various CO_2 deposition temperatures are shown in Figure 5.4.2 and in Table 3. The desorption energies for CO from CO_2 ices increase with decreasing deposition temperature and range from 1239 K to 1407 K for CO_2 ices deposited at 50 K and 11 K respectively. We show the desorption energies of CO from H_2O ice deposited at 11 K (porous) and at 100 K (compact) from Fayolle et al. [75] for comparison. The increase in CO-CO_2 desorption energy with decreasing CO_2 deposition temperature is likely due to an increase in porosity and therefore number of strongly bound sites. In the submonolayer regime, mobile molecules tend to fill the deeper adsorption sites, resulting in a shift in the mean E_{des} to higher energies (e.g. Fillion et al. [77]).

In the experiments where CO_2 is deposited at temperatures between 11–25 K, CO is slowly out-gassing between the CO and CO_2 desorption peaks, probably due to a combination of slow CO diffusion and CO_2 ice rearrangement during the TPD warm-up. CO out-gassing is the largest for the experiment where CO_2 ice was deposited at 11 K, consistent with expectations that this ice has the highest CO_2 porosity and therefore highest CO trapping efficiency. To avoid including the slow out-gassing effect into our calculation of the CO-CO_2 surface desorption energy, we fit a baseline to the TPD spectra before and after CO surface desorption, where the latter includes the spectral region where CO is slowly out-gassing. If the contribution from CO outgassing is instead included in the fit, the average desorption energies are systematically higher, but this increase is only significant for the 11 K CO_2 ice, where ignoring the baseline correction results in a $\sim$100 K increase in the desorption energy estimate compared to our reported value.

5.5 DISCUSSION

5.5.1 DIFFUSION MECHANISMS

There are three main diffusion mechanisms proposed in the literature that are relevant for low temperature interstellar ices and their laboratory analogs: swapping of lattice molecules [81, 88, 162], movement into empty vacancy sites in the lattice (e.g. Chang & Herbst [32], Lamberts et al. [127, 128] and surface hopping along adsorption sites in pores [87]. The former two are *bulk* diffusion processes, which are expected to have large barriers compared to pore surface hopping.

Our experiments provide three different lines of evidence that, in the case of CO diffusion into CO_2, the main diffusion mechanism is that of surface diffusion in pores and on the ice surface: the magnitude of the extracted diffusion barrier, the evolution of the LO mode during diffusion,

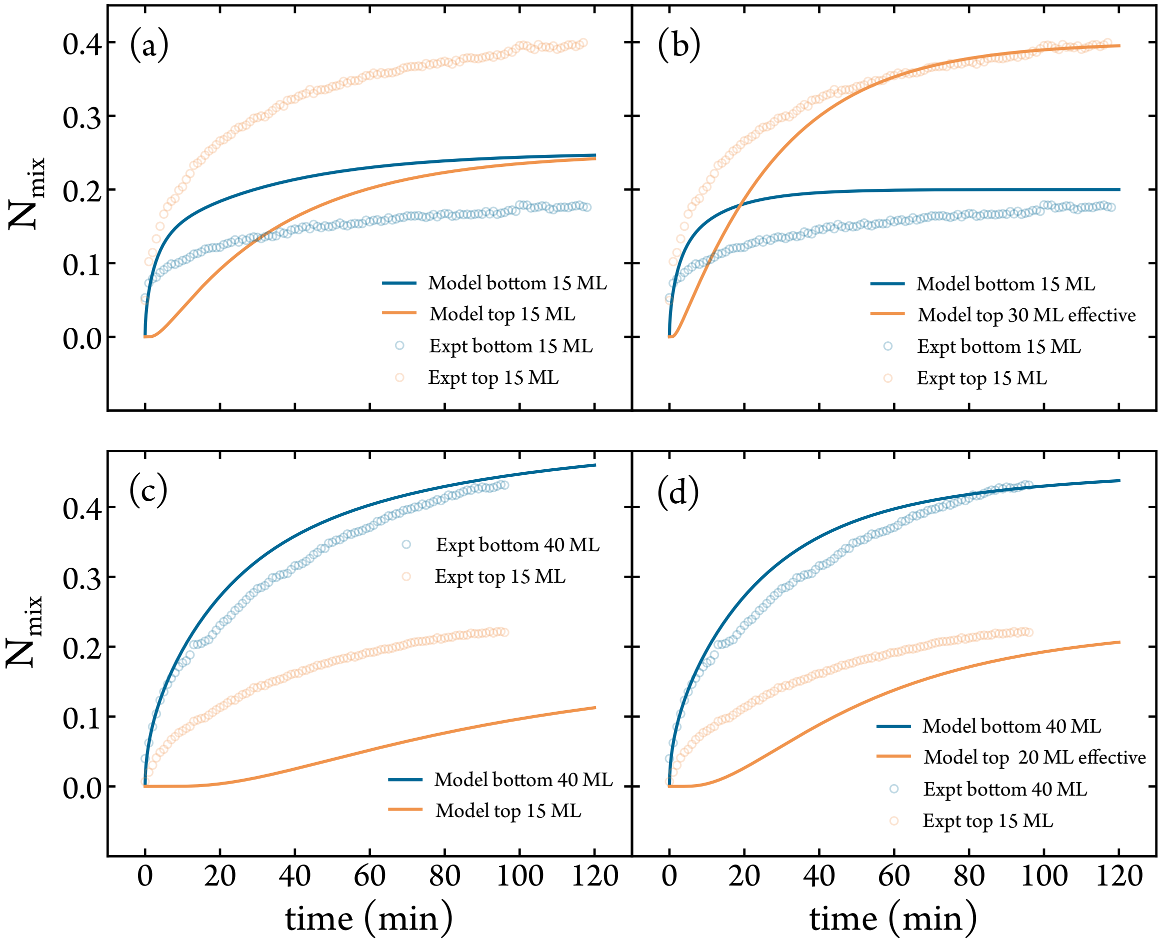

Figure 5.5.1: Fick's Law model for CO diffusion into isotopic layers of CO_2. Panels a) and c) model are modeled using the CO_2 thicknesses used in the experiment and a relevant diffusion coefficient from the measurements at 20 K. Panels b) and d) show adjustments to the Fickian model by scaling the heights to an "effective" thickness by assuming that the top layer has an additional surface area that is not present in the lower layer. The diffusion coefficient is increased to assume that once the CO reaches a pores in the lower CO_2 it can move more rapidly along the pore surface to the top layer. The faint open circles display the experimental kinetic traces for comparison.

and the observed diffusion pattern through isotopically labeled ice layers.

First, the low diffusion barrier and the low diffusion-desorption energy barrier ratio of 0.21-0.24 is consistent with surface diffusion, but not with models of bulk diffusion in which ratios ranging from 0.5 for diffusion by swapping [88] up to 1 for movement into interstitial sites

[32] have been employed. Similar low diffusion barriers have been measured for the diffusion of volatile species into porous water ices [129, 151].

Secondly, pore diffusion is the best explanation for how the CO_2 LO phonon mode evolves during the isothermal diffusion experiments. Our previous experiments reported in Cooke et al. [46] have shown that bulk mixing of CO into CO_2 ices redshifts the CO_2 LO mode linearly with the concentration of CO. If diffusion occurred through swapping there should be a smooth change in the CO_2 ice lattice with time which should increasingly redshift the LO mode as more CO diffuses into the CO_2. This is not observed; rather, we observe the growth of a new feature at a single redshift. The diffusion mechanism then, does not change the bulk lattice structure during CO diffusion, and this is only consistent with either surface hopping or movement into interstitial sites.

The third line of evidence comes from the behavior of the isotopically labeled CO_2 layered experiments in section 5.3.5. If diffusion occurs by the random walk into the CO_2 layer with a homogeneous distribution of binding sites, we would expect diffusion into the top layer should be delayed with respect to the bottom layer, and the final mixing fractions should be the same for two layers of the same thickness. In Figure 5.5.1 we show a toy model to demonstrate this point. On the left-hand-side of Figure 5.5.1 (panels (a) and (c)), we input our experimentally measured ice thicknesses into Fick's law to model the mixing of CO into the CO_2 isotopic layers and compare with the actual experiments. Contrary to model predictions, in our experiment the top isotopic layer hosts more CO molecules per ML of CO_2 compared the to the bottom CO_2 layer; the Fick's law model (solid lines) expects equal final mixing of CO into CO_2 layers of the same thickness. The second discrepancy is the predicted time delay for CO mixing into the top layer, which is not seen in our experimental data.

One possible explanation for the discrepancy in the final mixing fractions is that the top layer has a larger number of surface sites, i.e. the binding sites for CO are not distributed homogeneously across the CO_2 ice height. We incorporate this into the toy model by assigning the top layer an "effective thickness" to best match the experimental mixing fractions by eye. In the case of 15 ML:15 ML ice, we need to roughly double the thickness of the top layer to reproduce the relative mixing fractions seen in the experimental curves. In the 40 ML: 15 ML case we increase the top layer by around 33%. In the pore-diffusion scenario, this effect can be explained physically by a larger number of surface sites per CO_2 ML in the top isotopic layer due to additional surface binding sites at the vacuum interface. Changing the effective thicknesses of the two layers does not resolve the above noted mismatch between predicted and experimental mixing delay times. The immediate appearance of mixing in the top ice layer (within the measurement time scale) is best explained by a rapid pore diffusion, which is faster than expected using our solution to Fick's law that. One possible explanation for the rapid pore-diffusion is that initially absorbed CO molecules at the CO-CO_2 boundary could facilitate faster diffusion of subsequent CO molecules via decreased van der Waals interactions. Because the CO-CO adsorption energy is lower than that of CO-CO_2 the diffusion kinetics would reflect the CO-CO self-diffusion barrier. This possibility has been suggested previously by Lauck et al. [129] for the case of CO diffusing through porous water ices.

In summary, diffusion of CO through CO_2 ice most likely occurs through internal pores; this theory is supported by the low diffusion-desorption energy barrier ratio, the evolution of the CO_2 ν_3 LO mode during CO diffusion, and the surface accumulation of CO in the isotopically labeled ice experiments.

5.5.2 CO_2 LO PHONONS FOR TRACING DIFFUSION

We have presented a new method for studying diffusion processes in CO_2 bearing ices based on the sensitivity of the CO_2 LO phonon mode to the ice environment. Diffusion kinetics in ices have most commonly been measured via decreases in IR absorption of the diffusing molecule after desorption. Typically, a layered or mixed ice is heated temperatures above the desorption temperature of the volatile species. In these experiments the volatile species diffuses through the ice and subsequently desorbs; the diffusion is then traced by the decreasing infrared absorption. These experiments are usually not able to distinguish well between the mechanisms of diffusion as the molecule can diffuse from both weakly and strongly bound sites. In our method we monitor diffusion by observing changes in the CO_2 lattice IR modes. This method resembles that used by Lauck et al. [129], where the IR feature of the diffusing molecule, CO, was monitored, but presents a number of advantages.

First, this technique could be extended to study ice systems in which the diffusing molecule itself is IR inactive, e.g. O_2, N_2, but produces a still produces a shift in the CO_2 LO mode upon mixing with CO_2.

Second, LO phonon modes are very sensitive to the exact mixing morphology of the ice, which enabled us to distinguish between mixing through pore diffusion and mixing through bulk diffusion.

Using LO phonons to trace ice mixing and diffusion also present some unique challenges. The LO phonon frequency shifts are the result of changes in the ice lattice to intermolecular forces between CO_2 and the diffusing CO molecules and there are potentially other processes that can also change the lattice structure. In particular, at temperatures similar to those employed in our experiments, the CO_2 ice may undergo pore collapse or reorganization, which could change the LO phonon frequency. To check the potential impact of CO_2 morphology changes, we also ran an isothermal experiment in which we deposited pure CO_2 ice. In this experiment we did not see a redshift of the LO mode indicating that CO diffusion into CO_2 is indeed responsible for the observed redshift during the diffusion experiments. At longer time scales, we did, however, see a slow blueshift and narrowing of the LO mode develop attributed to CO_2 crystallization. Fortunately, the CO_2 crystallization is slower than the CO diffusion process in our temperature regime and it appears that CO diffusion into CO_2 further slows the CO_2 crystallization rate.

5.5.3 DIFFUSION AND DESORPTION BARRIERS AND THEIR ASTROPHYSICAL IMPLICATIONS

The CO:CO_2 diffusion barriers extracted in this work, combined with the complementary measurements of the CO-CO_2 desorption barriers places CO:CO_2 ice diffusion into a growing family of systems with low, <0.3, ice diffusion-desorption barrier ratios. This suggests that diffusion may be underestimated in current gas-grain astrochemical models which typically adopt diffusion-desorption energy barrier ratios of 0.3 or higher [31, 85, 117, 188]. However, it is important to note that these low diffusion barriers are only valid for ices with pores, and may be sensitive to porosity differences between laboratory and interstellar ices [87].

It is further important to note that the diffusion-desorption barrier ratio for the CO:CO_2 system is larger by a factor of two compared to the diffusion-desorption barrier ratio for the CO:H_2O system that can be derived from experiments of Lauck et al. [129] and Fayolle et al. [75]. This strongly suggests that there is no universal ratio that can be applied in models, but rather that experiments and molecular dynamics models are needed for several other major ice constituents and for mixed ices to evaluate the range of possible ratios.

Through our measurements to determine the diffusion-desorption barrier ratio for the CO:CO_2 ice system, we systematically measured CO-CO_2 desorption barriers for the first time. We found that the CO-CO_2 E_{des} barriers are substantially higher than the previous estimates of Cleeves et al. [41], who report a CO-CO_2 desorption energy of 1110 K based on the peak desorption temperature of CO from CO_2. Considering only the individual pairwise interactions between CO and the ice substrate, we would expect that the CO desorption energy from water ice should be higher than that from CO_2. Instead, the ice morphology appears to be more important in controlling the CO desorption from H_2O and CO_2 ices. This implies that the CO desorption temperature in, for example, protoplanetary disks, may be high even when CO is not in direct contact with water ice. A recent study places the CO snowline in the iconic protoplanetary disk TW Hya at 22 AU [237] and explains its location as a result of CO binding directly to water ice. Our results show that the same desorption temperature could result from binding to CO_2 ice, which might be a likelier scenario when considering the freeze-out temperatures and chemistry of H_2O, CO_2 and CO.

5.6 Conclusions

In this work we report the diffusion of CO into CO_2 from initially layered ices at low temperatures. We make the following conclusions:

1. We show that the CO_2 ν_3 LO phonon mode can be used to trace CO diffusion. This system could be used to study mixing phenomena between other astrophysically relevant ice constituents and CO_2.
2. The diffusion coefficients depend on temperature as well as the CO:CO_2 ice thickness ratio.
3. The temperature-dependent rates CO diffusion through CO_2 ice are well fit by an Arrhenius Law, which allows us to derive a diffusion barrier of 300 ± 40 K.
4. The CO from CO_2 desorption energies range from 1239-1407 K depending on the CO_2 ice deposition temperature. Some of the CO-CO_2 desorption barriers are similar to those from water ices, demonstrating that CO binds equally well to compact CO_2 as it does to compact water ice.
5. Combining these sets of experiments, we derive a diffusion-desorption barrier ratio for CO:CO_2 ices of 0.21–0.24. This ratio is low compared to what has been used in astrochemical models, suggesting that diffusion driven processes may be more efficient than what is currently assumed.

6. The low diffusion barrier, combined with constraints on the diffusion kinetics supports a scenario where CO diffusion into CO_2 occurs along internal pores and across the CO_2 ice surface rather than through the bulk ice. The CO mobility and mixing in CO_2 ices depends on the number of surface binding sites resulting in a accumulation of CO at the CO_2 ice surface.

We gratefully acknowledge productive discussions with Rob Garrod, Eric Herbst, Aspen Clements, Matthew Reish and Shiliang Ma, as well as helpful comments from an anonymous reviewer. I.R.C. acknowledges support from the Sidney M. Hecht Graduate Fellowship. K.I.Ö. acknowledges funding from the Simons Collaboration on the Origins of Life (SCOL) and the David and Lucile Packard Foundation.

6

New Measurements of Photodestruction Kinetics in Astrophysical Ices

In Progress: Ilsa R. Cooke, Karin I. Öberg, Rafael Martín-Doménech & Mahesh Rajappan

In cold regions of interstellar space, dust grains are enveloped by icy mantles composed of water and other volatile species. These ice mantles are exposed to UV-radiation during star-formation that can dissociate molecules in the ice and form reactive radicals. If the radicals are sufficiently mobile, they can react to form more complex molecules that could potentially be delivered to nascent planetary systems. Photodestruction of several astrophysically relevant molecules has been measured systematically for optically thick ices, as well as in some case-studies of optically thin ices. Large discrepancies remain in the reported photodestruction cross sections that may be a result of optical depth effects as well as uncertainties in the spectral emission and photon flux of the UV sources used. Here we present a survey of ice photodestruction kinetics in a range of astrophysically relevant ices and ice mixtures in the optically thin regime. We report measurements of photodestruction cross sections for pure ices

and binary ice mixtures of CO_2, CH_4, H_2O, NH_3 and CH_3OH. We find that the quantum efficiencies for photodestruction are lower in the ice than the gas-phase; this can be explained by cage effects that lower the net loss of the parent ice. We show that the photodestruction cross sections increase with temperature (except for CO_2 ices) and when the parent molecule is isolated in rare-gas matrices, as would be expected if cage effects modulate the ice destruction. We find that in most cases, the effective photodestruction cross sections in binary ice mixtures are larger than in the pure ice due to reactions between the photo-products of the two ice components. In some cases the ice photodestruction cross sections are decreased in the binary ice mixtures indicating either a reaction route that reforms the parent ice, or decreased mobility of photo-fragments in the binary ice mixture compared to the pure ice.

6.1 INTRODUCTION

Icy grain mantles are commonly observed in star and planet forming regions, and ice chemistry is proposed as the main source of complex organic molecules (COMs) that have been observed in the interstellar medium [83, 84]. The strong UV-fields in interstellar environments were initially considered an argument against the presence of large molecules including COMs; however, a wide variety of organic molecules with as many as 13-atoms (as well as fullerenes) have been observed in a range of astrophysical environments (e.g. Belloche et al. [13], Cazaux et al. [29], Cuadrado et al. [52], McGuire et al. [145], Thiel et al. [211], Walsh et al. [223]). Regions of the ISM that are shielded from the intense external UV-field can be particularly chemically rich due to photochemistry activated by the lower UV-fields in the internal cloud. In the interior of dense clouds, molecules are shielded from the external UV-radiation but are subject to a lower flux ($\sim 10^4$ photons cm^{-2} s^{-1}) secondary radiation due to the interaction between cosmic rays and hydrogen, which peaks at Lyman-alpha (10.2 eV, 121.5 nm) [98]. The lower UV-fields provide sufficient energy to produce reactive species, but are not so intense as to totally destroy the newly formed COMs.

The inventory of ice species detected in dense clouds and toward protostars consists of CO, H_2O, CO_2, CH_4, NH_3 and CH_3OH. Current models and observations suggest that the ices form sequentially resulting in a bi-layered structure of water-rich ("polar") and CO-rich ("apolar") environments, respectively [17, 119, 179, 180]. One proposed route to more complex species is the energetic destruction of simple ice species followed by diffusion and recombination of the photoproduced radical species. Once formed, the radicals can react or recombine efficiently, typically without reaction barriers. In order to form more complex organic molecules rather than recombining to reform the parent ice, the photo-fragments need to meet and react with other species in the mantle. This most likely requires diffusion of the radical fragments within the ice and therefore the dust temperatures need to be hot enough (typically >20 K) that the radicals are mobile. This method has been successfully implemented to model the formation of complex molecules in in-falling envelopes followed by ice evaporation (warm-up) using hot core conditions [83, 84, 88].

Recent measurements of ice photoirradiation show that the ice photodestruction cross sections are typically lower than their gas-phase counterparts [48, 90, 163, 164]. More informative are the relative quantum efficiencies for photodestruction in solids vs. the gas, which have become accessible due to recent measurements of wavelength dependent VUV-absorption spectra [49, 50, 143]. Lower photodestruction efficiencies in ices compared to the gas-phase may explained by the *cage effect*: once a photon is absorbed by a solid state molecule the dissociative intermediate, AB*, must overcome an exit barrier in order to form the dissociated radical species, A + B [95, 126, 196]. The size of the barrier is dependent on van der Waals forces between the absorbing species and the local ice matrix. This suggests that the solid phase photodestruction rates should depend on both temperature dependent the nature of the ice binding environment.

Early laboratory studies aiming to mimic irradiation of interstellar ices were mainly focused on the nature of complex molecules and resultant refractory residues starting with simple molecules observed in the ISM ices [3, 19, 55, 198]. Only a few studies have been conducted that aim at reporting kinetic constants (i.e. cross sections) in order to extrapolate from the laboratory to ISM environments. The cross sections derived in each of these studies are reported in Table 6.1.1. Gerakines et al. [90] conducted a systematic study of UV photoprocessing of pure ices, reporting the photoproducts formed in each case as well as formation and destruction cross sections. The ices in this study were thin enough to allow complete penetration of the VUV-photons; however, the photon flux was estimated rather than measured so the absolute photodestruction cross sections are uncertain. Cottin et al. [48] extended the measurements of Gerakines et al. [90], providing photodestruction cross sections for five interstellar ice molecules and HNCO as pure ices, as well as in H_2O and N_2 matrices. They fit the ice photodestruction kinetics assuming first-order decay rates although recognizing that their ices were optically thick to at least some of the VUV-radiation emitted by their lamp. They also carefully measured the lamp photon flux by both chemical actinometry and using a calibrated silicon photodiode.

Case studies of the photodestruction of optically thin CH_4[164], NH_3[164], CO_2[142] and CH_3OH[163] ices report larger cross sections than those found by Cottin et al. [48]. It has been suggested that these discrepancies may arise due to deviations from first-order kinetics when the ices are thicker than the UV-penetration depth[167]. Other explanations could include under- or over-estimations in the photon fluxes as well a wavelength or fluence dependencies.

In this chapter, we study the photodestruction of optically thin CO_2, CH_4, H_2O, NH_3, CH_3OH ices. We aim to produce a consistent measurement set with well understood opacitites and UV fluxes, covering a range of ice mixtures and temperatures. To understand the effects of ice optical depth, we measure the photodestruction rates for pure ices at different thicknesses. We then study the photodestruction rates at different ice temperatures to determine whether increased diffusion of photo-fragments influences the net photodestruction cross sections. This can provide clues about the energetically available routes that reform the parent molecules. We measure the photodestruction rates of the ice species in various binary ice mixtures and discuss the relative changes in the photodestruction cross sections compared to the pure ices.

In the following sections 6.1.1-6.1.5 we describe the energetically available gas-phase photodissociation processes for each of molecules in the vacuum ultraviolet (VUV) and compare these to existing data for ices.

6.1.1 CARBON DIOXIDE

Photodissociation of CO_2 gas has been extensively studied due to its importance in the atmospheres of Earth, Mars and Venus [12, 40, 139, 203, 205]. CO_2 photolysis in the gas-phase occurs via the following channels [170]:

$$
\begin{aligned}
CO_2 &\longrightarrow CO + O(^3P) \quad \lambda \geq 167\,\mathrm{nm} && (6.1)\\
&\longrightarrow CO + O(^1D) \quad \lambda = 167\,\mathrm{nm} - 120\,\mathrm{nm} && (6.2)\\
&\longrightarrow CO + O(^1S) \quad \lambda < 120\,\mathrm{nm} && (6.3)
\end{aligned}
$$

The first generation photoproducts in the photodissociation of CO_2 ice are likewise CO and O. In the ice, the CO and O photofragments can be involved in further reactions to produce CO_3, O_2, O_3 and to reform CO_2 [14, 15, 90, 112]:

Table 6.1.1. Previously measured photodestruction cross sections for the species measured in this study along with the experimental parameters used to make the measurements.

Ice species	gas-phase $\sigma_{Ly\alpha}$ (cm^2)	Pure Ice σ (cm^2)	Temperature (K)	Ice thickness	Lamp emission (nm)	Flux (photon cm^{-2} s^{-1})	Reference*
H_2O	1.2×10^{-17}	...	...	...	...	...	...
NH_3	8.4×10^{-18}	3.2×10^{-20}	<20	~1 μm	mostly 160	$3x10^{14}$	(1)
		$1.4[0.7]\times10^{-18}$	30	51 ML	160 & 121	$1.1x10^{13}$	(2)
CO	zero at Lyα	$<1\times10^{-21a}$	<20	~1 μm	mostly 160	$3x10^{14}$	(1)
		$<8.0\times10^{-20\ a}$	10	$\sim$100 nm	broadband[b]	$\sim10^{15}$	(3)
CO_2	6.5×10^{-20}	3.8×10^{-19}	<20	~1 μm	mostly 160	$3x10^{14}$	(1)
		5.6×10^{-19}	10	$\sim$100 nm	broadband[b]	$\sim10^{15}$	(3)
		7.3×10^{-20}	75	50 nm	mostly 121	2.7×10^{14}	(4)
		$9.5[2.9]\times10^{-18}$	8	200 ML	5.8% 121	$2x10^{14}$	(5)
CH_4	1.8×10^{-17}	9.1×10^{-20}	<20	~1 μm	mostly 160	$3x10^{14}$	(1)
		$5.0[3.0]\times10^{-19}$	30	47 ML	160 & 121	$1.1x10^{13}$	(2)
		7.2×10^{-19}	10	$\sim$100 nm	broadband[b]	$\sim10^{15}$	(3)
CH_3OH	1.4×10^{-17}	5.0×10^{-19}	<20	~1 μm	mostly 160	$3x10^{14}$	(1)
		1.6×10^{-18}	10	$\sim$100 nm	broadband[b]	$\sim10^{15}$	(3)
		$2.6[0.9]\times10^{-18}$	20	20 ML	160 & 121	10^{13}	(6)
		$2.4[0.8]\times10^{-18}$	30	20 ML	160 & 121	10^{13}	(6)
		$3.3[1.1]\times10^{-18}$	50	20 ML	160 & 121	10^{13}	(6)

*References: (1) Cottin et al. [48], (2) Öberg et al. [164], (3) Gerakines et al. [90], (4) Yuan & Yates [234], (5) Martín-Doménech et al. [142], (6) Öberg et al. [163]

[a] upper limit

[b] five lines: 121, 136, 145, 160 & 280 nm

$$\mathrm{CO(X^1\Sigma^+) + O \longrightarrow CO_2} \tag{6.4}$$

$$\mathrm{CO(X^1\Sigma^+) + CO^* \longrightarrow CO_2(X^1\Sigma_g{}^+) + C(^3P)} \tag{6.5}$$

$$\mathrm{CO_2 + O \longrightarrow CO_3} \tag{6.6}$$

$$\mathrm{CO_3} + h\nu \longrightarrow \mathrm{CO_2 + O(^3P)} \tag{6.7}$$

$$\mathrm{O + O \longrightarrow O_2} \tag{6.8}$$

$$\mathrm{O_2(X^3\Sigma_g{}^-) + O \longrightarrow O_3} \tag{6.9}$$

Whether reaction (6.4) can produce CO_2 under interstellar conditions has been controversial due to uncertainty in the reaction barrier, which is typically assigned a value in the range of 290–1000 K [56, 185]. If a barrier of 1000 K is assumed, the reaction probability is low and may proceed by tunneling under dense cloud conditions. Work by Fournier et al. [79] showed efficient formation of CO_2 by CO + O(^{3}P) in argon matrices with rates inconsistent with a large barrier. With the input of energy (e.g. UV photons), CO_2 can be reformed by reactions (6.5) and (6.7) during pure CO_2 ice photolysis. The CO + O channel could also be more efficient than in the thermal case due to the presence of electronically excited O(^{1}D), which may have have enough excess energy to efficiently overcome the reaction barrier [140].

The CO_2 absorption cross section at Lyman-alpha is enhanced in the solid state with respect to the gas-phase (though the gas-phase cross sections are higher at other VUV wavelengths), increasing from 6.5×10^{-20} cm^2 [107] to 1.0×10^{-18} cm^2 [50]. UV-photodestruction cross-sections for pure CO_2 ice have been reported in four different studies and range from 7.3×10^{-20} cm^2 [234] to 9.5×10^{-18} cm^2 [142]; i.e. differing by a factor of one hundred and producing quantum efficiencies between $\sim$0.07-25. The lowest cross section recorded was measured by Yuan & Yates [234] for 50 nm CO_2 ice at 75 K irradiated with a Lyman-alpha dominated lamp, while the largest cross section was measured by Martín-Doménech et al. [142] for 200 ML CO_2 at 8 K irradiated with an H_2 lamp producing a broad emission peaking 160 nm and to a lesser extent at 121 nm. Carbon dioxide photodesorption has also been studied in detail and is shown to be limited to energies above 10.5 eV for pure CO_2 ice, but also may be induced by an indirect desorption induced by electronic transition (DIET) mechanism involving the excitation of photoproduced CO [78]. At VUV wavelengths of typical hydrogen lamps the photodesorption is shown to be dominated by CO desorption with a low yield for intact CO_2 [142].

6.1.2 METHANE

Gas-phase methane is photodissociated at Lyman-alpha forming methyl (CH_3), methylene (CH_2) and methylidyne (CH) radicals with quantum yields of 0.44, 0.5 and 0.06, respectively [170]. The spin allowed channels are [45, 184]:

$$\begin{aligned}
CH_4 &\longrightarrow CH_3(X^2A_2) + H && (6.10)\\
&\longrightarrow CH_2(a^1A_1) + H_2 && (6.11)\\
&\longrightarrow CH_2(b^1B_1) + H_2 && (6.12)\\
&\longrightarrow CH_2(X^3B_1) + 2\,H && (6.13)\\
&\longrightarrow CH_2(a^1A_1) + 2\,H && (6.14)\\
&\longrightarrow CH(X^2\Pi) + H_2 + H && (6.15)\\
&\longrightarrow C(^1D) + 2\,H_2 && (6.16)
\end{aligned}$$

The photolysis of methane ice at 20 K using a hydrogen-discharge lamp has been shown to produce primarily methyl radicals with a branching ratio of 0.95 [26]. This is markedly different from gas-phase studies which indicate lower yields of CH_3 possibly due to secondary fragmentation into CH_2 [97, 130]. Reactions between primary photoproducts (CH_3, CH_2 and CH) have been shown to produce ethane and ethylene as well as allene (C_2H_3), propane and higher order unsaturated and branched hydrocarbons [90].

The methane VUV absorption spectrum is particularly wavelength dependent within the spectral range of typical H_2 lamps. Methane absorbs strongly at Ly-α with a cross section of 1.5×10^{-17} cm^2 and has almost no absorption in the Lyman band system [50]. As a result, the optical thicknesses of ices grown in previous studies of CH_4 ice photodestruction depend strongly on the lamp emission profile employed. Likewise, methane photodesorption has been shown to follow the absorption spectrum, desorbing for energies higher than 9.1 eV [65].

Photodestruction cross sections have been reported for a range of CH_4 ice thicknesses using broadband hydrogen discharge lamps. Gerakines et al. [90] a report photodestruction cross section for 100 nm ($\sim$170 ML) thick CH_4 ice of 7.2×10^{-19} cm^2. At this thickness the ices are optically thin to wavelengths in the Lyman-band system and absorb ~90% of the Lyman-α photons. Cottin et al. [48] found a lower cross section of 0.91×10^{-19} cm^2 for ices estimated to be 0.5-1.5 μm thick. In this case, the ices may be optically thick to all the VUV photons, possibly explaining the lower cross section measured. Öberg et al. [164] irradiated a 47 ML thick methane ice at 30 K with a broadband H_2 lamp and found a cross section of $5.0[3.0]\times10^{-19}$ cm^2. Here, all VUV photon wavelengths penetrate the depth of the ice. It is clear from these measurements that the wavelengths emitted from different lamps, and consequently the thickness dependent opacities at those wavelengths, is an important factor influencing the derived photodestruction cross sections for methane ices.

6.1.3 WATER

Despite the prevalence of water in the ISM (reviewed in van Dishoeck et al. [222]), the UV-photodestruction cross section for water ice has not been quantified by laboratory measurement. Extracting the water loss from IR spectra during UV-irradiation is challenging because of band shape changes due to photo-induced structural rearrangement of the ice lattice, as well as background water deposition on either the ice substrate or the cooled IR detector. UV photons below 280 nm can result in the dissociation of H_2O occurring by the major channel [170]:

$$H_2O \longrightarrow OH + H \tag{6.17}$$

In the gas-phase, a $\sim$10% branching ratio at Lyman-alpha exists for the dissociation channel [170, 206]:

$$H_2O \longrightarrow O(^1D) + H_2 \tag{6.18}$$

Heays et al. [107] likewise report a gas-phase branching ratio of 10% for channel 6.18, but also include the possibility of forming $2H(^2S) + O(^3P)$ resulting in an overall branching ratio of 0.74:0.26 for the production of OH and O respectively [204].

Absorption of VUV photons in the wavelength range of typical H_2-lamps occurs by two main band systems. The first absorption band between $\sim$130-160 nm and is attributed to the $4a_1{:}A^1B_1 \leftarrow 1b_1{:}X^1A_1$ transition; the second, between 120-130 nm, is attributed to $B^1A_1 \leftarrow X^1A_1$. The VUV absorption cross sections for water ice reported by Cruz-Diaz et al. [49] are 5.2×10^{-18} cm^2 and 0.7×10^{-18} cm^2 at 121.6 nm and 160.8 nm, respectively, and are lower than the gas-phase value of 1.36×10^{-17} cm^2 at Lyman-alpha [107]. The cross section for photodissociation of H_2O at Lyman-alpha is reported as 1.53×10^{-17} cm^2 [107], giving a gas-phase quantum efficiency for

H_2O Ly-α photodissociation of close to 1.

A number of studies have been conducted to explore the cage effect in the photodissociation of water in rare-gas matrices [195–197, 209]. Schriever et al. [196] report a barrier to exit of the H_2O-rare-gas cage of $\sim$1.8 eV due to repulsive H-rare-gas potentials. It is expected that the cage barrier in pure water ice should be substantially higher due to strong H-bonding between neighbouring H_2O molecules. In order to assess the magnitude of the cage effect in pure H_2O ices, we aim to measure the photodestruction cross section for water ice and extract the quantum efficiency by direct comparison to the H_2O ice VUV-absorption spectrum.

6.1.4 AMMONIA

Ammonia ice has been detected towards protostars and quiescent clouds with abundances typically $<$10% with respect to water ice (e.g. Boogert et al. [24], Dartois & d'Hendecourt [59], Lacy et al. [125]). In the gas-phase ammonia is dissociated in two spin-allowed channels Okabe [170]:

$$
\begin{aligned}
NH_3 &\longrightarrow NH_2 + H && (6.19)\\
&\longrightarrow NH + H_2 && (6.20)\\
& && (6.21)
\end{aligned}
$$

The thresholds for NH_2 and NH production are reported to be 4.4 eV and 5.5 eV in the gas-phase respectively [169, 170]. In the ice, the products of the primary photodestruction can then react further to form nitrogen, hydrogen and hydrazine [90]:

$$NH + NH_3 \longrightarrow N_2H_4 \tag{6.22}$$

$$NH + NH \longrightarrow N_2 + 2\,H \tag{6.23}$$

$$NH_2 + NH_2 \longrightarrow N_2H_4 \tag{6.24}$$

Ammonia ice photodestruction has been studied under a range of conditions [48, 90, 138, 164] Gerakines et al. [90] showed that photolysis of pure ammonia ice produced NH_2 and N_2H_4 but were unable to report a photodestruction cross section. Loeffler & Baragiola [138] irradiated ammonia ice films using pulses of 193 nm (6.4 eV) light produced by an ArF excimer laser. They found that at fluences $<1\times10^{19}$ photons cm^{-2} analysis was complicated by band sharpening indicating crystallization effects. At a fluence of 3.7×10^{19} photons cm^{-2} they found a low quantum efficiency for NH_3 photodestruction of 0.01. Cottin et al. [48] likewise found a low photodestruction cross section for ammonia ice of 3.2×10^{-20} cm^2 which increased when the NH_3 was mixed within an N_2 matrix, suggesting that in pure NH_3 ices there is a strong cage effect.

Öberg et al. [164] studied the photodestruction of $\sim$50 ML thick NH_3 ices at 30 K for fluences of $\sim2\times10^{17}$ photons cm^{-2}. They report a cross section of $1.4[0.7]\times10^{-18}$ cm^2. The spectra reported do not show evidence for band sharpening, possibly indicating thickness effects on the UV-induced structural changes, or different extents of local thermal heating from the different UV-sources.

6.1.5 METHANOL

Solid methanol is the most complex molecule detected in interstellar ices thus far and and is believed to form predominantly by the hydrogenation of CO on icy grains [81, 224]. Methanol may be the starting point for the formation of more complex organics and as a result, photo-processing of methanol-bearing ices has been the subject of a number laboratory studies (e.g. Baratta et al. [11], Krim et al. [120], Öberg et al. [163]). In the gas-phase the following photodissociation channels have been proposed:

$$\begin{aligned} CH_3OH &\longrightarrow CH_2OH + H && (6.25) \\ &\longrightarrow CH_3O + H && (6.26) \\ &\longrightarrow CH_3 + OH && (6.27) \\ &\longrightarrow H_2CO + H_2 && (6.28) \end{aligned}$$

The branching ratios of the photolysis channels is of substantial importance for input into astrochemical models. Matrix isolation experiments by Jacox & Milligan [113] revealed a substantial yield of CH_2OH during the photolysis of methanol embedded in a xenon matrix. Öberg et al. [163] quantitatively monitored the photodestruction of methanol ice and the formation rates of complex organics during the irradiation using a hydrogen discharge lamp peaking at 160 nm. The branching ratios in the ice were calculated as 73%, 15% and 12% for channels (6.25), (6.26) and (6.27) respectively, with the direct formation of formaldehyde expected to be negligible. Measurements of the gas-phase photolysis of methanol using mass spectrometry [101] give 75% channels (6.25)+(6.26), 5% (6.27) and 20% (6.28); however, the CH_2OH and CH_3O channels are indistinguishable due to the identical masses of the products. Work is currently being undertaken to measure the branching ratios using rotational spectroscopy. The relative importance of these branching ratios in gas- versus solid-phase remains an open question [124].

6.2 EXPERIMENTAL DETAILS

In this study, we aim to produce a consistent set of solid-phase photodestruction cross sections using well understood lamp emission spectral profiles and photon fluxes, as well as constrained ice opacities. Our experimental design is motivated by the following parameters:

1. Ice thickness: we aim to determine the thickness range in which ices can be considered optically thin to the VUV-radiation emitted by the UV-sources. This will allow us to assess the validity of using first-order kinetics to extract the photodestruction cross sections.

2. Lamp emission: we wish to understand whether ice photodestruction quantum efficiencies have wavelength dependencies across the bandwidth of typical hydrogen-discharge lamps.

3. Lamp flux: we aim to evaluate the extent to which uncertainties in photon fluxes can account for discrepancies in the measured photodestruction cross sections reported in the astronomical literature. We aim to minimize uncertainties in our lamp fluxes in order to best report absolute cross sections and quantum efficiencies.

4. Cage effects: we plan to measure the ice photodestruction cross sections in various diffusive environments, including at different temperatures and in different ice matrices, in order to assess the relative importance of immediate energy dissipation or recombination versus dissociation and photofragment diffusion in various astronomically relevant ices.

To achieve aim (1), we make preliminary measurements of the photodestruction for pure ices of different thicknesses (section 6.3.1) and determine whether changes in the photodestruction cross sections can be explained by the ice optical depth. To address the wavelength dependencies of aim (2),we use two different hydrogen lamps with different emission profile, shown in Figure 6.2.1, to make measurements of ice photodestruction at different wavelengths: an H_2/Ar lamp that produces primarily Lyman-alpha (Chamber 1) and a H_2/D_2 lamp (Hamamatsu) that produces a mixture of Lyman-alpha and Lyman-band emission, peaking at 161 nm (Chamber 2). The H_2/D_2 lamp emission can be modified to using a sapphire window to totally absorb the Lyman-alpha component. To minimize the uncertainty in our lamp photon fluxes ,in accordance with aim (3), we use a range of flux measurement techniques utilizing both chemical actinometers as well as a calibrated photodiode. We then combine these facets to address aim (4) by measuring the ice photodestrucion rates over different temperatures and in binary ice mixtures. The two experimental setups used to make these measurements are described in brief below.

Chamber 1 is a high vacuum system (base pressure $\sim$1 x 10^{-8} Torr, dominated by H_2) modified from Yuan & Yates [234] and described in Cooke et al. [46]. The ices are condensed on an IR transparent substrate, a 0.3 cm^2 a disk of ground KBr that was hydraulically pressed into a tungsten grid. The substrate is suspended into the chamber by an OFHC copper coldfinger that is cooled by a closed cycle helium cryostat (Air products Displex DE 202-0SP expander and APD Cryogenics HC-4 compressor). The substrate is cooled to as low as 25 K and the temperature is monitored using a k-type thermocouple welded to tantalum foil and attached to the W-grid close to the KBr disk. The temperature is monitored and controlled using a custom Labview program. Infrared spectra were collected using a Bruker Tensor 27 FTIR spectrometer and a liquid-N_2 cooled MCT detector. The residual gas-phase partial pressures are monitored by an RGA 200 quadrupole mass spectrometer (QMS).

Chamber 2 is described previously in Lauck et al. [129]. Briefly, the experiment consists of an UHV chamber with a base pressure of $\sim 4 \times 10^{-10}$ Torr at room temperature. The ices are deposited onto a CsI window cooled to as low as $\sim$11 K using a closed-cycle Helium cryostat (ARS). These ices are grown using a 4.8 mm gas doser that is positioned close to the CsI subtrate at normal incidence. The temperature of the substrate is monitored and controlled using a

LakeShore Model 335 controller with two calibrated silicon diode sensors that have an estimated accuracy of 2 K and a relative uncertainty of 0.1 K. Transmission infrared spectra of the ices are obtained using a Fourier transform infrared (FTIR) spectrometer (Bruker Vertex 70v). Gas partial pressures were monitored during the experiments using a quadrupole mass spectrometer (Pfeiffer QMG 220M1).

6.2.1 ICE DEPOSITION

Ices were deposited in both chambers using gas dosers directed at the IR transparent substrates. The thickness of the ice is monitored by infrared spectroscopy during dosing until the desired thickness is reached based the ice optical depths shown in Figure 6.2.2 and the results of the preliminary thickness measurements in 6.3.1. The percentage of photons absorbed by the ice film (%Abs) is calculated by:

$$\%\text{Abs} = 100[1 - \exp(-\sigma_{\mathit{eff}} N)] \tag{6.29}$$

Where σ_{eff} is the effective absorption cross section at the lamp emission wavelengths in cm^2, and N is the ice column density in molecules/cm^2. The effective optical depths were calculated using the absorption cross sections reported by Cruz-Diaz et al. [49, 50] based on VUV spectroscopic measurements of ice films condensed on a MgF_2 window and exposed to photons from a broad-band hydrogen-discharge lamp. The ice column densities are calculated using the integrated infrared absorbances and the band strengths listed in Bouilloud et al. [28]. The preliminary ice thicknesses were chosen to ensure optical depths <1 for all VUV wavelengths emitted by the H_2 lamps, typically 20-200 ML. The most absorptive ice, CH_4, absorbs 99% of the Lyman-alpha photons at 330 ML, whereas the least absorptive, CO_2, doesn't absorb 99% until 4600 ML. The VUV-absorption is lower in the Lyman-band system for all of the ice species

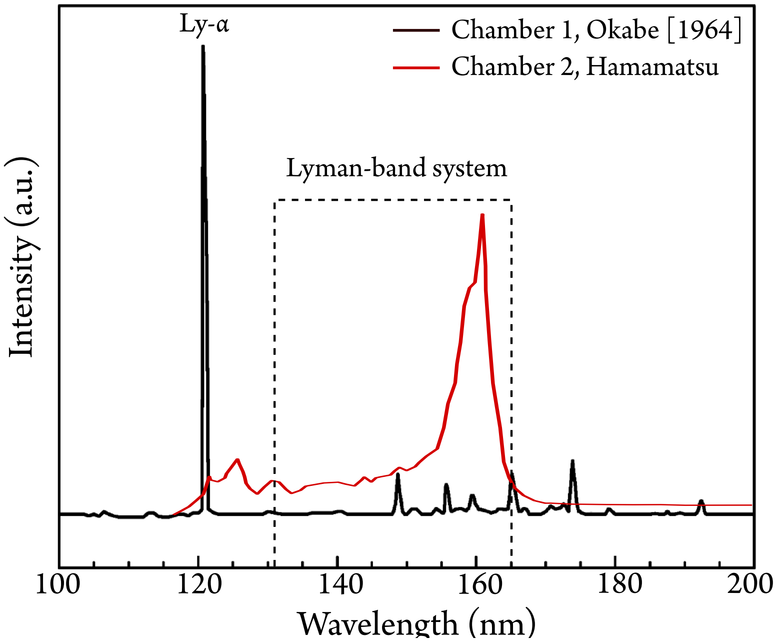

Figure 6.2.1: Expected emission spectra for the MDHL lamps used in this study. The emission intensities are scaled for clarity. The spectrum for Chamber 1 is taken from Okabe [168] for a similar lamp using 10% H_2 in Ar at 1 Torr. The emission spectrum for Chamber 2 is measured by McPherson Inc.

measured so we chose the preliminary ice thickness based on the higher absorption at Lyman-alpha.

6.2.2 LAMP DESCRIPTION AND FLUX CALIBRATIONS

Accurate flux calibration is essential to the measurement of reproducible photodestruction cross sections. We use several different flux measurement and calibration procedures based on physical measurements of the photon flux (photodiode) and indirect chemical actinometers (O_2 ice, N_2O(g), CO_2(g)). We describe the UV-source used in each chamber and the methods used to measure the photon fluxes below. Table 6.2.1 shows the fluxes obtained using the different

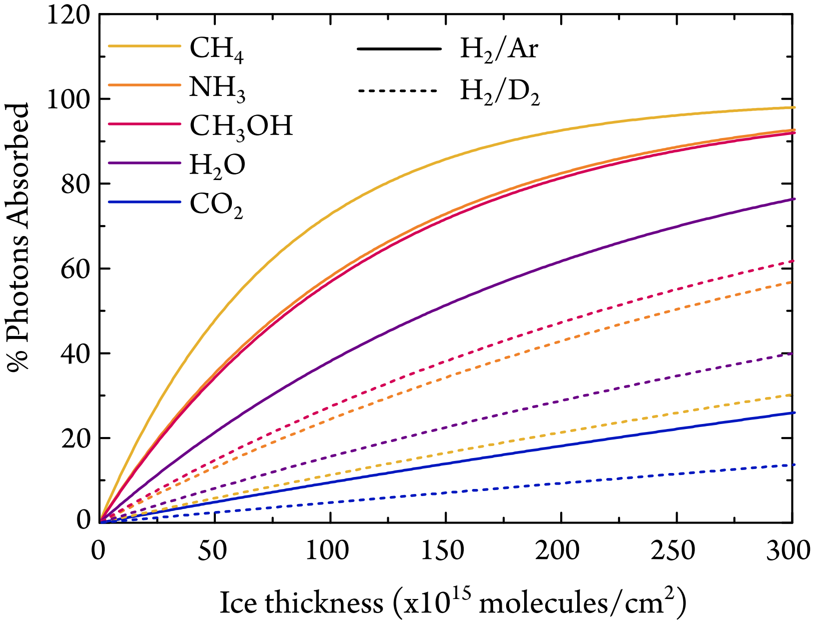

Figure 6.2.2: Percentage of photons absorbed for each of the ices in this study as a function of the ice thickness. The percentage of photons absorbed is calculated by convolving the absorption spectra from Cruz-Diaz et al. [49, 50] with the lamp emission from the H_2/Ar and H_2/D_2 lamps.

measurement methods.

Chamber 1: A microwave discharge hydrogen flow lamp (Opthos Instruments) was used as the UV-source. It has been described in detail previously in Rajappan et al. [181]. The microwave power was kept at 60 W for the duration of the experiments. A mixture of 90% Ar, 10% H_2 was used to produce UV light with a sharp Lyman-alpha feature [168].

N_2O(g) Actinometry: The photon flux of our UV lamp was originally calibrated using N_2O actinometry as described in detail in Rajappan et al. [181]. We chose this method due to the high UV absorption cross section of N_2O at Lyman-alpha compared to other VUV wavelengths ($>1\times10^{-17}$ cm^2). This has the advantage that the photons destroying N_2O will be above 140 nm so any contribution from $<$140 nm emission should be negligible. The total volume of the photolysis cell is calibrated using a known volume of helium gas and found to be 2.7 L. We find

Table 6.2.1. Photon fluxes, in units of photons cm^{-2} s^{-1}, obtained via chemical various chemical actinometry methods and using a calibrated silicon photodiode. The flux methods we have used to calculate kinetic parameters in this thesis are shown in bold.

Method	Chamber 1: H_2/Ar	Chamber 2: H_2/D_2
N_2O(g)	3.0×10^{14}	—
CO_2(g)	4.8×10^{14}	—
Total Photodiode	—	1.1×10^{14}
<220 nm Photodiode*	—	$\mathbf{8.1\times10^{13}}$
O_2(ice)	$\mathbf{8.3\times10^{13}}$	2.4×10^{13}

*The <220 nm photodiode reading refers to the corrected diode reading taking into account the diode responsivity in the visible

that the photon flux obtained from N_2O actinometry is 3.0×10^{14} photons cm^{-2} s^{-1} at the 45° KBr substrate.

CO_2(g) Actinometry As a secondary flux calibration we use CO_2 actinometry. CO_2 absorbs at wavelengths longer than 140 nm and therefore, in contrast to N_2O, will measure flux from any emission at 160 nm. This method has the advantage that there is only one main channel for CO_2 photolysis in the VUV, that is the formation of CO and O which occurs with a quantum yield of 1. The disadvantage compared to N_2O actinometry is that CO_2 has a very low absorption cross section at Lyman-alpha of 4.8×10^{-20} cm^2 [107]. The low cross section means that CO_2 absorbs only ~30% of the Lyman-alpha photons in the length of the absorption cell. The flux is then corrected for photon absorption using:

$$Flux = \frac{\Delta P_{CO_2}}{\Delta t}\frac{V}{k_B T}\frac{1}{\varphi_{Lya}\beta_{Lya}} \tag{6.30}$$

$$\beta_{Lya} = 1 - \exp(\varepsilon l P_{CO_2}) \tag{6.31}$$

Where P_{CO_2} is the partial pressure of CO_2, V is the calibrated cell volume, T is the gas temperature, φ_{Lya} is the quantum efficiency for CO_2 destruction at Lyman-alpha. Beta is a factor used to correct for the proportion of photons absorbed in the cell column and is obtained using ε_{Lya} = 1.61 atm cm^{-1} [232]. We use a calibration curve from concurrent measurements of various CO_2 partial pressures (using a baratron gauge) and its IR spectra to convert the CO_2 integrated absorbance to partial pressure. We find that the photon flux obtained from CO_2 gas actinometry is 4.8×10^{14} photons cm^{-2} s^{-1} at the 45° KBr substrate.

Oxygen Actinometry: The accuracy of the flux measured by gas-phase actinometry methods relies on the same number of photons per area hitting the ice film as the gas column. This may not be the case if the UV-beam is divergent or is larger than the IR substrate or if the IR probe spot is not centered on the UV-beam. The gas-phase actinometry methods also rely on accurate knowledge of the chamber geometries and volume. Because of this, we also compare the fluxes obtained via the gas-phase actinometers to solid phase actinometry that more directly probes the number of photons incident on the ice films. Oxygen actinometry utilizes the photolysis of O_2 to form ozone, which has been well documented in the gas-phase with a quantum yield of 1.92[100]. O_2 ices have been used similarly to measure the flux impinging on ices [48, 91]; however, due to a lack of solid-phase data, gas-phase ozone values have been typically used. Cottin et al. [48] used the gas-phase quantum yield and ozone band strength but employed a solid phase scaling factor based on photodiode measurements.

A recent study by Fulvio et al. [82] employed a gold photodetector to independently calibrate the ozone yield for oxygen ice photolysis at both 122 nm and 160 nm. Additionally, a solid state ozone band strength has been measured by Loeffler et al. [137] in RAIRS. We find the flux obtained using O_2 actinometry was 8.3×10^{13} photon cm^{-2} s^{-1}, lower than the values obtained using the gas-phase actinometers.

Lamp long-term flux stability: To evaluate the stability of the lamp flux over time, we ran repeat measurements of CO_2 ice photodestruction cross sections on a weekly or biweekly basis. We standardize this measurement by depositing and photoirradiating CO_2 ices 40-50 ML thick at 25 K. We also record the resistance measured by a diode that is placed outside of the vacuum near the end of the lamp. The diode does not give us a direct measurement of the UV photon flux but rather serves to check variations in the visible light emission from the lamp from day-to-day. Using this method we adjust the photon flux for deviations from the flux measurement by actinometry. These long-term calibrations give an average flux over a 1 year period of 7.6×10^{13} photons cm^{2} s^{-1}, with a standard deviation of 2.6×10^{13} photons cm^{-2} s^{-1}.

Chamber 2: An H_2/D_2 lamp (Hamamatsu L11798) was used as a VUV-source. This source has a spectral distribution that peaks at the H_2 161 nm line and to a lesser extent at Lyman-alpha. The lamp can be filtered either by a MgF_2 window, or a sapphire window to cut off the contribution from Lyman-alpha.

Photodiode Measurements: The photon flux from the UV lamp was measured with a NIST calibrated AXUV-100G photo-diode at the beginning and end of each experiment. The average total flux obtained over the experimental period was 9.9×10^{13} photons cm^{2} s^{-1} using the MgF_2 window, and 4.0×10^{13} photons cm^{2} s^{-1} using the sapphire window. The flux obtained from the photodiode may be overestimated due to the high diode response at visible wavelengths. In order to subtract visible (non-dissociative) flux we convolve the diode response in the visible with the lamp spectrum measured between 220-700 nm. We find that the emission from the lamp at wavelengths >220 nm contributes ~25% of the measured photocurrent. Oxygen actinometry was also performed as described for Chamber 1. The flux obtained using O_2 actinometry was

2.4×10^{13} photons cm^{-2} s^{-1} with a concurrent photodiode reading giving a total flux of 1.1×10^{14} photons cm^{-2} s^{-1} (UV flux of 8.1×10^{13} photons cm^{-2} s^{-1}) i.e. ∼30% of the UV-flux obtained using the photodiode.

Comparison of Flux Measurement methods

Table 6.2.1 shows the fluxes obtained via the various calibration methods. The O_2 actinometry measurements gave lower fluxes than both the photodiode reading and the gas-phase actinometers. O_2 actinometry may give an underestimate of the VUV photon flux if all of the photons emitted by the lamp aren't absorbed by the O_2 film or the quantum yields for ozone production overestimated. Another possibility is that ozone production rate depends on the ice thickness, a parameter that is quite uncertain given the weak intensity of the forbidden O_2 IR mode.

The gas-phase actinometers may overestimate the photon flux if the IR spot is probing a region of the O_2 film where the UV beam is not centered. In the same manner, the photodiode may give an overestimated flux if the diode collects more photons per area than the ice film i.e. if the diode is centered on the UV beam and the ice spot is not. We find that even after subtracting the visible contribution, the photon flux measured by the diode is still at least a factor of three larger than that measured using O_2 actinometry. This indicates that another source of uncertainty in the flux measurement methods that will need to be addressed in order to minimize the absolute uncertainties on the kinetic parameters reported in this study. In this thesis, we use the flux obtained by O_2 actinometry in Chamber 1 and the flux obtained from the corrected photodiode measurement in Chamber 2 for calculations of the photodestruction cross sections (shown in bold in Table 6.2.1). The values may therefore be revised for publication once we best determine the most reliable flux measurement method.

Currently, we are implementing methods in both labs to reduce the flux uncertainties. In

Chamber 1, we have recently made a photo-detector by evaporative deposition of gold onto a glass substrate. The gold spot is suspended into the chamber in the position of the IR substrate and attached by means of a feed-through to a DC power supply which applies a bias voltage to the gold film and forces the photoelectrons emitted by the gold to be collected by the walls of the chamber (which is grounded). The saturation photo-current is then measured and directly related to the photon flux. This technique is described in detail in Fulvio et al. [82] and in Chapter 2 of this thesis. In Chamber 2, we are planning to utilize a lens system to independently focus different VUV-wavelengths onto the IR substrate. This involves a UV transparent lens (MgF_2 or LiF) that focuses the lamp's arc point onto a 2 mm aperture. A linear translation stage is used to focus the desired wavelength at the aperture.

Quantum Yields: The quantum yields for solid phase photodestruction are calculated using the VUV-absorption cross spectra reported by Cruz-Diaz et al. [49, 50]. In the case of the H_2/Ar lamp, we assume the lamp emits ~80% Lyman-alpha and the other 20% at 132 nm, based on VUV absorption measurements by Chen et al. [34] (and private communication) for similar lamp configurations. For the H_2/D_2 lamp, we convolve the lamp emission spectrum with the absorption spectra of the ice and with the filter window transmission where relevant. The effective absorption cross sections obtained from the convolutions are listed in Table 6.2.2. In the case of CO_2 ice, we are not able to convolve the absorption spectrum with that of the lamp due to the strong absorption from photo-produced CO. Instead, we estimate the effective absorption cross sections for the H_2/D_2 lamp by taking 20% of the value at Lyman-alpha and 80% of the average value of the Lyman band system. To compare to the gas-phase quantum yields, we use the photodissociation cross sections and absorption cross sections reported in Heays et al. [107] and references therein.

Table 6.2.2. Effective ice absorption cross sections from the convolution of the ice absorption spectra with the lamp emission profiles.

Ice	$\sigma_{Abs}(H_2/Ar)$	$\sigma_{Abs}(H_2/D_2)$	$\sigma_{Abs}(H_2/D_2$ filtered$)$
CO_2	1.0×10^{-18}	$4.9\times10^{-19*}$	$3.6\times10^{-19*}$
CH_4	1.3×10^{-17}	1.2×10^{-18}	3.5×10^{-19}
NH_3	8.7×10^{-18}	2.8×10^{-18}	3.4×10^{-18}
H_2O	4.8×10^{-18}	1.7×10^{-18}	2.0×10^{-18}
CH_3OH	8.4×10^{-18}	3.2×10^{-18}	3.9×10^{-18}

*Estimate based on subtracting the CO absorption spectrum.

6.3 RESULTS

In sections 6.3.1 we report the results of the photodestruction measurements for the pure ices. The cross sections obtained for the pure ice measurements are reported in table 6.3.1 and displayed in figures 6.3.1-6.3.6.

We first conduct preliminary experiments to measure whether the pure ice photodestruction cross sections change with ice thickness within the thickness regime where the photons totally penetrate the ice depth. We measure the photodestruction cross sections for CO_2, CH_4, NH_3 and CH_3OH at different thicknesses and therefore different opacities to the VUV-photons. The cross sections are obtained assuming first-order kinetics and therefore changes in the cross section with ice thickness can either represent "true" changes in the photodestruction rates e.g by increased trapping of photoproducts, or can indicate limitations in the first-order kinetics model. The percentage of photons absorbed as a function of ice depth is shown in 6.2.2 based on the convolved absorption cross sections from the absorption spectra of Cruz-Diaz et al. [50] shown in Table 6.2.2. These measurements motivate the ice thicknesses chosen to explore the effects of ice thickness.

Following the preliminary ice thickness experiments, we measured the photodestruction of pure CO_2, CH_4, NH_3 and CH_3OH at various ice temperatures in order to study how of diffusion of photo-fragments affects the net photodestruction cross sections. The photodestruction cross sections obtained for pure ices at different temperatures are reported in 6.3.1 and figures 6.3.1-6.3.6. The quantum efficiencies obtained from the pure ice experiments are summarized in Figure 6.4.1.

In section 6.3.2 we report the net photodestruction cross sections for the binary ice mixtures with respect to the pure ices. The photodestruction kinetics and cross sections are displayed in figures 6.3.7-6.3.2 and well as in table 6.3.3. In section 6.4 we present the photodestruction cross sections obtained using the H_2/D_2 lamp make preliminary comparisons to the results obtained using the Ly-α dominated H_2/Ar lamp.

Table 6.3.1. Pure ice photodestruction cross sections measured in this study for various ice temperatures, thicknesses and using the different UV-sources

Ice	Lamp configuration	T_{ice} (K)	Ice thickness (ML)*	Photodestruction σ (cm^2)	Quantum yield
CO_2	H_2/Ar 10%	25	135	4.1×10^{-19}	0.41
	H_2/Ar 10%	25	60	4.1×10^{-19}	0.41
	H_2/Ar 10%	40	62	4.1×10^{-19}	0.41
	H_2/Ar 10%	55	68	3.8×10^{-19}	0.38
	H_2/Ar 10%	65	76	4.0×10^{-19}	0.40
	H_2/D_2 MgF_2	25	67	2.0×10^{-19}	0.41
	H_2/D_2 sapphire	25	65	$<1.6\times10^{-19}$	<0.44
$^{13}CO_2$	H_2/Ar 10%	25	42	3.7×10^{-19}	0.37
CH_4	H_2/Ar 10%	25	100	4.9×10^{-19}	0.03
	H_2/Ar 10%	25	48	8.7×10^{-19}	0.06
	H_2/Ar 10%	25	34	9.2×10^{-19}	0.06
	H_2/D_2 MgF_2	15	36	1.7×10^{-19}	0.14
	H_2/D_2 MgF_2	20	32	1.5×10^{-19}	0.13
	H_2/D_2 MgF_2	20	13	2.9×10^{-19}	0.24
	H_2/D_2 MgF_2	25	16	4.5×10^{-19}	0.38
	H_2/D_2 sapphire	25	39	$<2.3\times10^{-19}$	<0.65
NH_3	H_2/Ar 10%	25	187	$<1\times10^{-20}$	<0.001
	H_2/Ar 10%	25	87	3.3×10^{-20}	0.004
	H_2/Ar 10%	40	85	7.2×10^{-20}	0.008
	H_2/Ar 10%	55	94	1.1×10^{-19}	0.012
	H_2/Ar 10%	70	96	1.5×10^{-19}	0.017
	H_2/D_2 MgF_2	25	31	3.3×10^{-19}	0.12
	H_2/D_2 sapphire	25	32	1.1×10^{-18}	0.32

6.3.1 PURE ICES

Carbon Dioxide: We irradiate pure CO_2 ices at 25-65 K for fluences of $\sim 1 \times 10^{18}$ photons cm^{-2}. Figure 6.3.1 shows example spectra of the CO_2 ν_3 mode during photo-irradiation at 25 K, as well as the first-order kinetic fits to the CO_2 destruction rates at different temperatures and the associated photodestruction cross sections. The CO_2 loss rate doesn't deviate substantially from first-order kinetics during the photolysis period i.e the first-order kinetics fit has a similar slope at low and high fluences. During the irradiation of pure CO_2 ices, CO appears at 2141 cm^{-1} and continues to grow during the irradiation period. Martín-Doménech et al. [142] found that the CO column density reaches a maximum and then decreases at larger fluences; however, in their experiments the maximum CO column density was reached after $\sim 7 \times 10^{17}$ photons cm^{-2} i.e. at larger fluences than our experiments. Carbon trioxide (CO_3) is observed at 2044 cm^{-1} and reaches a maximum abundance at low fluence ($\sim 1.5 \times 10^{17}$ photons cm^{-2}) after which its abundance decreases for the remainder of the photolysis period. We also observe a small peak at 1040 cm^{-1} attributed to ozone. We find that 20-25% of the CO_2 ice is consumed during the irradiation period. The amount of CO produced in the pure CO_2 ice after a fluence of $\sim 7 \times 10^{17}$ photons cm^{-2} is 17% of the initial CO_2 ice column density, around half of the 40% value reported by Martín-Doménech et al. [142] for CO_2 ice at 8 K after a fluence 3×10^{18} photons cm^{-2} (a factor of 4 larger fluence). This corresponds to 74% of the carbon from CO_2 locked up in CO. Using the band strength for CO_3 estimated by Martín-Doménech et al. [142], CO_3 constitutes 13% of the carbon-budget, leaving another 13% unaccounted for. The unaccounted for carbon may be a result of photodesorption or due to the large uncertainty on the CO_3 band strength, it is not expected that a significant portion of other carbon bearing species are produced.

Carbon dioxide has the lowest VUV absorption of the solid species we have measured, with an

Table 6.3.1 (cont'd)

Ice	Lamp configuration	T_{ice} (K)	Ice thickness (ML)*	Photodestruction σ (cm^2)	Quantum yield
H_2O	H_2/Ar 10%	120	60	1.8×10^{-19}	0.04
H_2O/Ar	H_2/D_2	20	25	1.6×10^{-18}	0.94
CH_3OH	H_2/Ar 10%	25	127	8.9×10^{-19}	0.13
	H_2/Ar 10%	25	77	1.2×10^{-18}	0.18
	H_2/Ar 10%	55	76	1.4×10^{-18}	0.21
	H_2/Ar 10%	80	69	2.1×10^{-18}	0.31
	H_2/Ar 10%	100	67	3.2×10^{-18}	0.48
$^{13}CH_3OH$	H_2/D_2 MgF_2	25	96	1.0×10^{-18}	0.31
	H_2/D_2 sapphire	25	80	5.3×10^{-19}	0.13

*ML refers to equivalent monolayer = 10^{15} molecules cm^{-2}

[a] Upper limit

effective absorption cross section of 1×10^{-18} cm^2 for the Ly-α dominated H_2/Ar lamp and an estimated value of 4.9×10^{-19} cm^2 for the H_2/D_2 lamp. Figure 6.2.2 shows that CO_2 ices 300 ML thick absorb only 25% of the incident photons from the H_2/Ar lamp. Using the effective absorption cross section and the lamp flux we find that $\sim 8 \times 10^{-5}$ photons are absorbed per CO_2 per second. To assess the affects of changing ice opacity, we irradiate CO_2 ice films between 60 and 135 ML thick, the results of these measurements are shown in Table 6.3.1. We find that the photodestruction cross sections are the same, within error, for both of the ice thicknesses. The CO_2 films 60 and 135 ML thick absorb 6% and 13% of the incident photons, respectively.

We measured the temperature dependence of CO_2 ice photodestruction by irradiating ices deposited at 25, 40, 55 and 65 K. The results of the measurements for different ice temperatures are shown in Table 6.3.1 and Figure 6.3.1. We find the cross sections for CO_2 photodestruction are 4.1, 4.1, 3.8 and 4.0×10^{-19} cm^2 for ices at 25, 40, 55 and 65 K respectively. These values are statistically identical and therefore indicate that the CO_2 photodestruction rate is independent of the ice temperature.

The normalized integrated absorbance of CO (CO[t]/CO_2[i]) produced after a fluence of $\sim 3 \times 10^{17}$ photons cm^{-2} is 0.08, 0.09 and 0.1 for 55, 40 and 25 K respectively, indicating that much of the photoproduced CO is trapped in the CO_2 ice even above the CO-CO_2 desorption temperature reported in [47].

Methane: We irradiate pure CH_4 ices for fluences between 2-9×10^{17} photons cm^{-2} using both the H_2/Ar lamp and the H_2/D_2 lamp. We find that for pure CH_4 ice $\sim$40 ML thick and irradiated with the H_2/Ar lamp, $\sim$52% of the CH_4 column is consumed after a fluence of 9×10^{17} photons cm^{-2}. The dominant photoproduct formed is ethane (C_2H_6), observed by bands at 2976 cm^{-1}, 2942 cm^{-1}, 2882 cm^{-1} and 1463 cm^{-1} as described in previous experiments (e.g.

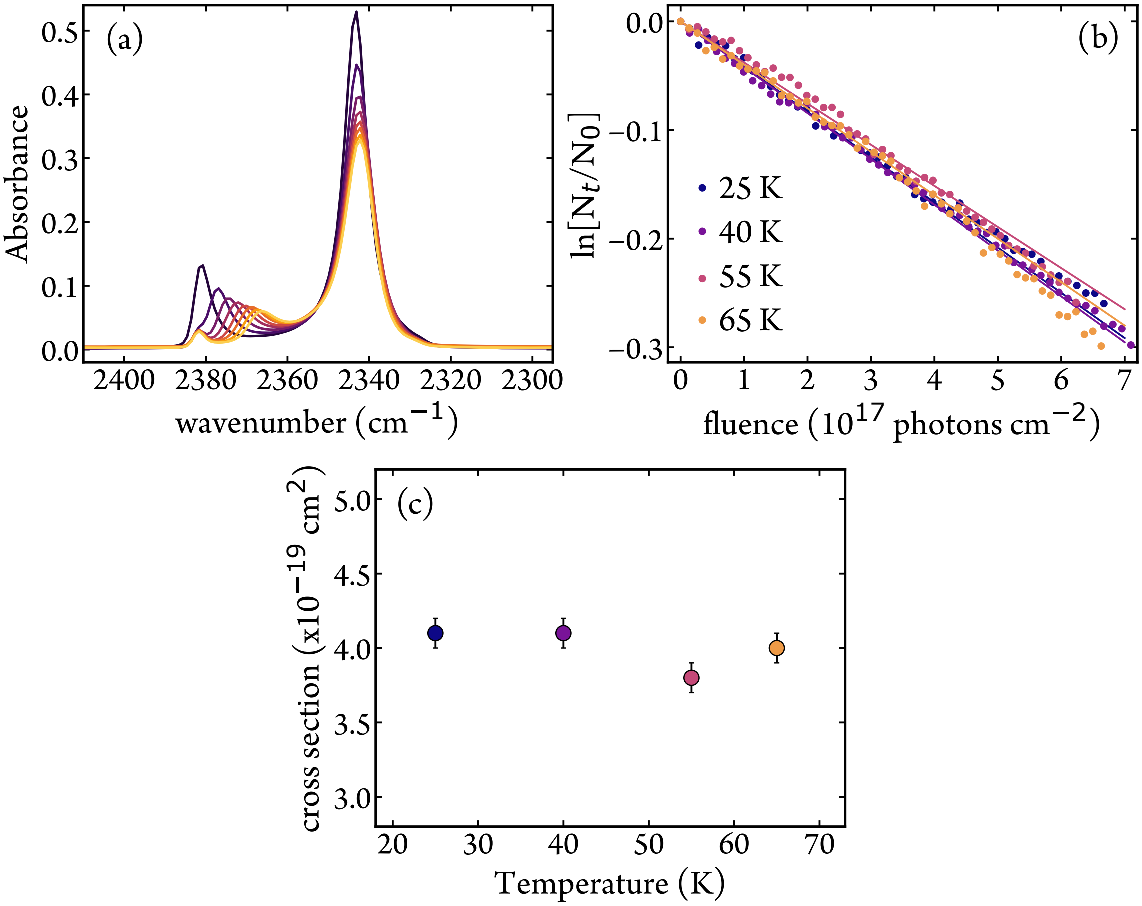

Figure 6.3.1: Photodestruction of CO_2 ices using the H_2/Ar Lyα dominated lamp. Panel (a) Example spectra showing the loss of the CO_2 ν_3 asymmetric stretching mode at ∼2343 cm^{-1} during CO_2 photoirradiation. Panel (b) Kinetic plots for the photodestruction of CO_2 ice at 25, 40, 55 and 65 K. The loss rate is fit assuming first order kinetics. Panel (c) Temperature dependence of the photodestruction cross sections for CO_2 ices at 25, 40 K, 55 and 65 K

Gerakines et al. [90], Öberg et al. [164]. We also observe the C-H symmetric and asymmetric stretching modes at 2960 cm^{-1} and 1460 cm^{-1} that may be due to other R-CH_3 bearing species. Ethylene (C_2H_4) is observed at 1437 cm^{-1} in the thick ice experiment (∼100 ML) but not in the thin ice experiments, probably due to S/N limitations.

Methane has a high absorption at Lyman-alpha and low absorption in the Lyman-band system with an absorption cross section ∼2-orders of magnitude lower at 160 nm than at Ly-α [50].

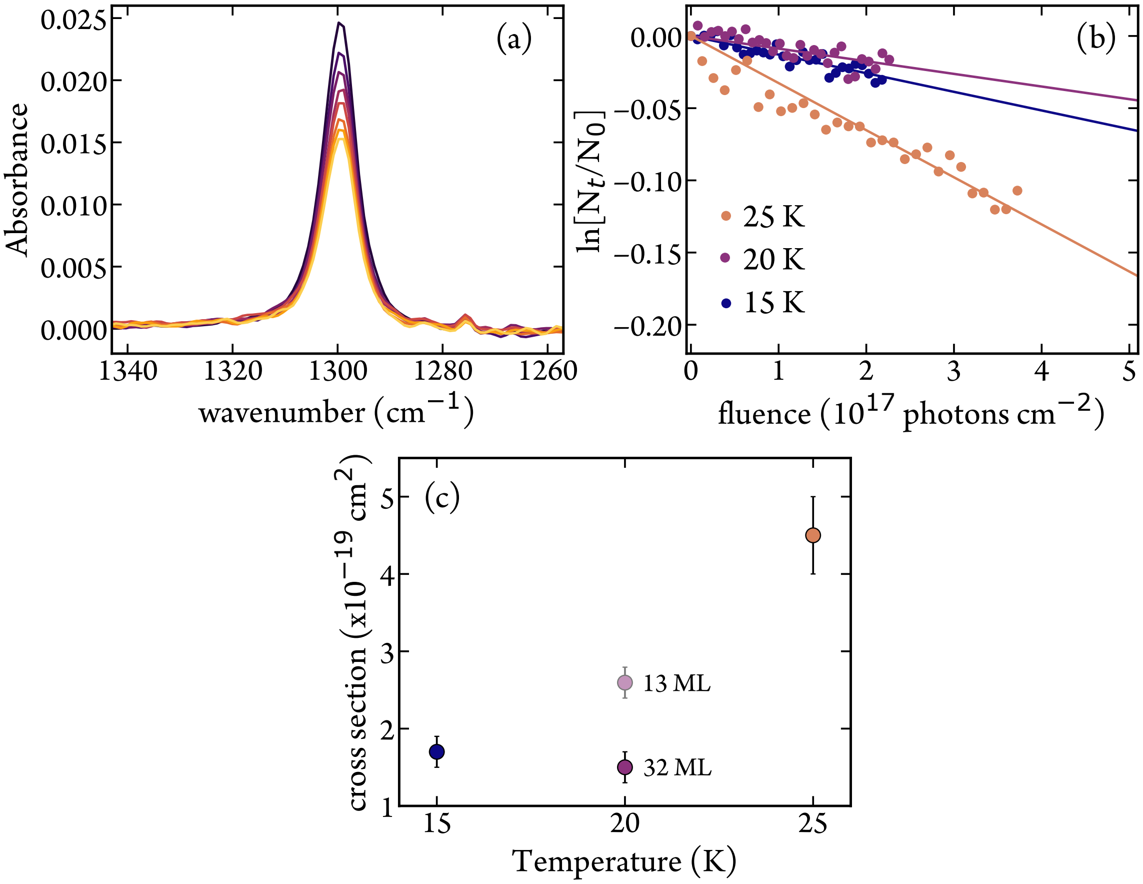

Figure 6.3.2: Photodestruction of methane ices using the H_2/D_2 lamp. Panel (a) Example spectra showing the loss of the methane bending mode at ∼1300 cm^{-1} during CH_4 photoirradiation. Panel (b) Kinetic plots for the photodestruction of methane ice at 15 20, 25 K. The initial linear range is fit assuming first order kinetics. Panel (c) Temperature dependence of the photodestruction cross sections for CH_4 ices at 15, 20 and 25 K. The two different measurements taken at 20 K are labelled with their thicknesses.

Figure 6.2.2 shows that by 300 ML almost all of the photons from the H_2/Ar lamp would be absorbed by the methane film. We measure the photodestruction cross sections for methane ices 34, 48 and 100 ML thick. The photodestruction cross sections are 9.2, 8.7 and 4.9 $\times 10^{-19}$ cm^2, for 34, 48 and 100 ML ices respectively. We find the the photodestruction cross sections decrease with increasing ice thickness, even within the nanometer regime. The percentage of photons absorbed by the films is 36%, 46% and 73%. For methane ices, roughly doubling the ice thickness from 48 ML to 100 ML results in ∼30% more photons absorbed, whereas for CO_2 ices a similar increase in ice thickness resulted in a ∼7% higher absorption.

Methane ices were photolyzed at 15, 20 and 25 K using the H_2/D_2 lamp. We are unable to study the temperature dependence under irradiation with the H_2/Ar (Ly-α dominated) lamp due to temperature limitations of the system. The cross section for photodestruction increases from 6.9×10^{-19} cm^2 at 15 K to 1.5×10^{-18} cm^2 at 25 K. Two measurements were made for methane ice of different thickness (13 ML and 32 ML) at 20 K. We found that the cross section for methane photodestruction was higher for the thin ice, 1.2×10^{-18} cm^2 compared to 6.3×10^{-19} cm^2, even though the optical depth does not change much between 13 and 32 ML for the H_2/D_2 (160 nm dominated) emission. We plan to repeat these experiments with systematic ice thickness variations to better constrain the effects of temperature on CH_4 photodestruction. At 15 K, the initially double peaked CH_4 band (indicative of the low temperature crystalline phase II) merges to form a single band during the irradiation. The single symmetric band is similar in shape and peak frequency to the spectra recorded CH_4 ice deposited above 20 K. The influence of this structural change on the ice photodestruction cross section is discussed further in section 6.5.

Water: Figure 6.3.3 shows spectra of the O-H stretching mode during the photo-irradiation of the water ice films under different conditions. Increasing fluence is indicated by the colour of the spectra and is shown in the scale bar. We irradiated water ices deposited at 25 K and monitored their IR spectra (panel (a)). During the photoirradiation, the initially broad O-H stretching band sharpens and redshifts, consistent with increased order in the water ice lattice. When the ice is instead annealed to 120 K and irradiated at 25 K (panel (b)) we see the opposite effect: the initially sharp O-H stretching mode is broadened, indicating amorphization. Because the IR band strengths for water ice depend strongly on the ice crystallinity, quantitative analysis of the ice photodestruction is difficult. In order to circumvent this issue, we photolyze a water ice both

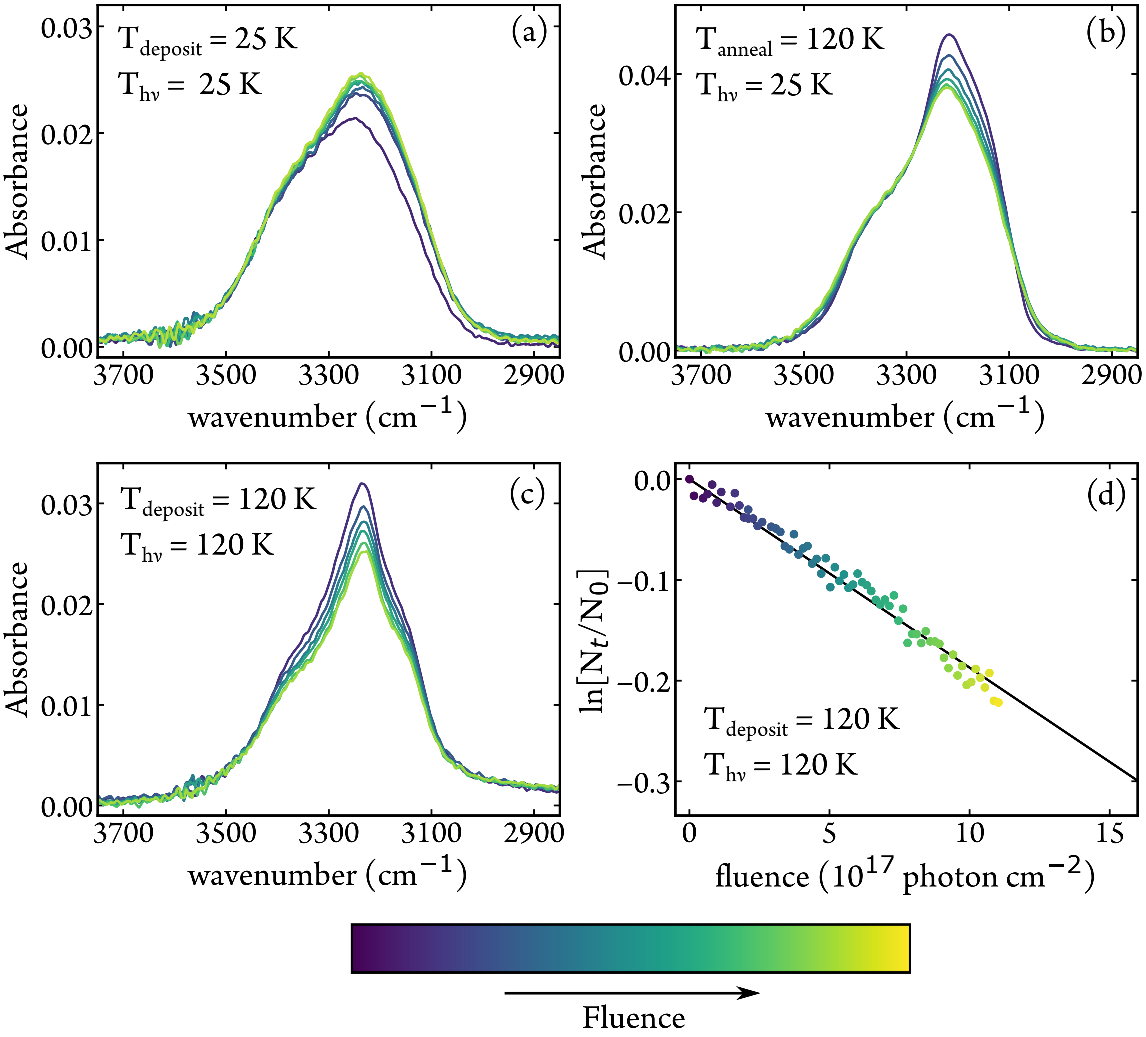

Figure 6.3.3: Spectra showing the evolution of the OH-stretching mode for water ices during photoirradiation. Panel (a) shows water ice both deposited and irradiated at 25 K. Panel (b) shows the OH-stretch of water ice deposited at 25 K, annealed to 120 K and irradiated at 25 K. Panel (c) shows the OH stretch of H_2O ice both deposited and irradiated at 120 K. Panel (d) shows the first-order kinetic plot for the loss of the H_2O ice at 120 K.

deposited and irradiated at 120 K. At this temperature water is sufficiently mobile such that the structure is maintained during the photon irradiation, as indicated by the band shape of the O-H stretching mode in panel (c). Panel (d) shows the first-order kinetic fit to the loss of H_2O ice at 120 K. We find a cross section for H_2O photodestruction at 120 K is 1.8×10^{-19} cm^2. This gives a

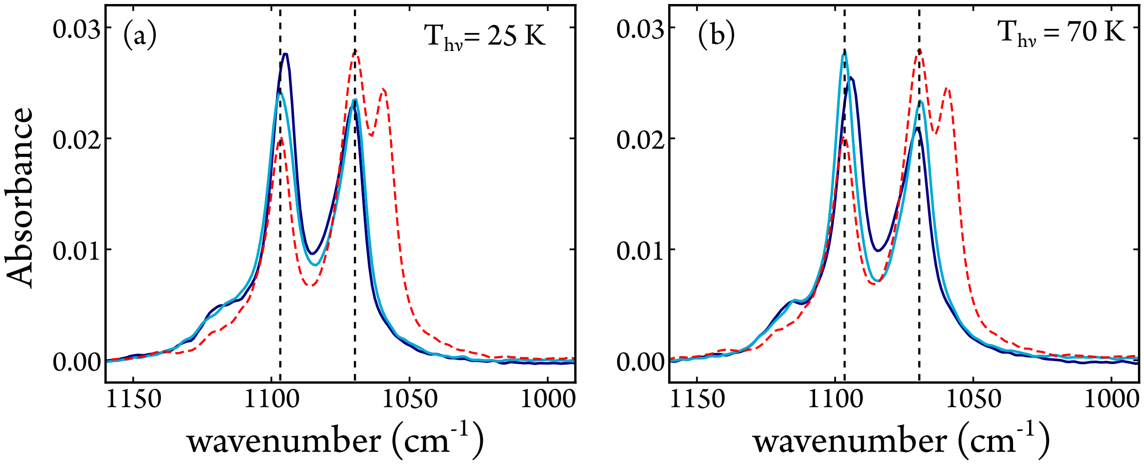

Figure 6.3.4: Low fluence changes in the umbrella mode of NH_3 ices annealed to 70 K and irradiated at 25 K (a) or 70 K (b). The spectra taken before photolysis are shown in dark blue and the spectra after a fluence of ∼1×10^{16} photons cm^2 are shown in light blue. In both cases the peaks shift toward the frequency of the NH_3 ice deposited at 70 K (red dashed line).

quantum yield for water ice destruction of 0.04, lower than the gas-phase value of ∼1, possibly indicating a strong cage effect. We therefore expect that the photodestruction cross section would decrease with temperature, implying that the efficiency of producing OH at low temperature is likely lower than currently assumed.

Ammonia: We irradiated NH_3 ices of different thicknesses and at temperatures of 25, 40, 55 and 70 K, for fluences of ∼1×10^{17} photons cm^{-2}. We monitor the loss the NH_3 umbrella mode at 1070 cm^{-1} during the irradiation.

Ammonia ice has an effective absorption cross section at the emission wavelengths of the H_2/Ar lamp of 8.7×10^{-19} cm^2. We found a photodestruction cross section for annealed ammonia ice at 25 K of 3.3×10^{-20} cm^2 for an ice thickness of 87 ML. The 87 ML ice would absorb ∼53% of the incident photons from the H_2/Ar lamp. Increasing the ice thickness to 187 ML we found a negligible loss of NH_3 ice such that we were unable to fit the decay kinetics. The analysis is further complicated by changes in the ice structure that also appear to be thickness dependent i.e. the crystallization rate may increase with ice thickness. We place an upper limit on the photodestruction cross section of $\sim 1\times 10^{-20}$ cm^2.

We find that for NH_3 ices thicker $\sim$50 ML the initially broad N-H stretching and umbrella modes sharpen, split into two peaks, and the integrated band areas increase during the photo-irradiation, possibly masking the effect of loss of NH_3 due to photodestruction. For NH_3 ice around 20 ML thick, the IR band shape does not sharpen and therefore the cross section derived from the IR band loss is larger. Because of the low S/N on the thin ices, we photolyze NH_3 ices annealed to 70 K and subsequently cooled to 25, 40, 55 or 70 K. Figure 6.3.5 panel (a) shows an example of spectra taken during the photoirradiation of NH_3 ice annealed to 70 K and cooled to 25 K. In the first IR spectrum taken (after a fluence of $\sim 1\times 10^{16}$ photons cm^2) we see a rapid change in in the IR absorbance. We show these low fluence spectral changes in Figure 6.3.4. For annealed NH_3 ices photolyzed both at 25 K and 70 K, the peak frequencies shift toward those of a crystalline NH_3 ice deposited at 70 K. After this initial rapid change in the NH_3 spectrum, the loss of NH_3 follows first-order kinetics. The origin of the dramatic spectral change at low fluence is unclear, though it it likely associated with ice structural changes induced by the photo-irradiation. We find that the photodestruction cross sections increase with temperature with values of 0.33, 0.72, 1.1 and 1.5 $\times 10^{-19}$ cm^2 for 25, 40, 55 and 70 K respectively.

Methanol: we photolyze a series of methanol ices of different thicknesses and at temperatures of 25, 55, 80 and 100 K. The main photo-products we observe are CO, CO_2, H_2CO and CH_4 as well as peaks associated with ethanol, dimethyl ether and other COMs similar to those reported in Öberg et al. [163]. The loss of CH_3OH deviates from first-order kinetics after fluences of $\sim 1\times 10^{17}$ photons cm^{-2} so we derive the photodestruction cross sections from the initial rate at low fluences. The deviation is likely due to higher-order alcohols that absorb at the same frequency as methanol. Methanol ice has an effective absorption cross sections at the emission

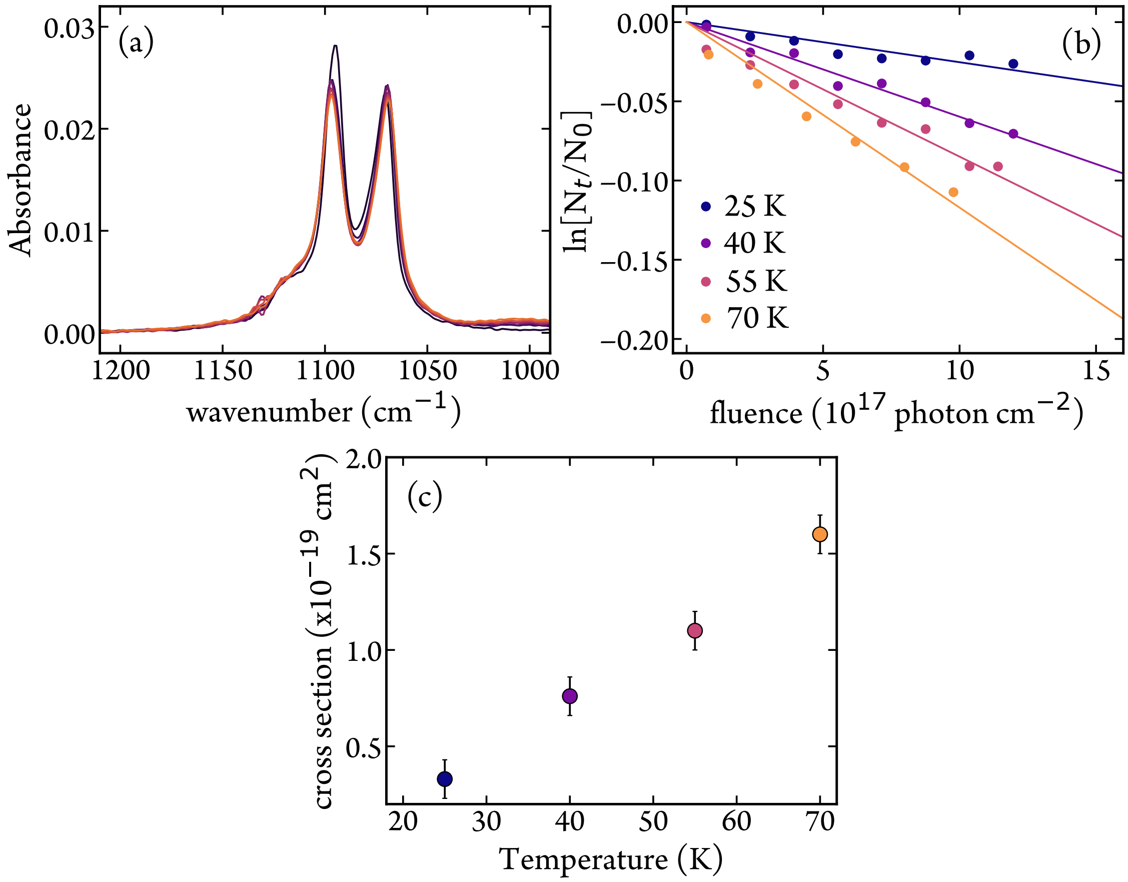

Figure 6.3.5: Photodestruction of annealed ammonia ices. Panel (a) Example spectra showing the loss of the ammonia umbrella mode at ~1070 cm^{-1} during NH$_3$ photoirradiation. Panel (b) Kinetic plots for the photodestruction of ammonia ice at 25, 40, 55 and 70 K. The data are binned and averaged every 13 minutes due to the low S/N. Panel (c) Temperature dependence of the photodestruction cross sections for NH$_3$ ices at 25, 40, 55 and 70 K.

wavelengths of the H$_2$/Ar lamp of $\sigma_{eff} = 8.4\times 10^{-19}$ cm^2. We photolyzed methanol ices 77 and 127 ML thick and find that the photodestruction cross sections increase with decreasing ice thickness from 8.9 to 12$\times$10^{-19} cm^2. The ices absorb 45% and 66% of the incident VUV photons respectively i.e. an increase of ~20%. Figure 6.3.6 shows the kinetics of photodestruction of methanol ices at 25, 5, 80 and 100 K. Example spectra of the methanol C-O band during photo-irradiation of methanol ice at 25 K are shown in panel (a). We find that at 25 K ~20% of

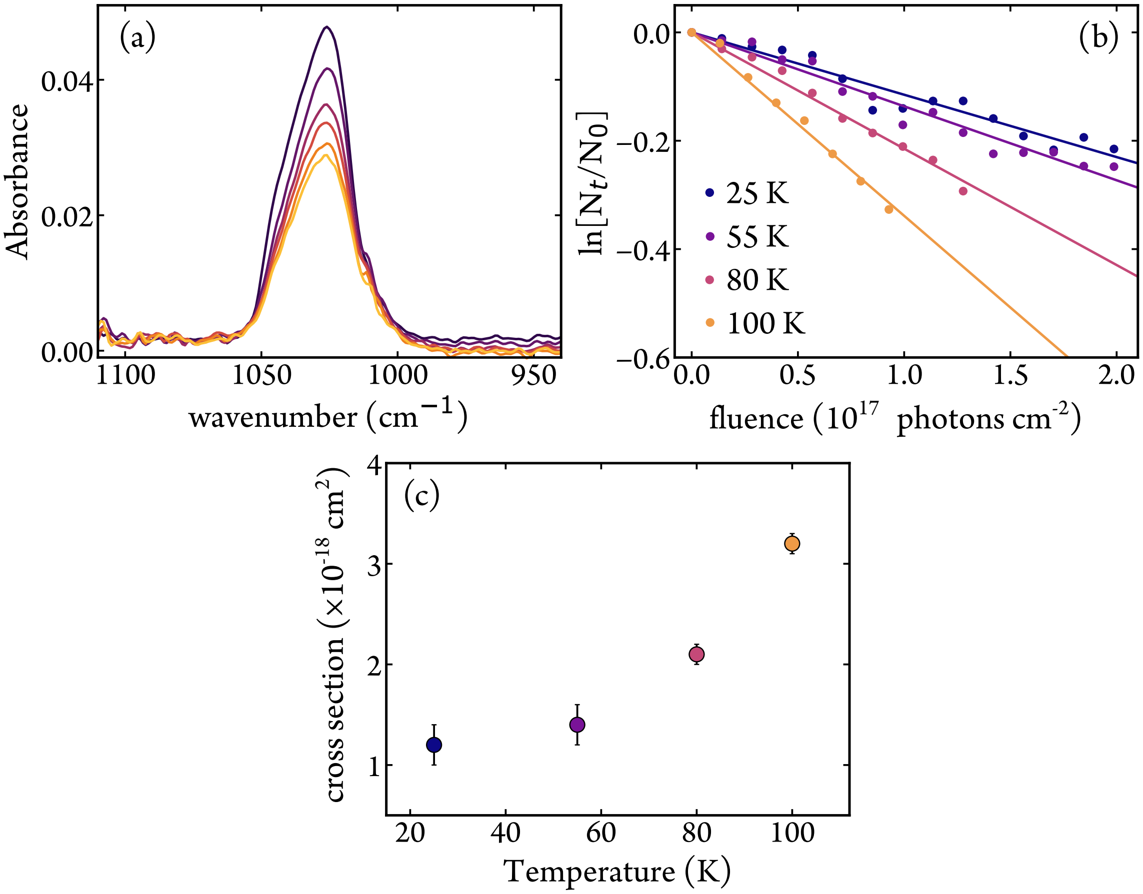

Figure 6.3.6: Photodestruction of methanol ices. Panel (a) Example spectra showing the loss of the methanol C-O stretching mode at ~1030 cm^{-1} during CH_3OH photoirradiation. Panel (b) Kinetic plots for the photodestruction of methanol ice at 25, 55, 80 and 100 K. The initial linear range is fit assuming first order kinetics. Panel (c) Temperature dependence of the photodestruction cross sections for CH_3OH ices at 25, 55 K, 80 K and 100 K.

the ice is lost after a fluence of 2×10^{17} photons cm^{-2}. We fit the initial loss of the methanol band at low fluences to derive the photodestruction cross sections. This is below $\sim2\times10^{17}$ photons cm^{-2} for CH_3OH ices at 25 and 55 K, and below 1.5×10^{-17} photons cm^{-2} for the 80 and 100 K ices. The cross sections increase with ice temperature with values of 1.2, 1.4, 2.1 and 3.2 $\times10^{-18}$ cm^2 for 25, 55, 80 and 100 K methanol ices, respectively.

Table 6.3.2. Initial ice thicknesses for the binary ice mixtures co-deposited at 25 K. The percentage of incident photons absorbed by each species is estimated using the effective absorption cross sections for the pure ices.

Ice 1	Ice 2	Thickness Ice 1 (ML)	Thickness Ice 2 (ML)	% Incident Photons Abs Ice1/Ice2
CO_2[a]	H_2O	64	205	6/63
CO_2	CH_4	39	30	4/32
CO_2	CH_3OH	72	48	7/33
CO_2	NH_3	60	25	6/20
CO_2	CO	38	20	4/0.6
CO_2	Xe	27	~240[b]	3/0
CH_4	H_2O	45	40	44/17
CH_4	CH_3OH	30	76	32/47
CH_4	NH_3	48	63	46/42
CH_3OH	H_2O	69	25	44/11
CH_3OH	CO	53	10	36/0.3
CH_3OH	Xe	71	~270[b]	45/0
NH_3	H_2O	98	~50[b]	57/21
NH_3	CO	105	8	60/0.2
NH_3	Xe	106	~500[b]	60/0

[a] Isotopic $^{13}CO_2$ was used

[b] Estimated from the gas-phase mixing ratio

6.3.2 ICE MIXTURES

We photolyze CO_2, CH_4, NH_3 and CH_3OH in various co-deposited binary ice mixtures in order to study trends in the effective photodestruction cross sections with different reactive and diffusive environments. The photodestruction cross sections are calculated in the same way as for the pure ices, that is, by fitting first-order kinetics to the normalized loss of the individual ice

Table 6.3.3. Effective photodestruction cross sections for binary ice mixtures irradiated with the H_2/Ar (Ly-α dominated) lamp at 25 K, in units of 10^{-19} cm^2. The photodestruction cross sections are calculated for the molecule in the left-most column in an ice mixture with the molecule in the top row. The pure ices are shown in italics for comparison.

	CO_2	H_2O	CH_4	CH_3OH	NH_3	CO[a]	Rare-gas
CO_2	*4.1*	1.8	6.2	5.2	9.2	4.0	9.5
CH_4	17	14	*9.2*	12	5.7	—	—
CH_3OH	8.4	12	16	*12*	—	12	16
NH_3	4.8	1.3	0.8	—	*0.33*[*]	0.6	3.0

[*] The pure NH_3 ice is annealed to 70 K before photolysis at 25 K

[a] Pure CO was not studied due to temperature limitations of the system

column densities. This means that the effective photodestruction cross sections now include reactions between photoproducts in the binary ice mixtures that can reform the molecule (giving a lower net loss) or form other species (increasing the net loss). The binary ice mixtures also change the diffusion environment as compared to the pure ice, especially in strong hydrogen-bonding matrices. This can alter the rates of diffusion of newly formed radicals, as well as changing the energy dissipation rates and the cage barriers.

The ice column densities and mixing ratios used are presented in Table 6.3.2 along with the percentage of the incident photon flux absorbed by the ice components according the their absorption cross sections listed in Table 6.2.2. Figures6.3.7–6.3.9 and Table 6.3.3 show the effective photodestruction cross sections obtained for the binary ice mixtures.

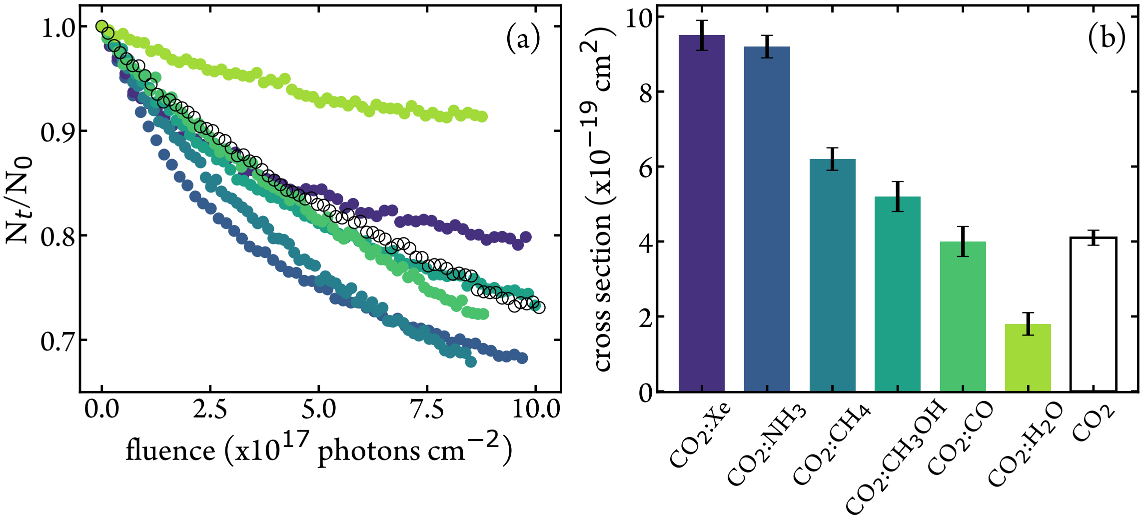

Figure 6.3.7: Photodestruction of CO_2 in various binary ice mixtures. Panel (a) shows the kinetic curves for the normalized loss of CO_2 in different ice mixtures as a function of photon fluence. Panel (b) shows the photodestruction cross sections for CO_2 in the binary ice mixtures compared to pure CO_2 ice at 25 K.

CO_2 ICE MIXTURES:

CO_2 ices were photolyzed in binary ice mixtures with Xe, CO, H_2O, CH_4, NH_3 and CH_3OH. Figure 6.3.7 shows the photodestruction kinetics along with the photodestruction cross sections for CO_2 in binary ice mixtures at 25 K compared to pure CO_2 ice at 25 K. The pure CO_2 ice is denoted by the black open circles and bar. The net photodestruction cross section for CO_2 ranges from 1.8×10^{-19} cm^2 for CO_2 in a water ice mixture to 9.5×10^{-19} cm^2 for CO_2 mixed with Xe. Below we describe the effects of mixing CO_2 with the various ices both qualitatively and in terms of changes in the net photodestruction cross section.

CO_2/H_2O: We conducted initial experiments in which we mixed CO_2 with H_2O ice in ratios of 1:20, 1:5 and 2:1. We saw zero net loss of CO_2 in the dilute 1:20 $^{12}CO_2$:H_2O mixture, probably due to a combination of band shape changes, CO_2 deposition from the chamber background pressure and the production of CO_2 via surface OH and background CO(g) as described in Yuan et al. [236]. To minimize the latter two effects, we irradiate mixtures of isotopically labelled $^{13}CO_2$ and H_2O. Figure 6.3.1 shows the loss of $^{13}CO_2$ ice initially 64 ML thick mixed with 205 ML of water. We find the cross section for photodestruction of CO_2 in H_2O ice mixtures is decreased with respect to pure CO_2 ices from 4.1 to 1.8×10^{-19} cm^2.

In the 2:1 mixture, similar to pure CO_2 ice, we see new bands from CO and CO_3 During the irradiation period we see a band appear around 1718 cm^{-1}, convoluted with the H_2O OH bending mode, attributed to the formation of H_2CO. The OH dangling bonds are depleted during the irradiation and we observe a dramatic spectral change in the CO_2 band profile. The initially broadened and redshifted CO_2 ν_3 mode centered around 2332 cm^{-1} blueshifts to 2341 cm^{-1} during the irradiation i.e. towards the frequency of pure and crystalline CO_2 ice.

In the dilute 1:5 and 1:20 mixtures we do not see any new photoproducts including CO and CO_3. This could be due to a strong cage effect, in which excited CO + O cannot leave the CO_2-H_2O cage, or could be due to shielding of the CO_2 molecules from UV-photons due to the strong H_2O absorption at Lyman-alpha. Another possibility is that the photoproduced CO molecules are quickly removed reactions in the ice e.g. by CO + OH. We discuss this further in 6.5.

CO_2/CH_4: The photodestruction of CO_2 in a methane ice mixture 39:30 ML thick is shown in 6.3.7. The cross section for CO_2 destruction in a methane binary ice mixture is increased with respect to pure CO_2 from 4.1×10^{-19} to 6.2×10^{-19} cm^2. Spectral changes during the irradiation indicate that the increase in the photodestruction cross section is likely due to chemistry between the photoproducts of CO_2 and CH_4. Recently, Bergner et al. showed that O(^{1}D) atoms, produced by *in situ* photodestruction of O_2/CH_4 mixtures, can insert into methane ice forming methanol. We do not observe the formation of methanol, possibly due to low S/N or because of the higher photodestruction of CH_4 at Lyα compared to the LBS emission used by Bergner et al. We see spectral evidence for the formation of formaldehyde around $\sim$1720 cm^{-1}. The formaldehyde peak is redshifted in isotopic experiments using $^{13}CH_4$:$^{12}CO_2$ and we see a peak corresponding to the formation of ^{13}CO, indicating that the carbon from mehane is incorporated into oxygen-bearing species. This is consistent with an increased net photodestruction cross section for both CH_4 and CO_2 in the CO_2:CH_4 ice mixture compared to the pure ices.

CO_2/CH_3OH: The photodestruction of CO_2 in methanol 72 ML: 48 ML thick is increased with respect to pure CO_2 ice from 4.1×10^{-19} cm^2 to 5.2×10^{-19} cm^2. The increase may be smaller than for other binary mixtures due to the reformation of CO_2 via the reaction of the first generation photoproducts (e.g. CO + OH) similar to CO_2 in binary mixtures with water ices. Another possibility is that the increase in the cage barrier may also be larger than for mixtures with CH_4 and NH_3 ices. The relative importance of these two effects could be studied by isotopically labelling the O of methanol to follow the kinetics of CO_2 reformation and is a topic for future study.

CO_2/NH_3: In the 60 ML:25 ML CO_2:NH_3 ice mixtures we find that the cross section for CO_2 ice destruction is increased from 4.1×10^{-19} to 9.2×10^{-19} cm^2. A Large number of new photoproducts are observed in the spectra during irradiation, particularly in the N-H, C=O and N=O region between 1770-1200 cm^{-1} and the N-H/O-H region between $\sim$3500–2500 cm^{-1}, consistent with a increase in the net photodestruction CO_2 rate due to chemistry - either by direct reaction with CO_2, or by reactions involving CO and O, therefore reducing the amount of CO_2 that can be reformed. The spectral results are reported further in section 6.3.2 regarding the NH_3 ice mixtures.

CO_2:CO We mix CO_2 with CO with thicknesses of 38 ML and 20 ML respectively. We find that the photodestruction cross section for CO_2 in a CO_2:CO ice mixture is statistically the same as that of pure CO_2 ice, with cross sections of 4.0×10^{-19} cm^2 and 4.1×10^{-19} cm^2, respectively. We also mix CO_2 with $C^{18}O$ to check how much of the isotopically labelled oxygen is incorporated into newly formed CO_2 molecules and how this affects the net photodestruction cross section for $^{12}CO_2$. We find that the loss of $^{12}CO_2$ is increased and some of the 12-C is incorporated into $C^{16}O^{18}O$ and $C^{18}O_2$. The photodestruction cross section for the sum of all CO_2 isotopes is 3.7×10^{-19} cm^2, while for $^{12}CO_2$ it is 6.0×10^{-19} cm^2, i.e. moving closer to the gas-phase quantum yield of $\sim$1.

CO_2/Xe: CO_2 is photolyzed in a $\sim$1:9 xenon ice mixture in order to study the importance of the cage effect. In the xenon ice, CO_2 molecules are (at least partially) isolated from one another and surrounded instead by xenon atoms which have low van der Waals interactions with CO_2. The weaker CO_2-Xe interactions should reduce the cage barrier and relaxation probability compared to pure CO_2 ice. We see an increase in the photodestruction cross section with respect to pure CO_2 ice giving a value of 9.5×10^{-19} cm^2 i.e. a quantum yield of 0.95 based on the effective absorption cross section in Table 6.2.2, similar to the gas-phase value of $\sim$1 at Lyman-alpha.

METHANE ICE MIXTURES:

The photodestruction of methane ice was studied in binary ice mixtures of CO_2, H_2O, CH_3OH and NH_3. The kinetics of the CH_2 loss and the cross sections derived for the binary ice mixtures are shown in Figure 6.3.8. We found that, except in the case of NH_3 ice mixtures, the CH_4 photodestruction cross section is increased with respect to pure CH_4 ice. The highest photodestruction cross section was obtained in the binary mixture with CO_2.

CH_4/H_2O: The photodestruction of CH_4 in a 45 ML:40 ML CH_4:H_2O binary ice mixture is increased with respect to pure CH_4. We find a photodestruction cross section of 1.4×10^{-18} cm^2 compare to 9.2×10^{-19} cm^2 for pure CH_4 ice 34 ML thick. The increase in the photodestruction cross section is likely due to reactions between photoproducts decreasing the net reformation of CH_4. The major photoproducts we observe are C_2H_6, C_2H_4, H_2CO and CO_2. Öberg et al. [164] reported the formation of alcohols during the irradiation of CH_4/H_2O mixtures and it is likely

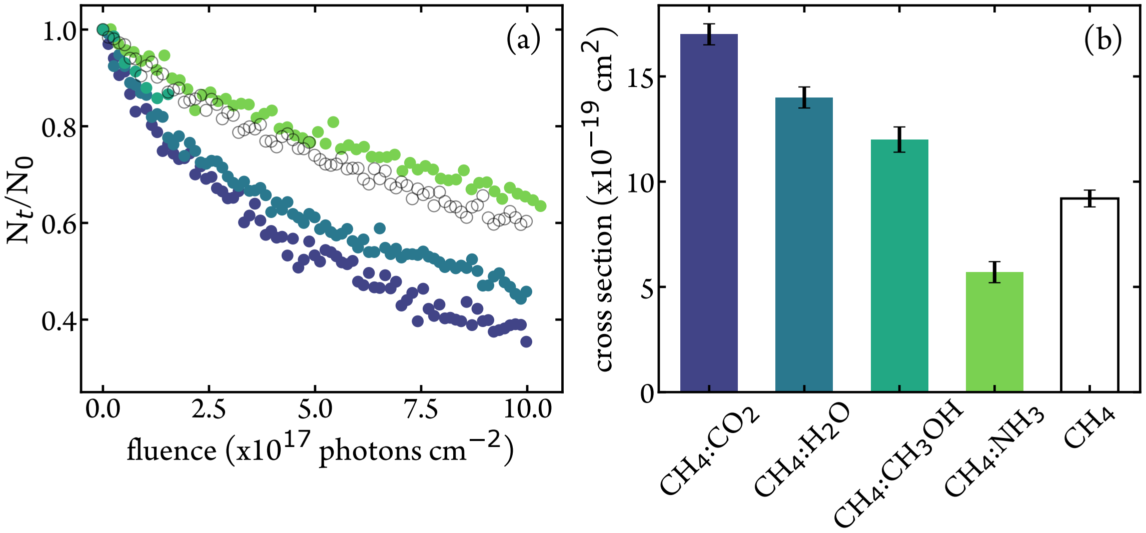

Figure 6.3.8: Photodestruction of CH_4 in various binary ice mixtures. Panel (a) shows the kinetic curves for the normalized loss of methane in different ice mixtures as a function of photon fluence. Panel (b) shows the photodestruction cross sections for methane in the binary ice mixtures compared to pure methane ice at 25 K.

that these are also formed but the low S/N prohibits their identification.

CH_4/CH_3OH: The photodestruction of CH_4 in a methanol binary ice mixture is increased with respect to pure CH_4 ice. We find a photodestruction cross section of 1.2×10^{-18} cm^2 for 30 ML of CH_4 mixed with 76 ML CH_3OH. We observe the production of a range of products in the IR spectra during the photolysis including CO_2, CO, H_2CO, CH_3CH_2OH and CH_3OCH_3.

CH_4/NH_3: In contrast to the other ice mixtures, we find that the CH_4 photodestruction cross section in the 48 ML:63 ML CH_4:NH_3 binary ice is decreased. This could be due to an increased cage barrier felt by CH_4 in the CH_4:NH_3 ice mixture, due to the van der Waals forces between CH_4 and NH_3 molecules. The increased optical depth may also affect the net photodestruction cross section, as seen for pure methane ices. The spectra do not show substantial changes during the irradiation as compared to the pure ices, except for a small peak associated with the formation of HCN.

CH_4/CO_2: The photodestruction of CH_4 in a CO_2 ice mixture 39:30 ML thick is increased

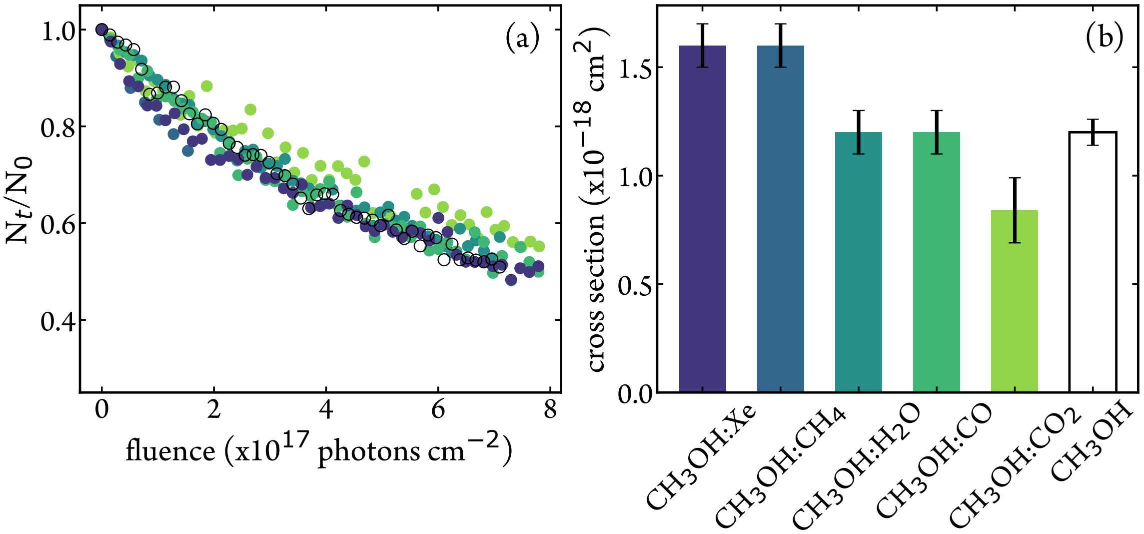

Figure 6.3.9: Photodestruction of CH_3OH in various binary ice mixtures. Panel (a) shows the kinetic curves for the normalized loss of CH_3OH in different ice mixtures as a function of photon fluence. Panel (b) shows the photodestruction cross sections for CH_3OH in the binary ice mixtures compared to pure CH_3OH ice at 25 K.

with respect to pure CH_4 ice of similar thickness. See the CO_2/CH_4 ice section (6.3.2) above for a description of the spectral changes during photoirradiation of the CH_4/CO_2 ice mixture.

CH_3OH ICE MIXTURES:

Figure 6.3.9 shows the photodestruction kinetics for various binary ice mixtures with CH_3OH. We find that the photodestruction rate of methanol is not strongly influenced by the addition of other ice species. The photodestruction cross section is increased with respect to pure methanol in a xenon matrix and in the methane binary ice mixture. The photodestruction cross sections for methanol mixed with H_2O or CO ice are the same, within error, as the photodestruction of pure CH_3OH ices.

CH_3OH/H_2O: We photolyze an ice mixture with 69 ML of methanol and 25 ML of water. We find that the cross section for photodestruction is statistically the same as for pure CH_3OH ice.

We also photolyze a more dilute mixture of CH_3OH in H_2O (34 ML:230 ML) and also find a photodestruction cross section of 1.2×10^{-18} cm^2. This suggests the photoproduced OH from the dissociation of water ice is not involved in reformation of CH_3OH at short timescales. This is possibly due to the much lower photodestruction cross section for water ice as compared to CH_3OH but full kinetic modelling and isotopic experiments would be required to validate this hypothesis.

CH_3OH/CO: Methanol was photolyzed in an ice mixture of 53 ML of CH_3OH and 10 ML of CO. Similar to the case of water, we found that the photodestruction cross section for methanol in the CH_3OH:CO mixture is the same as for pure CH_3OH. Using isotopically labelled $C^{18}O$ we find that most of the ^{18}O ends up in CO_2. We plan to photolyze 1:1 mixtures of methanol with CO to determine if the methanol photodestruction cross section remains unchanged by the presence of CO.

CH_3OH/CH_4: We photolyze an ice mixture with 76 ML CH_3OH and 30 ML CH_4. The photodestruction cross section for methanol ice is increased with respect to the pure CH_3OH ice at 25 K, from 1.2 to 1.6×10^{-19} cm^2. A qualitative description of the spectral changes can be found above in section 6.3.2.

CH_3OH/CO_2: The photodestruction cross section for CH_3OH in CO_2 is slightly decreased. The CO_2 photodestruction cross section, however, is increased (see section 6.3.2). The methanol cross section may be decreased in the CO_2 ice if a chemical route involving CO_2 photofragments reforms CH_3OH faster than reforming CO_2. This is discussed further in 6.5

CH_3OH/Xe: We find that the photodestruction cross section for methanol ice is larger in a ~1:4 CH_3OH:Xe mixture than in pure CH_3OH ice increasing to around $\sim1.6\times10^{-18}$ cm^2. This is still a low quantum yield of 0.24 compared to the gas-phase value of ~1.

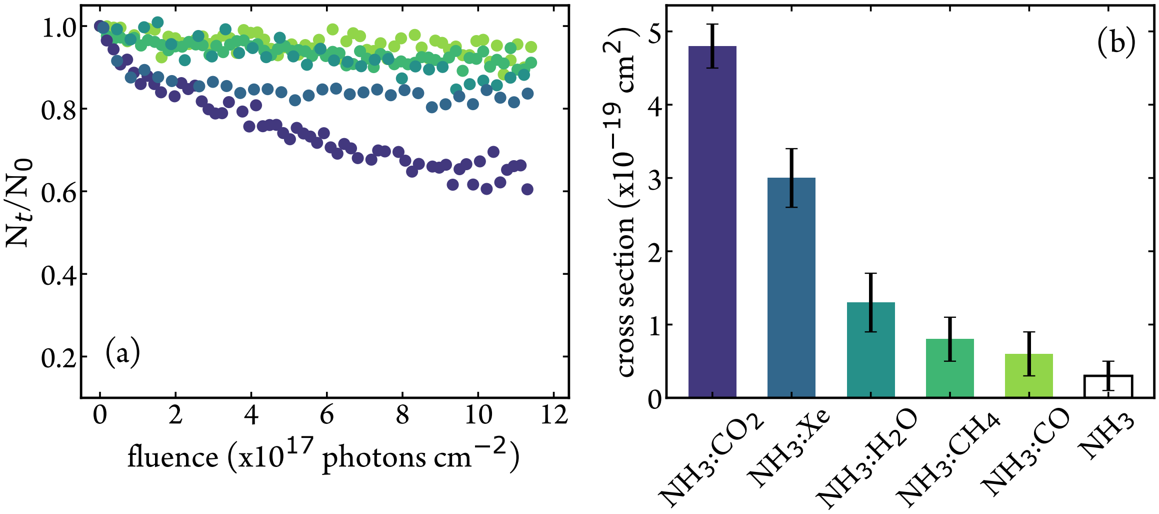

Figure 6.3.10: Photodestruction of NH_3 in various binary ice mixtures. Panel (a) shows the kinetic curves for the normalized loss of NH_3 in different ice mixtures as a function of photon fluence. Panel (b) shows the photodestruction cross sections for NH_3 in the binary ice mixtures compared to pure NH_3 ice at 25 K.

AMMONIA ICE MIXTURES:

Figure 6.3.10 shows the photodestruction kinetics for ammonia ices in various binary mixtures. Ammonia was photolyzed in binary mixtures with Xe, CO_2, H_2O, CH_4 and CO. The photodestruction rate of NH_3 is increased for all binary ice species with respect to pure NH_3. It is important to note in the comparisons below that the pure NH_3 ice was annealed since the loss of amorphous NH_3 ice was below the S/N level in our spectra. The ice mixtures are not annealed so direct comparison with pure and annealed NH_3 ice should be considered accordingly.

NH_3/Xe: We find the the rate of photodestruction for NH_3 ice in a ∼1:5 Xenon matrix is increased relative to pure annealed NH_3 ice, with a photodestruction cross section of 3.0×10^{-19} cm^2. The higher photodestruction cross section in Xe is consistent with a decreased cage barrier allowing the newly formed photoproducts to react and form other species rather than reforming NH_3. Though the photodestruction cross section is initially increased, the destruction rate drops to near zero after a fluence of $\sim 5\times10^{17}$ photons cm^{-2}. It is possible that clusters form due to diffusion and recombination of NH_3 photoproducts, causing an increased cage effect in the clusters.

NH_3/CO: The photodestruction cross section for NH_3 in a 105 ML: 8 ML mixture of NH_3:CO is slightly increased compared to pure annealed NH_3 ice. Even with the small <1:10 ratio of CO in the ice we observed chemistry occurring that is likely responsible for the increased photodestrcution rate. We observed the formation of the cyanate ion, OCN^- at $\sim$2150 cm^{-1} and CO_2 as well as some features in the N-H/O-H stretching region.

NH_3/CH_4: The photodestruction of NH_3 in a 63 ML:48 ML NH_3:CH_4 ice mixture is increased relative to pure annealed NH_3. We find a photodestruction cross section of 8×10^{-20} cm^2. We do not observe any new reaction products that differ from the pure ices, except for a small amount of HCN. In addition, we did not find an increase in the CH_4 photodestruction rate in the ice mixture. The increase in the NH_3 photodestruction cross section may then be due to a decreased cage barrier and/or inhibited crystallization in the CH_4 ice which would also manifest as a larger decrease in the NH_3 IR bands.

NH_3/CO_2: In the 25 ML:60 ML CO_2:NH_3 ice mixture, ammonia is destroyed more rapidly than in pure NH_3 ice with an effective photodestruction cross section of 4.8×10^{-19} cm^2. We see a number of new bands forming early in the irradiation including those attributed to fingerprint modes from C=O, N=O, N-H and C-H bending. Bands attributed to the formation of hydroxylamine are observed. We also observe the OCN^{-1} ion, indicating acid base chemistry, probably involving HNCO.

NH_3/H_2O: We find an increase in the photodestruction rate of NH_3 ice in $\sim$98 ML:50 ML water ice mixture compared to pure annealed NH_3 ice. No new photoproducts are observed at our S/N level.

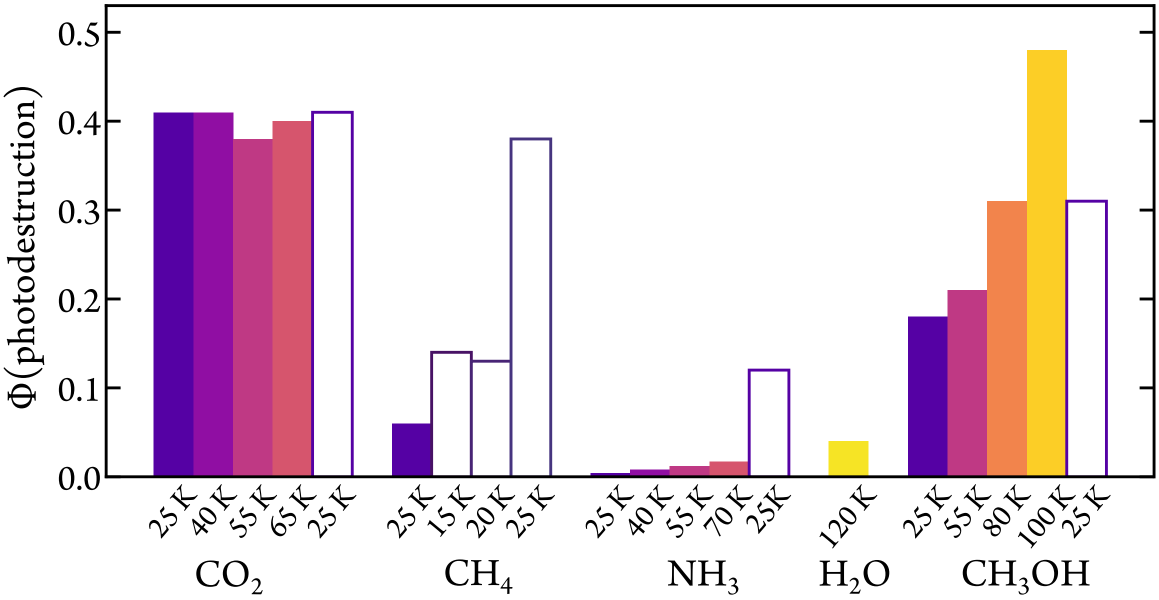

Figure 6.4.1: Summary of the photodestruction quantum efficiencies for the pure ices at different temperatures. The filled bars show the results obtained using the H_2/Ar (Ly-α) lamp while the open bars show those obtained with the H_2/D_2 lamp.

6.4 Dependence on Lamp Configuration

An eventual aim of this study is to use the different H_2 lamp configurations to compare the photodestruction cross sections for the different emission profiles: one with predominantly Lyman-alpha emission and the other with predominantly Lyman-band system emission, peaking at 160 nm. It is unknown for most ice species whether the quantum efficiencies for photodestruction are wavelength dependent in the VUV range applicable to interstellar UV-fields. Comparing cross sections from the two wavelength regimes can provide information about different absorption and excitation channels for photodestruction and help inform astrochemical models. Lyman-alpha is more strongly absorbed than 160 nm for all of the ices studied, therefore the ices absorb more photons/molecule with the H_2/Ar Lyα lamp then with the H_2/D_2 lamp. As mentioned previously, if the ice has substantial optical thickness, the first-order kinetic fit will underestimate the photodestruction cross section.

We find systematically higher quantum yields for the photodestruction of ices using the H_2/D_2 lamp than using the H_2/Ar lamp except for the case of CO_2 ice. It is unclear at this stage whether this is a true effect or due to uncertainties in the lamp fluxes and spectral emissions. We therefore make only relative comparisons between the ice species irradiated with the same lamp configuration.

The photodestruction cross sections for ices irradiated with H_2/D_2 lamp are calculated in the same way as for the H_2/Ar lamp i.e. using first-order kinetics fits to the normalized loss of the ice IR absorbance bands. We use the relevant effective absorption cross sections listed in Table 6.2.2 to calculated the quantum efficiencies. Using the sapphire window do not observe loss of CO_2 or methane during the irradiation period during the irradiation period, probably due to their low absorption cross sections a Lyman-band system wavelengths combined with the lower flux due to decreased transmission though the sapphire window. CO_2 and CH_4 absorb 2.3% and 1.4% of the photons emitted by the sapphire filtered H_2/D_2 lamp respectively, leading to $\sim 1 \times 10^{-5}$ absorbed photons molecule^{-1} s^{-1}. We therefore calculate upper limits on the photodestruction cross sections and find upper limits of 2.3×10^{-19} cm^2 for CH_4 and 1.6×10^{-19} cm^2 for CO_2.

Our results show that the quantum efficiencies for photodestruction using the Lyman-α dominated lamp increase in the following order: $NH_3 < H_2O(\text{high T}) < CH_4 < CH_3OH < CO_2$. Using the H_2/D_2 lamp we find $NH_3 < CH_3OH < CH_4 < CO_2$. The absolute cross sections are higher for the H_2D_2 lamp for all species at 25 K; however, the current uncertainties in the lamp flux calibrations must be addressed before we can compare the absolute cross sections. Instead we note that the quantum efficiency for CH_4 is higher than CH_3OH using the H/D_2 broadband lamp and lower than CH_3OH using the H_2/Ar Ly-α lamp. We plan to conduct further experiments to determine if this is a wavelength dependent effect.

6.5 Discussion

6.5.1 Ice Photodestruction Processes

The photodestruction kinetics for pure ices display a number of trends that allow us to extract information about the various pathways available in the ices following photoexcitation. All of the pure ices measured display a temperature dependence in their photodestruction cross sections, except for CO_2 ice. We found that the photodestruction rate of CO_2 is independent of the ice temperature between 25-65 K. This could suggest a low cage barrier; however, we also find that the quantum efficiency is lower than the gas-phase (0.4 compared to 1), which suggests that a cage effect could be present. The absence of a temperature dependence implies that the dominant reactions reforming CO_2 do not involve thermal diffusion. This result has implications for understanding the formation of CO_2 in quiescent dense clouds where the production of OH radicals may be too low for CO + OH to account for the CO_2 abundances that are observed. The irradiation of pure CO ices with UV photons or energetic electrons yields the formation of CO_2 ice. This is thought to occur by the $CO + CO^*$ reaction as the dissociation of threshold of CO is above the energy of UV-lamps [15].

The temperature dependencies observed in the ice photodestruction cross sections of CH_4, NH_3 and CH_3OH suggest the presence of cage effects. The methanol photodestruction cross sections increase exponentially as the ice temperature increase, possibly following the exponential dependence of the diffusion rates of photoproducts. Methane ices also show a rapid increase in the photodestruction rate as the temperature is increased. Photodestruction cross sections of 2.9×10^{-19} cm^2 and 1.5×10^{-19} cm^2 were measured for CH_4 ices 13 ML and 32 ML thick, both at 20 K. Within this thickness range, effects of ice penetration depths are negligible, suggesting an alternate mechanism for the increased photodestruction cross section in the thin CH_4 ice. One possibility is the decreased trapping of photo-fragments as the ice thickness is decreased. If the photofragments desorb more efficiently after formation then less of the parent ice can be reformed by radical recombination. A similar effect may also contribute to the larger quantum efficiencies for the photodestruction of thinner NH_3 and CH_3OH ices.

The relative photodestruction cross sections are also affected by the presence of other ice species in the binary ice mixtures. These species can change the photodestruction cross sections by a number of mechanisms. Firstly, reactions between the photofragments of the two ice constituents can change the net photodestruction cross section. If reactions between the photofragments produce new species, the net reformation of the parent ice is decreased and the photodestruction cross section increases. An example of this is the increased cross section for photodestruction of CO_2 in an NH_3 ice mixture. The presence of N=O and H-N-OH mode in the infrared spectra suggest that reactions between the two ice components occur, decreasing the reaction channel(s) that reform CO_2. Tsegaw et al. [216] found that hydroxylamine formed during the electron irradiation of NH_3/O_2 ices. They suggest that the hydroxlamine is formed by suprathermal O atom insertion into ammonia, indicating a similar insertion route by $O(^1D)$ may be present in the irradiation of NH_3/CO_2 ices:

$$CO_2 \longrightarrow CO + O(^1D) \tag{6.32}$$

$$NH_3 + O(^1D) \longrightarrow NH_2OH \tag{6.33}$$

On the other hand, if reactions between the photofragments of the two ice components efficiently reforms one of the parent ices, the net photodestruction cross section can decrease. This is most evident in the CO_2/H_2O binary ice mixture where the photodestruction cross section for CO_2 is lower than the pure ice. The most likely explanation for the decrease in the net photodestruction rate is the efficient reformation of CO_2 via the reaction between CO and OH:

$$\mathrm{CO} + \mathrm{OH} \longrightarrow \mathrm{CO_2} + \mathrm{H} \tag{6.34}$$

This reaction has been assigned a small barrier of 80 K [189], though it has been shown to efficiently form CO_2 in the solid phase (e.g. Oba et al. [157]).

The photodestruction cross sections can also be changed in binary ice mixtures due to changes in the magnitude of cage effects. If the ice is isolated in a matrix that is more strongly binding than the pure ice, the cage barrier can be increased relative to the pure ice. The photodestruction cross section may then be decreased by increasing the probability of electronic relaxation and/or the immediate recombination of radicals compared to their diffusion. This is another possible explanation for the decrease in the photodestruction cross section of CO_2 in H_2O ice mixtures. In this case, the van der Waals interactions between the H_2O ice and the CO_2 molecules may increase the cage barrier for exit of the CO and O photo-fragments, resulting in less net destruction of CO_2.

The relative importance of these processes in decreasing the photodestruction cross sections could be investigated using isotopic experiments for each of the binary ice systems. For example, by isotopically labelling the O-atoms in H_2O, the CO_2 formed by CO + OH would be spectrally distinguishable, allowing one to determine whether the photodestruction cross section is decreased due to reactions between photofragments or due to increased cage effects.

Lastly, the binary ice mixtures may trap newly formed photofragments to a greater degree than the pure ice. This would have the effect of decreasing the ice photodestruction cross section if the trapped radicals can reform the parent ice. Most likely, the net photodestruction cross sections we report for the binary ice mixtures are a balance of all these effects. Further detailed experiments on each binary ice system, as well as microscopic modelling, will be required to untangle the importance of each process on net photodestruction rate.

6.5.2 INFLUENCE OF ICE STRUCTURAL CHANGES

Infrared spectroscopy is the most common tool used to measure bulk photodestruction processes in ices. The column densities derived from infrared bands depend on optical constants associated with the ice crystal structure and matrix environment. As the ice photolysis progresses, the ice lattice structure can become more ordered (due to local heating) or disordered (due to radiation damage); the band strengths used to derive the ice loss during irradiation are then also a function of photolysis time and can not always be assumed to be constant. If this is not explicitly accounted for, the ice photodestruction cross sections reported may include the kinetics associated with photon induced ice reorganization rather than the photodestruction of the parent ice.

An example of this evident in our experiments is the photodestruction of water ices. To check the relative band strengths of the H_2O ice structures, we measure the integrated absorbance of an ice deposited at 25 K, and then following annealing to 120 K and cooling back down to 25 K. We find that the integrated absorbance of the annealed O-H stretching band is 1.27× that of the O-H band for the un-annealed ice. Therefore, if the ice is amorphized during photo-irradiation, the associated change in band strength would artificially increase the measured photodestruction rate. We see a similar effect in the photoirradiation of ammonia ices, where ice reorganization results in an increased infrared absorbance that masks the effects of photodestruction. In this case, the effect appears to be less important for thinner ammonia ices, suggesting that the ice photo-reorganization rate depends on the ammonia thickness. For methane ices spectral band shape changes are most prominent for the ice deposited at 15 K. The infrared spectral features shift in the direction of the high temperature crystalline phase which has a thermal transition point $\sim$20 K [94]. The band shapes of the methane ices deposited at 20 and 25 K do not change

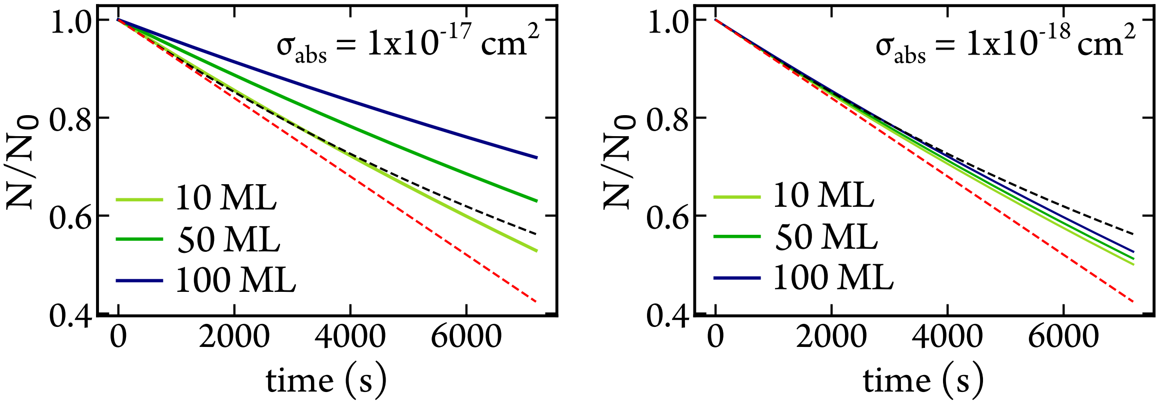

Figure 6.5.1: Deviations from zeroth- and first-order kinetics for different ice thicknesses between 10-100 ML using the thick ice equation derived in Cottin et al. [48]. Examples are shown for absorption cross sections of 1×10^{-17} cm^2 and 1×10^{-18} cm^2.

during the irradiation indicating that the high-temperature crystalline state is more stable to UV radiation than the low-temperature crystalline state.

Such spectral changes are usually neglected in the calculation of kinetic rates and should be considered in order to correctly associate changes in the IR-absorbance with the process of interest, rather than bulk structural changes in the ice.

6.5.3 Optical Depth Considerations

In the previous sections, our experiments showed that the photodestruction rates depend on the ice thickness, especially if the lamp emits a large proportion of Ly-α. The photodestruction cross sections have been previously measured for ices of various thicknesses in the nanometer to micrometer range. Gerakines et al. [90] irradiated ices 0.1 μm thick through which the UV photons should totally penetrate, even if the lamp is dominated by Ly-α. We measured three of the same ice molecules as Gerakines et al. [90] and find similar (within 30%) absolute photodestruction cross sections as well as the same order of increasing photodestruction rate, that is $\sigma(CH_3OH) > \sigma(CH_4) > \sigma(CO_2)$.

Cottin et al. [48] studied ices of thickness in the range of 0.5-1.5 μm thick using a lamp with emission dominated by the Lyman-band system and peaking at 161 nm. Assuming similar effective absorption cross sections for our H_2/D_2 lamp, the CH_3OH and NH3 ices would have been optically thick, while the CH_4 and CO_2 absorbed ∼80% and ∼50% of the UV photons respectively. This could explain why they find a similar value for to us (and Gerakines et al. [90]) for CO_2 ice photodestruction, but a lower value for CH_3OH ice. We find a similar NH_3 photodestruction cross section even though NH_3 is optically thick in their study; however, the ammonia ice in our study was annealed and therefore may present a stronger cage effect than low temperature NH_3 ice. They find a lower photodestruction cross section for methane ice, consistent with lower VUV-absorption in the Lyman-band system compared to Lyman-alpha but may also be partially due to the ice optical thickness.

Figure 6.5.1 emphasizes how the ice opacity can affect the measured photodestruction cross sections if first-order kinetics are assumed regardless of the UV-penetration. We calculate the normalized fraction of un-dissociated molecules (N/N_0) using the thick ice equation reported in Cottin et al. [48], which assumes that the photodestruction rate is not constant and is a function of the ice depth. The initial photodestruction rate (J_0) is chosen to be the same for both cases, though it is important to note that J_0 depends on the lamp flux ($J = \sigma \times$ Flux). The left hand panel shows an example of the ice loss rate for strongly absorbing ices ($\sigma_{abs} = 1 \times 10^{-17}$ cm^2) 10, 50 and 100 ML thick. The zeroth- and first-order kinetic curves are shown in the red and black dashed lines respectively. This is representative of CH_4, NH_3 and CH_3OH absorption at Lyman-alpha. The photodestruction rate approaches first-order kinetics when the ice is 10 ML thick, so ices 50 and 100 ML thick would underestimate the photodestruction cross section if fit with first-order kinetics. The right-hand panel shows the same ice thicknesses for an ice absorption cross section of 1×10^{-18} cm^2, representative of CH_4, NH_3, H_2O and CH_3OH ice irradiation with the H_2/D_2 lamp. In this case, the first order kinetics fit would produce the same photodestruction cross section as the depth-dependent model for all of the ice thicknesses.

It is clear that the lamp spectral profile should be taken into consideration when determining the validity of a first-order kinetics fit to extract the photodestruction cross sections. If a large portion of Lyman-alpha is present the cross-sections may be underestimated even if the ices are $<$100 ML thick. This may explain some of the discrepancies between the quantum efficiencies we measure using the two lamps in this study, as well as across the measurements made in different laboratories.

Water photodestruction efficiency

In this study we measured the photodestruction cross-section for solid phase water ice at 120 K. The low quantum efficiency for photodestruction measured is of particular astrophysical importance due to the prevalence of water ice during all stages of star-formation as well as in comets. The photodestruction cross section of 1.8×10^{-19} cm^2 is almost two-orders of magnitude lower than the gas-phase value at Lyman-alpha of 1.5×10^{-17} cm^2 [107], while the absorption cross section is only about half that measured in the gas-phase [49]; indicating a strong cage effect in water ices. As such, we would expect the photodestruction rate to be temperature dependent and therefore even lower at 10-20 K. The water ice photodestruction in an argon matrix likewise points at a strong cage effect, giving a photodestruction cross section of 1.6×10^{-18} cm^2 compared to the convolved absorption cross section of 1.7×10^{-18} cm^2 i.e. a quantum yield approaching 1. A low water photodestruction cross section has important astrochemical implications. In particular. water is known to be coupled to CO_2 formation via the CO + OH reaction in which the OH is primarily produced by water photolysis. Decreased production of OH in the ice may lead to lower abundances of CO_2 in the polar phase than is currently produced by astrochemical models.

Table 6.5.1. Estimated half-lives ($t_{1/2}$) for pure ices and ices in binary ice mixtures for a typical UV-fluxes in dense cloud cores induced by cosmic rays and cloud edges that is not exposed to any massive star-formation.

UV Flux ($cm^{-2}\ s^{-1}$)	Ice	$t_{1/2}$ pure ice	$t_{1/2}$ in H_2O	$t_{1/2}$ in CO_2	$t_{1/2}$ σ_{gas} Lyα[a]
10^3	CO_2	6×10^7	1×10^8	–	3×10^8[b]
	CH_4	2×10^7	2×10^7	1×10^7	1×10^6
	H_2O	$>1\times10^8$	–	–	2×10^6
	NH_3	$<7\times10^8$	2×10^8	5×10^7	3×10^6
	CH_3OH	2×10^7	2×10^7	3×10^7	2×10^6
10^8	CO_2	540	1200	–	3400
	CH_4	240	160	130	12
	H_2O	1200	–	–	14
	NH_3	6690	1670	460	26
	CH_3OH	180	180	260	16

[a] The half-lives estimated using the gas-phase values are lower limits and represent only photodestruction sinks for the ice species i.e. no recombination events or formation via other reaction channels

[b] CO_2 absorbs weakly at Ly-α, so the gas-phase survival would be shorter other parts of the VUV-spectrum are considered.

6.5.4 ASTROPHYSICAL IMPLICATIONS

The measurements in this study, combined with previous measurements, show definitively that ice photodestruction quantum efficiencies ares lower than their gas-phase counterparts. This has important implications for astrochemical models of UV-induced processes on dust grains, which often use the gas-phase absorption cross sections to calculate photodestruction rates. Some gas-grain chemical kinetics models treat photodissociation events separately to recombination events that reform the parent ice. Relaxation from electronic states is typically not explicitly treated, though electronic processes are beginning to be incorporated into some models [200]. The cosmic ray induced photodissociation rates in the gas-phase are calculated using $k = b \times \zeta$, where ζ is the cosmic ray ionization rate and b is the photodissociation efficiency for the ice photodissociation channel of interest, derived by Gredel et al. [99]. The photodestruction efficiency is calculated by convolving the UV-emission spectrum with the photodissociation cross section and summing over all UV wavelengths to give the efficiency factor, b. As mentioned, in many cases the absorption cross sections are used in lieu of laboratory data reporting the photodissociation cross sections. The gas-phase values of b are usually used to calculate the rates of cosmic-ray induced photodissociation in ices, though these will likely be overestimated given the lower values found for both the absorption cross sections [49, 50] and the quantum efficiencies (this study).

Table 6.5.1 shows the estimated half-lives for the ice species with UV-fluxes on the order of those present in dense clouds and at cloud edges that are not exposed to massive star-formation. We calculate the half-lives using the cross sections obtained in this study for the pure ices and the ices in binary mixtures with H_2O and CO_2. We also calculate the half-lives assuming gas-phase photodissociation cross sections. These numbers should be taken as lower limits for the survival timescales of the ice molecules, especially when using the pure ice and gas-phase photodestruction cross sections. Table 6.5.1 show that the survival time is longer for the pure ice than using the gas-phase photodissociation cross section. In models, though the gas-phase photodissociation cross sections are often used, the recombination rates for photofragments are also estimated and used independently as a formation route. It should be noted that this method requires good knowledge of both diffusion barriers and reaction rates for radical species which have not been measured in the laboratory and are highly uncertain. The survival rates in H_2O and CO_2 ices incorporate some of the sources and sinks for the ice species. For example, CO_2 survives longer in H_2O ice due to its reformation by the CO + OH reaction, and possibly a larger

Table 6.5.2. Recommended cross sections and quantum efficiencies for use astrochemical models in units of 10^{-19} cm^2

Ice	σ(pure ice)	$\sigma_{Ly\alpha}$(dirty ice)[a]	σ(upper)[b]	Φ(pure ice)	Φ(upper)[b]
CO_2	4.1	1.8(p)/4.0(a)[c]	9.5	0.4	0.95
CH_4	9.2	14	–	0.07	–
H_2O	1.8	–	–	0.04	–
NH_3	0.33	1.3	3.0	0.004	0.03
CH_3OH	12	12	32	0.14	0.4

[a] Refers to the cross section obtained for binary ice mixtures that best represent the astrophysical environment of the ice species.

[c] (p) and (a) refer to polar (water-rich) and apolar (CO-rich) ice environments.

[b] Refers to the cross section and quantum efficiency which involves the lowest amount of immediate recombinations, either in a rare-gas or at the highest temperature.

amount of recombination due to an increased cage effect. In contrast, the presence of CO_2 mixed with NH_3 reduces its survival time by an order of magnitude due to fast chemistry between the photoproducts of NH_3 and CO_2. This emphasizes the importance of understanding the ice mixing environments as the net photon-induced destruction could vary substantially between different ice environments.

6.5.5 RECOMMENDATIONS

An important goal of this research is to provide modellers with quantitative solid phase photodestruction cross sections for direct input into astrochemical models. The recommended cross sections from our experiments are listed in Table 6.5.2. The photodestruction cross sections in the pure ice, σ(pure ice), include both relaxation of electronically excited species as well as immediate recombination events that reform the parent molecule. In models where the rates of relaxation and recombination are implemented independently, input of the pure ice photodestruction cross sections will underestimate the photodestruction rates. The values measured where diffusion is easiest, denoted $\sigma(\text{upper})$, that is in the rare-gas matrices or at temperatures closest to the ice desorption temperature, should be used in this case as immediate recombinations due to cage effects are minimized. However, it is important to note that the energy dissipation rates will differ between the rare-gas matrices and for e.g. water ice matrices.

In models where ice recombination reactions are not explicitly considered, or in cases where the recombination is highly uncertain, we recommend the use of the photodestruction cross sections obtained for the "dirty ice" mixtures ($\sigma_{Ly\alpha}(\text{dirty ice})$), that is, the values obtained in binary mixtures closest to the astrophysical environment of the ice species. The binary ice mixtures best representing the ice environments are then: CO_2 in CO (apolar) or H_2O (polar), CH_4 in H_2O, NH_3 in H_2O and CH_3OH pure or in CO. We also list the quantum efficiencies for photodestruction for the pure ices and in the limit where the cage effect is minimized. These quantum efficiencies can be applied to the Gredel et al. [99] formalism to calculate rates of cosmic ray induced photodissociation in ices:

$$\text{k(ice)} = \zeta \times \text{b(ice)} \tag{6.35}$$

Where k(ice) is the photodissociation rate in the ice, ζ is the cosmic ray ionization rate and b is:

$$\text{b(ice)} = \int^{\lambda=91.2\text{nm}} \frac{\sigma_{abs}(\lambda) \times \Phi(\text{this study}) \times P(\lambda)}{\sigma_g}\, d\lambda \tag{6.36}$$

where $\sigma_{abs}(\lambda)$ is the wavelength dependent absorption cross section, Φ is the photodestruction quantum efficiency as measured in this study, $P(\lambda)$ is the probability of emitting a photon of wavelength λ, and σ_g is the grain extinction cross section per hydrogen molecule. The

VUV-absorption spectra (e.g. Cruz-Diaz et al. [49, 50]) can then be convolved with the VUV-emission spectrum for the radiation field and multiplied by the quantum efficiency for photodestruction. In reality, the quantum yields for photodestruction may be wavelength dependent and studies of photodestruction at different UV wavelengths are therefore critical. The quantum efficiencies reported in Table 6.5.2 were measured using the dominantly Lyman-α lamp and therefore may be most relevant to the ice photodestruction rates in interstellar regions where Lyman-α emission is dominant e.g. in PDRs or at protoplanetary disk surfaces.

6.6 CONCLUSIONS

In this work we have reported the photodestruction kinetics of optically thin pure ices and binary ice mixtures of CO_2, CH_4, H_2O, NH_3 and CH_3OH. We systematically measured the effects of ice thickness and temperature on the photodestruction cross sections. We also measured and discussed trends in the relative photodestruction cross sections for various binary ice mixtures. We make the following major conclusions:

1. We find the photodestruction quantum efficiencies are lower in the ice than in the gas-phase for all of the pure ices studied.
2. We find that the photodestruction rates of NH_3, CH_4 and CH_3OH ices increase with temperature, suggesting cage effects that result in less reformation of the parent ice molecules as the temperature is increased. This is can be explained by increased diffusion of the photoproducts at higher temperatures.
3. We find that the photodestruction cross section for CO_2 ice is temperature independent. This suggests that CO_2 may be reformed by a non-thermal or non-diffusive process.
4. We measure a low quantum efficiency of 0.04 for water ice photodestruction by Lyman-alpha at 120 K. This suggests that less OH may be available in ice mantles than is

currently assumed by astrochemical models.

5. We find that the net photodestruction cross sections depend on the ice composition in binary ice mixtures of CO_2, CH_4 and NH_3. Methanol ice photodestruction is not strongly affected by the presence of other ice constituents at low fluence, possibly due to its larger photodestruction cross section.

We would like to thank Rob Garrod, Eric Herbst, Tyler Pauly, Matthew Reish, Jennifer Bergner, Eric Willis and Edith Fayolle for useful discussions. I.R.C. acknowledges support from the Sidney M. Hecht Graduate Fellowship and the Department of Chemistry, University of Virginia. K.I.Ö. acknowledges funding from the Simons Collaboration on the Origins of Life (SCOL) and the David and Lucile Packard Foundation.

7

Conclusions and Future Directions

This thesis presents experiments undertaken in order to provide constraints on various solid state processes important to astrochemistry. Beginning graduate school under the mentorship of John Yates, I was excited to learn how to approach astrochemical problems with the eyes of a surface scientist. Surface scientists have a tradition of following in great detail, interactions between well defined surfaces and small molecules. Interstellar ices surfaces present a new challenge to those trained in surface science, with their irregular structures and compositions that vary depending on the astrophysical environment and their chemical evolution over time. Since the beginning of this PhD, I have learnt a great deal about the physical conditions and variability of the ices whose processes I have been studying in the laboratory. Discussions with modellers and observational astronomers have allowed me to better motivate my experiments to provide useful data for the astronomical community. In the coming years, JWST promises to deliver data with better sensitivity and resolution in the infrared than previously possible. Laboratory experiments will be required to help answer questions about how the ices are formed, how long they survive and why their abundances many vary across astrophysical environments. The laboratory data will help to inform models that will aim to chemically reproduce the ice compositions and abundances observed by JWST. Below I summarize the main findings of this work and highlight future areas of study.

7.0.1 Gas-grain surface reactions

In chapter 3 we studied the Eley-Rideal type reaction between CO(g) and surface OH radicals. We found that the reaction occurs with a cross section of 6×10^{-20} m^2 and a barrier of 6 meV. The reaction cross section is of the order of geometric cross section, providing further evidence that CO does not diffuse on the surface before reaction. The CO(g) + OH channel competes with the surface recombination of OH which consumes the majority of the photoproduced OH species. This reaction may be relevant where OH radicals accrete from the gas-phase or form directly on ice surfaces and are exposed to CO gas. The most likely astrophysical environments where the CO + OH E-R reaction could take place are in photon-dominated regions (PDRs) towards the edges of clouds or in the upper layers of protostellar disks. In the ISM, the CO gas column density is orders of magnitude lower than H_2, and even H in warmer PDR regions where Lyman-alpha radiation may dominate. The CO(g) + OH process may be less efficient in these astrophysical environments than measured in the laboratory due to competitive E-R reactions between H_2 + OH (or H + OH) as well as OH + OH recombination on the surface. It is clear that both further experiments measuring the rates of E-R processes, as well as input of these rates into astrochemical models, are required to determine whether these processes are efficient in the ISM.

In most astrophysical models, Eley–Rideal mechanisms are neglected due to the low densities expected for reactive species on either the grain surfaces or in the gas. However, in some astrophysical environments, reactive species in the gas-phase may be of sufficient density that the E-R mechanism becomes important. The E-R reaction between carbon atoms with ice surface species was modelled by Ruaud et al. [187], with the premise that carbon atoms are reactive with most molecules adsorbed on grain surfaces and are present in the gas-phase at high abundances. They showed that Eley–Rideal and complex induced reaction mechanisms considerably enhance the abundance of the most COMs and suggested that such mechanisms are a potential route to the unexplained presence of COMs in the gas-phase at low temperature.

Since our work on the CO(g) + OH reaction, He et al. [106] have studied the mechanism of H atom addition to O_3 to produce O_2 and OH. They observe a lack of temperature dependence inconsistent with either the Langmuir -Hinshelwood or tunneling mechanisms that are typically assumed in astrochemical models. They show that the reaction rate is governed by the kinetics of the H-atoms and it is therefore likely that similar mechanisms exist for other low-barrier H-atom addition reactions on grains.

Future work should involve studies of other E-R and hot atom mechanisms geared toward processes that could be efficient in the ISM. Competitive reactions could also be studied by introducing gas mixtures e.g. CO diluted in H_2 incident on an irradiated H_2O ice surface. These studies will help better understand the extrapolation of such reaction mechanisms to dense cloud conditions. Eley-Rideal type reactions between OH and other prevalent gas-phase species should also be quantitatively studied and their kinetics input into astrochemical models where relevant.

Another critical aspect is the fraction of products that remain on frozen on the ice surface following an E-R or hot atom reaction. In our study of CO(g) + OH, it was unclear how much the

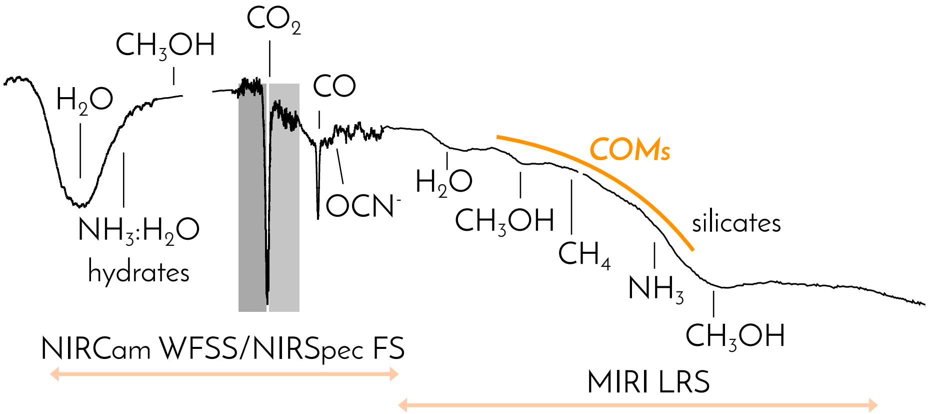

Figure 7.0.1: Image showing the spectral range of JWST's Near-IR Camera wide field slitless spectroscopy (NIRCam WFSS), Near-IR spectrograph fixed slits (NIRSpec FS) and Mid-IR Instrument in low resolution (MIRI LRS) modes that will be used to demonstrate JWST's ice mapping ability in the early science release stage. Image modified from K. Pontopiddan.

solid phase CO_2 monitored by IR constitutes the total amount of CO_2 produced in the reaction. These studies are complementary to chemical desorption measurements of molecules that desorb following Langmuir-Hinshelwood reactions. The chemical desorption mechanism has been invoked as a possible route to release COMs into the gas-phase at low temperature; however, experiments are beginning to show the fraction of molecules desorbed by this mechanism may be low. One might expect that the chemical desorption following an E-R reaction would be more efficient since only one of the species is accommodated by the surface and the incoming gas-phase species will have excess energy. Detailed laboratory measurements followed by modelling will be required to determine whether this mechanism could produce any appreciable molecular abundances in astrophysical environments.

7.0.2 Laboratory IR Spectra for Ice Observations

Laboratory studies of the infrared spectral signatures of pure ices and ice mixtures are essential with the upcoming launch of JWST. Not only are low temperature spectra necessary, but also spectra of ices subject to processes believed to take place during star-formation e.g. heating, energetic irradiation, atom bombardment.

Chapter 4 presented a study of CO_2 longitudinal phonons and their response to the ice composition by measuring the spectra of CO_2 ices mixed with CO, O_2 and H_2O. We show that the CO_2 LO phonons red-shift with increasing concentrations of CO_2, O_2 or H_2O. The peak frequency of the CO_2 LO modes, if observed, could provide an additional constraint on the ice composition. CO_2 ν_3 LO phonons at $\sim$2380 cm^{-1} (4.20 μm) would be a sure sign of pure CO_2 ice since the presence of other ice species, even at low concentration, would shift the LO mode.

Figure 7.0.1 shows the spectral coverage of instruments on JWST that will be used during the early science release phase to map ice compositions in the Chameleon I cloud at higher sensitivity and resolution than previously possible [144]. JWST will also deliver early science data probing different stages of star-formation by observing a prestellar core, a protostar and an edge on protoplanetary disk. Within this spectral range, CO_2 LO phonons may be visible, particularly on the strong CO_2 ν_3 mode and if the source is highly polarized. These data will likely provide a new set of challenges from laboratory astrophysicists in order to explain the molecular origin of the observed bands and their formation routes. During this time it will be important for the community to make IR-spectra publicly available in such a way that they can be used by observers to fit the new astronomical spectra.

7.0.3 Diffusion and Desorption Processes in Ices

Diffusion barriers are essential for input into astrochemical models aiming to reproduce interstellar molecular abundances; however, their laboratory measurement remains a challenge. Chapter 5 presented measurements of CO diffusion through CO_2 ice at low temperature by utilizing the CO_2 LO phonon sensitivity to CO mixing.

Diffusion barriers are often measured through reaction, typically at a temperature where one reactant is mobile and the other is stationary. If the reaction does not have a barrier and the surface coverage is low, the reaction is diffusion limited and the diffusion barrier is extracted from temperature reaction rate experiments. This method is limited to reactive species and is subject to low sensitivity since the experiments require submonolayer coverages.

The other camp of experiments involve layering the diffusing species beneath the ice of interest (usually ASW) and following the diffusion by infrared spectroscopy. If the temperature is above the desorption temperature of the diffusing species, the rate limiting step for desorption is the diffusion of the species through ice layer. The disappearance of the diffusing species is monitored by following the decreasing IR absorbance. If the ice is kept below the desorption temperature the concentration of molecules mixed into the ice layer is monitored by following spectral changes.

For the many species in astrochemical models the diffusion barrier is assumed to be a universal, fixed fraction (f) of the better constrained desorption energy such that $E_{diff} = f \times E_{des}$. There is no physical reason for a universal ratio to exist and it is used solely due to the lack of diffusion data. Our results show that this ratio depends not only on the ice species but also the ice structure. Future work should be focused on continued measurements of diffusion barriers and especially how the diffusion-desorption barrier ratios change with ice porosity. It is likely that for amorphous structures, a range of diffusion barriers exist following the energy distribution of binding sites. Desorption energy measurements made for the same ice system can therefore be informative as to the spread of surface binding energies.

7.0.4 PHOTODESTRUCTION PROCESSES IN ICES

Photoprocesses, including photodissociation and the resulting product formation channels and branching ratios, remain highly uncertain in astrochemical models. Chapter 6 presented a new survey study of photodestruction kinetics for a range of ice species in pure ices at different temperatures as well as in binary ice mixtures. We find that the ices (except for CO_2) display temperature dependent photodestruction rates, suggesting cage effects in the ice that lower the quantum efficiencies compared to the gas-phase. The photodestruction cross sections in binary ice mixtures can provide further details about the mechanisms that affect the total photodestruction rates of different ice constituents.

An important result of this study is the influence of IR band shape changes on the calculated photodestruction cross sections. We recommend that future studies attempt to include these effects in their derivations of photodestruction rates or try to mitigate them by e.g. irradiating thin ices or ices close to their desorption temperature. An experimental tool that does not rely on the ice physical properties would be better suited to study ice photodestruction rates; however, it is difficult to envision a tool that could be used *in situ* and non-destructively.

Further work should also consider carefully the spectral profile of the UV-sources employed and the resultant optical thickness of the ice. This will determine whether assuming first-order kinetics (as is done in most studies) is appropriate for the ice photodestruction.

Wavelength dependencies of ice photodestruction processes are mostly unknown and are important for modelling astrophysical regions with different UV-fields. In chapter 6 we are working towards a small part of this problem by studying the photodestruction rates using two different H_2 lamps with complementary spectral emissions. Synchrotron studies could provide useful measurements of wavelength dependent photodestruction, especially now that the VUV-absorption spectra have been measured for many ice species. Another consideration is photon-induced processes below 110 nm, where the MgF_2 windows used with most H_2 lamps cutoff the the short wavelength emission. At shorter wavelengths, CO and N_2 ice can be photodissociated, new electronically excited states become accessible as well as ionization of many ice species. It will therefore be important to measure quantum yields at these wavelengths to best model UV-processes occurring in the ISM.

7.0.5 Directions For Laboratory Ice Astrophysics

"We urge the experimental community to continue to push the boundaries of what is possible in the laboratory and develop innovative methods to quantify the necessary data for radicals. In astrochemical models used to simulate interstellar and circumstellar environments, the data adopted for radicals remains the most uncertain." - Herma Cuppen *et. al.*, 2017

"The key for a fruitful interaction is for astronomers to ask the right questions and have enough chemical physics knowledge of what can, and what cannot, be done in the laboratory. Chemists, in turn, have to sometimes let go of perfectionism, since astronomers are often content at the factor of 2 uncertainty level. Also, astronomers just want a number rather than a deep understanding of the underlying molecular processes." Erwine van Dishoeck, 2017

Laboratory astrophysics continues to be an essential component of the interdisciplinary field of astrochemistry. Results delivered from cutting edge telescopes are expanded and enriched by the input of laboratory data. One of the biggest uncertainties in astrochemical models is the rate reaction, diffusion and desorption of radicals. These data are particularly challenging in the laboratory but new techniques as well as collaborations between experimentalists and theorists from different backgrounds, will continue to step closer to providing these critical data.

Perhaps one of the biggest surprises of the last ten years is the observation of complex molecules in cold prestellar cores (e.g. Bacmann et al. [8]). The biggest mystery is not their formation but their presence in the gas-phase at dust temperatures below that required for thermal desorption. A number of non-thermal processes are beginning to be investigated including photodesorption, reactive (chemical) desorption and cosmic-ray induced sputtering or spot heating. Most results have shown that these mechanisms may lead preferenatially to desorption of fragments rather than the intact COMs. Laboratory astrophysicists should continue to make measurements to constrain these mechanisms as well as other possibilities that could form COMs in prestellar conditions, including alternate scenarios to the currently accepted ice formation routes.

Being by nature an interdisciplinary field, the future directions of laboratory astrophysics will both be informed by, and will inform, the new directions in observational astronomy. Together, these collaborations will enable us to better understand chemical evolution during star-formation and build a more complete picture of the origins of new planetary systems and their potential for terrestrial-like prebiotic chemistry.

References

[1] Al-Halabi, A., Fraser, H. J., Kroes, G. J., & van Dishoeck, E. F. 2004, A&A, 422, 777

[2] Al-Halabi, A., van Dishoeck, E. F., & Kroes, G. J. 2004, The J. Chem. Phys., 120, 3358

[3] Allamandola, L. J., Sandford, S. A., & Valero, G. J. 1988, Icarus, 76, 225

[4] Alves, J. F., Lada, C. J., & Lada, E. A. 2001, Nature, 409, 159

[5] Aikawa, Y., Kamuro, D., Sakon, I., et al. 2012, A&A, 538, A57

[6] Andersson, S., & van Dishoeck, E. F. 2008, A&A, 491, 907

[7] Arasa, C., van Hemert, M. C., van Dishoeck, E. F., & Kroes, G. J. 2013, J. Phys. Chem. A, 117, 7064

[8] Bacmann, A., Taquet, V., Faure, A., Kahane, C., & Ceccarelli, C. 2012, A&A, 541

[9] Balucani, N., Ceccarelli, C., & Taquet, V. 2015, MNRAS Lett, 449, L16

[10] Baratta, G. A., & Palumbo, M. E. 1998, JOSAA, 15, 3076

[11] Baratta, G. A., Leto, G., & Palumbo, M. E. 2002, A&A, 384, 343

[12] Bates, D. R., & Witherspoon, A. E. 1952, MNRAS, 112, 101

[13] Belloche, A., Müller, H. S. P., Menten, K. M., Schilke, P., & Comito, C. 2013, A&A, 559

[14] Bennett, C. J., Jamieson, C., Mebel, A. M., & Kaiser, R. I. 2004, Phys. Chem. Chem. Phys., 6, 735

[15] Bennett, C. J., Jamieson, C. S., & Kaiser, R. I. 2009, Phys. Chem. Chem. Phys., 11, 4210

[16] Benson, P. J., & Myers, P. C. 1989, ApJS, 71, 89

[17] Bergin, E. A., Melnick, G. J., Gerakines, P. A., Neufeld, D. A., & Whittet, D. C. B. 2005, ApJ, 627, 33

[18] Bergner, J. B., Öberg, K. I., Rajappan, M., & Fayolle, E. C. 2016, ApJ, 829, 85

[19] Bernstein, M. P., Sandford, S. A., Allamandola, L. J., Chang, S., & Scharberg, M. A. 1995, ApJ, 454, 327

[20] Bertin, M., Romanzin, C., Doronin, M., et al. 2016, ApJL, 817, L12

[21] Berreman, D. W. 1963, PhRv, 130, 2193

[22] Bohren, C. F., & Huffman, D. R. 1983, Absorption and scattering of light by small particles (Wiley)

[23] Boogert, A. C. A., Pontoppidan, K. M., Lahuis, F., et al. 2004, The ApJS, 154, 359

[24] Boogert, A. C. A., Pontoppidan, K. M., Knez, C., et al. 2008, ApJ, 678, 985

[25] Boogert, A. C. A., Gerakines, P. A., & Whittet, D. C. B. 2015, Annu. Rev. Astron. Astrophys., 53, 541

[26] Bossa, J.-B., Paardekooper, D. M., Isokoski, K., & Linnartz, H. 2015, Phys. Chem. Chem. Phys., 17, 17346

[27] Botta, O., & Bada, J. L. 2002, Surveys in Geophysics, 23, 411

[28] Bouilloud, M., Fray, N., Bénilan, Y., et al. 2015, MNRAS, 451, 2145

[29] Cazaux, S., Tielens, A. G. G. M., Ceccarelli, C., et al. 2003, ApJL, 593, L51

[30] Chang, Q., Cuppen, H. M., & Herbst, E. 2005, A&A, 434, 599

[31] Chang, Q., & Herbst, E. 2012, ApJ, 759, 147

[32] Chang, Q., & Herbst, E. 2014, ApJ, 787, 135

[33] Charnley, S. B., Tielens, A. G. G. M., & Millar, T. J. 1992, ApJL, 399, L71

[34] Chen, Y.-J., Chuang, K.-J., Muñoz Caro, G. M., et al. 2014, The ApJ, 781, 15

[35] Cheng, C. C., Lucas, S. R., Gutleben, H., Choyke, W. J., & Yates, J. T. 1992, JACS, 114, 1249

[36] Cheung, A. C., Rank, D. M., Townes, C. H., Thornton, D. D., & Welch, W. J. 1968, Phys. Rev. Lett., 21, 1701

[37] Cheung, A. C., Rank, D. M., Townes, C. H., Thornton, D. D., & Welch, W. J. 1969, Nature, 221, 626

[38] Chiar, J. E., Pendleton, Y. J., Geballe, T. R., & Tielens, A. G. G. M. 1998, ApJ, 507, 281

[39] Chuang, K.-J., Fedoseev, G., Qasim, D., et al. 2018, ApJ, 853, 102

[40] Clark, I. D., & Noxon, J. F. 1970, J. Geophys. Res., 75, 7307

[41] Cleeves, L. I., Bergin, E. A., Alexander, C. M. O., et al. 2014, Science, 345, 1590

[42] Collings, M. P., Dever, J. W., Fraser, H. J., McCoustra, M. R. S., & Williams, D. A. 2003, ApJ, 583, 1058

[43] Collings, M. P., Anderson, M. A., Chen, R., et al. 2004, MNRAS, 354, 1133

[44] Collings, M. P., Frankland, V. L., Lasne, J., et al. 2015, MNRAS, 449, 1826

[45] Cook, P. A., Ashfold, M. N. R., Jee, Y.-J., et al. 2001, Phys. Chem. Chem. Phys., 3, 1848

[46] Cooke, I. R., Fayolle, E. C., & Öberg, K. I. 2016, ApJ, 832, 5

[47] Cooke, I. R., Öberg, K. I., Fayolle, E. C., Peeler, Z., & Bergner, J. B. 2018, ApJ, 852, 75

[48] Cottin, H., Moore, M. H., & Bénilan, Y. 2003, ApJ, 590, 874

[49] Cruz-Diaz, G. A., Muñoz Caro, G. M., Chen, Y. J., & Yih, T. S. 2014a, A&A, 562, A119

[50] Cruz-Diaz, G. A., Muñoz Caro, G. M., Chen, Y. J., & Yih, T. S. 2014b, A&A, 562, A119

[51] Cruz-Diaz, G. A., Martín-Doménech, R., Muñoz Caro, G. M., & Chen, Y.-J. 2016, A&A, 592

[52] Cuadrado, S., Goicoechea, J. R., Cernicharo, J., et al. 2017, A&A, 603

[53] Cuppen, H. M., Karssemeijer, L. J., & Lamberts, T. 2013, Chem. Rev., 113, 8840

[54] Cuppen, H., M., van Dishoeck, E., F., Herbst, E., & Tielens, A., G. G. M. 2009, A&A, 508, 275

[55] D'Hendecourt, L. B., Allamandola, L. J., Baas, F., & Greenberg, J. M. 1982, A&A, 109, L12

[56] D'Hendecourt, L. B., Allamandola, L. J., Grim, R. J. A., & Greenberg, J. M. 1986, A&A, 158, 119

[57] D'Hendecourt, L. B., & Jourdain, d. M. M. 1989, A&A, 223, L5

[58] Dartois, E., Cox, P., Roelfsema, P. R., et al. 1998, A&A, 338, L21

[59] Dartois, E., & d'Hendecourt, L. 2001, A&A, 365, 144

[60] D'Hendecourt, L. B., & Jourdain de Muizon, M. 1989, A&A, 223, L5

[61] Dawes, A., Mukerji, R. J., Davis, M. P., et al. 2007, J. Chem. Phys., 126, 244711

[62] Doronin, M., Bertin, M., Michaut, X., Philippe, L., & Fillion, J.-H. 2015, The J. Chem. Phys., 143, doi:10.1063/1.4929376

[63] Dulieu, F., Congiu, E., Noble, J., et al. 2013, Scientific Reports, 3, 1338

[64] Dunham, T. 1937, Nature, 139, 246

[65] Dupuy, R., Bertin, M., Féraud, G., et al. 2017, A&A, 603

[66] Eddington, A. S. 1937, The Observatory, 60, 99

[67] Ehrenfreund, P., Boogert, A. C. A., Gerakines, P. A., Tielens, A. G. G. M., & van Dishoeck, E. F. 1997, A&A, 669, 649

[68] Ehrenfreund, P., Dartois, E., Demyk, K., & D'Hendecourt, L. 1998, A&A, 20, L17

[69] Ehrenfreund, P., Kerkhof, O., Schutte, W. A., et al. 1999, A&A, 253, 240

[70] Ehrenfreund, P., & Charnley, S. B. 2000, Annu. Rev. Astron. Astrophys., 38, 427

[71] Eley, D. D. 1948, in Advances in Catalysis, ed. W. G. Frankenburg, V. I. Komarewsky, & E. K. Rideal, Vol. 1 (Academic Press), 157–199

[72] Eley, D. D., & Rideal, E. K. 1940, Nature, 146, 401

[73] Escribano, R. M., Muñoz Caro, G. M., Cruz-Diaz, G. A., Rodríguez-Lazcano, Y., & Maté, B. 2013, PNAS, 110, 12899

[74] Falk, M. 1987, J. Chem. Phys., 86, 560

[75] Fayolle, E. C., Balfe, J., Loomis, R., et al. 2016, ApJL, 816, L28

[76] Fayolle, E. C., Öberg, K. I., Cuppen, H. M., Visser, R., & Linnartz, H. 2011, A&A, 529

[77] Fillion, J.-H., Amiaud, L., Congiu, E., et al. 2009, PCCP, 11, 4396

[78] Fillion, J.-H., Fayolle, E. C., Michaut, X., et al. 2014, Faraday Discuss., 168, 533

[79] Fournier, J., Deson, J., Vermeil, C., & Pimentel, G. C. 1979, J. Chem. Phys., 70, 5726

[80] France, K., Schindhelm, E., Bergin, E. A., Roueff, E., & Abgrall, H. 2014, ApJ, 784, 127

[81] Fuchs, G. W., Cuppen, H. M., Ioppolo, S., et al. 2009, A&A, 505, 629

[82] Fulvio, D., Brieva, A. C., Cuylle, S. H., et al. 2014, Appl. Phys. Lett., 105, 014105

[83] Garrod, R. T., & Herbst, E. 2006, A&A, 457, 927

[84] Garrod, R. T., Weaver, S. L. W., & Herbst, E. 2008, ApJ, 682, 283

[85] Garrod, R. T., & Pauly, T. 2011, ApJ, 735, 15

[86] Garrod, R. T., & Widicus Weaver, S. L. 2013, Chem. Rev., 113, 8939

[87] Garrod, R. T. 2013, ApJ, 778, 158

[88] Garrod, R. T. 2013, ApJ, 765, 60

[89] Gerakines, P. A., Schutte, W. A., Greenberg, J. M., & van Dishoeck, E. F. 1995, A&A, 296, 810

[90] Gerakines, P. A., Schutte, W. A., & Ehrenfreund, P. 1996, A&A, 312, 289

[91] Gerakines, P. A., Moore, M. H., & Hudson, R. L. 2000, A&A, 357, 793

[92] Gerakines, P. A., Bray, J. J., Davis, A., & Richey, C. R. 2005, ApJ, 620, 1140

[94] Gerakines, P. A., & Hudson, R. L. 2015, ApJ, 808, L40

[94] Gerakines, P. A., & Hudson, R. L. 2015, ApJL, 805, L20

[95] Gerber, R. B., & Krylov, A. 1994, in Reaction Dynamics in Clusters and Condensed Phases (Dordrecht: Springer Netherlands), 509–520

[96] Gillett, F. C., & Forrest, W. J. 1973, ApJ, 179, 483

[97] Gorden, R., & Ausloos, P. 1967, J. Chem. Phys., 46, 4823

[98] Gredel, R., Lepp, S., & Dalgarno, A. 1987, ApJL , 323, L137

[99] Gredel, R., Lepp, S., Dalgarno, A., & Herbst, E. 1989, ApJ, 347, 289

[100] Groth, W. E. 1937, Z. Physik. Chem., 37, 307

[101] Hagege, J., Roberge, P. C., & Vermeil, C. 1968, Trans. Faraday Soc., 64, 3288

[102] Harris, J., & Kasemo, B. 1981, Surface Science, 105, L281

[103] Hayes, J. M. 1967, Geochim. Cosmochim. Acta, 31, 1395

[104] He, J., & Vidali, G. 2014, Faraday Discuss., 168, 517

[105] He, J., Acharyya, K., & Vidali, G. 2016, ApJ, 823, 56

[106] He, J., Emtiaz, S. M., & Vidali, G. 2017, ApJ, 851, 104

[107] Heays, A. N., Bosman, A. D., & van Dishoeck, E. F. 2017, A&A, 602

[108] Herbst, E., & van Dishoeck, E. F. 2009, Annu. Rev. Astron. Astrophys., 47, 427

[109] Horn, A., Møllendal, H., Sekiguchi, O., et al. 2004, ApJ, 611, 605

[110] Hudgins, D. M., Sanford, S. A., Allamandola, L. J., & Tielens, A. G. G. M. 1993, ApJS, 86, 713

[111] Ioppolo, S., van Boheemen, Y., Cuppen, H. M., van Dishoeck, E. F., & Linnartz, H. 2011, MNRAS, 413, 2281

[112] Jacox, M. E., & Milligan, D. E. 1971, J. Chem. Phys., 54, 919

[113] Jacox, M. E., & Milligan, D. E. 1973, J. Mol. Spectrosc., 47, 148

[114] Jenniskens, P., & Blake, D. F. 1994, Science, 265, 753

[115] Karssemeijer, L. J., & Cuppen, H. M. 2014, A&A, 569

[116] Karssemeijer, L. J., Ioppolo, S., van Hemert, M. C., et al. 2014, ApJ, 781, 16

[117] Katz, N., Furman, I., Biham, O., Pirronello, V., & Vidali, G. 1999, ApJ, 522, 305

[118] King, D. A., & Wells, M. G. 1974, Proc R Soc Lond A Math Phys Sci, 339, 245

[119] Knez, C., Boogert, A. C. A., Pontoppidan, K. M., et al. 2005, ApJL, 635, L145

[120] Krim, L., Lasne, J., Laffon, C., & Parent, P. 2009, J. Phys. Chem. A, 113, 8979

[121] Kumi, G., Malyk, S., Hawkins, S., Reisler, H., & Wittig, C. 2006, JPCA, 110, 2097

[122] Kwon, J., Tamura, M., Lucas, P. W., et al. 2013, ApJL, 765, L6

[123] Kwon, J., Tamura, M., Hough, J. H., et al. 2014, ApJL, 795, L16

[124] Laas, J. C., Garrod, R. T., Herbst, E., & Weaver, S. L. W. 2011, ApJ, 728, 71

[125] Lacy, J. H., Faraji, H., Sandford, S. A., & Allamandola, L. J. 1998, ApJ, 501, L105

[126] Laffon, C., Lasne, J., Bournel, F., et al. 2010, Phys. Chem. Chem. Phys., 12, 10865

[127] Lamberts, T., Cuppen, H. M., Ioppolo, S., & Linnartz, H. 2013, PCCP, 15, 8287

[128] Lamberts, T., de-Vries, X., & Cuppen, H. M. 2014, Faraday Discuss., 168, 327

[129] Lauck, T., Karssemeijer, L., Shulenberger, K., et al. 2015, ApJ, 801, 118

[130] Laufer, A. H., & McNesby, J. R. 1968, J. Chem. Phys., 49, 2272

[131] Lazarian, A. 2007, JQSRT, 106, 225

[132] Le Bourlot, J., Le Petit, F., Pinto, C., Roueff, E., & Roy, F. 2012, A&A, 541

[133] Le Roy, L., Altwegg, K., Balsiger, H., et al. 2015, A&A, 583

[134] Lemaire, J. L., Vidali, G., Baouche, S., et al. 2010, ApJL, 725, L156

[135] Ligterink, N. F. W., Paardekooper, D. M., Chuang, K. J., et al. 2015, A&A, 584

[136] Livingston, F. E., Smith, J. A., & George, S. M. 2002, J. Phys. Chem. A, 106, 6309

[137] Loeffler, M. J., Teolis, B. D., & Baragiola, R. A. 2006, J. Chem. Phys., 124, 104702

[138] Loeffler, M. J., & Baragiola, R. A. 2010, J. Chem. Phys., 133, 214506

[139] Lu, Z., Chang, Y. C., Yin, Q.-Z., Ng, C. Y., & Jackson, W. M. 2014, Science, 346, 61

[140] Madzunkov, S., Shortt, B. J., MacAskill, J. A., Darrach, M. R., & Chutjian, A. 2006, Phys. Rev. A, 73, 020901

[141] Martín-Doménech, R., Muñoz-Caro, G.-M., Bueno, J., & Goesmann, F. 2014, A&A, 564

[142] Martín-Doménech, R., Manzano-Santamaría, J., Muñoz Caro, G. M., et al. 2015, A&A, 1

[143] Mason, N. J., Dawes, A., Holtom, P. D., et al. 2006, Faraday Discuss., 133, 311

[144] McClure, M., Bailey, J., Beck, T., et al. 2017, IceAge: Chemical Evolution of Ices during Star Formation, JWST Proposal ID 1309. Cycle 0 Early Release Science

[145] McGuire, B. A., Burkhardt, A. M., Kalenskii, S., et al. 2018, Science, 359, 202

[146] McKellar, A. 1940, PASP, 52, 187

[147] Millar, T. J., Herbst, E., & Charnley, S. B. 1991, ApJ, 369, 147

[148] Miller, S. L. 1953, Science, 117, 528

[149] Miller, S. L., & Urey, H. C. 1959, Science, 130, 245

[150] Minissale, M., Dulieu, F., Cazaux, S., & Hocuk, S. 2016, A&A, 585

[151] Mispelaer, F., Theulé, P., Aouididi, H., et al. 2013, A&A, 555, A13

[152] Moore, M. H., & Husdon, R. L. 1992, ApJ, 401, 353

[153] Noble, J. A., Dulieu, F., Congiu, E., & Fraser, H. J. 2011, ApJ, 735, 121

[154] Noble, J. A., Congiu, E., Dulieu, F., & Fraser, H. J. 2012, MNRAS, 421, 768

[155] Noble, J. A., Fraser, H. J., Aikawa, Y., Pontoppidan, K. M., & Sakon, I. 2013, ApJ, 775, 85

[156] Nomura, H., & Millar, T. J. 2005, A&A, 438, 923

[157] Oba, Y., Watanabe, N., Kouchi, A., Hama, T., & Pirronello, V. 2010, ApJ, 712, L174

[158] Oba, Y., Watanabe, N., Kouchi, A., Hama, T., & Pirronello, V. 2011, PCCP, 13, 15792

[159] Oba, Y., Tomaru, T., Lamberts, T., Kouchi, A., & Watanabe, N. 2018, Nature Astronomy, 2, 228

[160] Öberg, K. I., van Broekhuizen, F., Fraser, H. J., et al. 2005, ApJL, 621, L33

[161] Öberg, K. I., Fraser, H. J., Boogert, A. C. A., et al. 2007, A&A, 462, 1187

[162] Öberg, K. I., Fayolle, E. C., Cuppen, H. M., van Dishoeck, E. F., & Linnartz, H. 2009, A&A, 505, 183

[163] Öberg, K. I., Garrod, R. T., van Dishoeck, E. F., & Linnartz, H. 2009, A&A, 504, 891

[164] Öberg, K. I., van Dishoeck, E. F., Linnartz, H., & Andersson, S. 2010, ApJ, 718, 832

[166] Öberg, K. I., Boogert, A. C. A., Pontoppidan, K. M., et al. 2011, ApJ, 740, 109

[166] Öberg, K. I., Murray-Clay, R., & Bergin, E. A. 2011, ApJL, 743, L16

[167] Öberg, K. I. 2016, Chem. Rev., 116, 9631

[168] Okabe, H. 1964, J. Opt. Soc. Am., 54, 478

[169] Okabe, H., & Lenzi, M. 1967, J. Chem. Phys., 47, 5241

[170] Okabe, H. 1978, Photochemistry of small molecules (John Wiley & Sons Inc.)

[171] Omont, A., Forveille, T., Moseley, S. H., et al. 1990, ApJL, 355, L27

[172] Ootsubo, T., Kawakita, H., Hamada, S., et al. 2012, ApJ, 752, 15

[173] Oro, J. 1961, Nature, 190, 389

[174] Ovchinnikov, M. A., & Wight, C. A. 1993, JChPh, 99, 3374

[175] Palumbo, M. E., & Baratta, G. A. 2000, A&A, 302, 298

[176] Pirronello, V., Biham, O., Liu, C., Shen, L., & Vidali, G. 1997, ApJL, 483, L131

[177] Pirronello, V., Liu, C., Shen, L., & Vidali, G. 1997, ApJL, 475, L69

[178] Pontoppidan, K. M., Fraser, H. J., Dartois, E., et al. 2003, A&A, 408, 981

[179] Pontoppidan, K. M. 2006, A&A, 453, L47

[180] Pontoppidan, K. M. M., Boogert, A. C. A. C. A., Fraser, H. J. J., et al. 2008, ApJ, 678, 1005

[181] Rajappan, M., Büttner, M., Cox, C., & Yates, J. T. 2010, J. Phys. Chem. A, 114, 3443

[182] Rajappan, M., Yuan, C., & Yates, J. T. 2011, J. Chem. Phys., 134, 064315

[183] Rideal, E. K. 1939, Mathematical Proceedings of the Cambridge Philosophical Society, 35, 130

[184] Romanzin, C., Gazeau, M.-C., Bénilan, Y., et al. 2005, Space Life Sciences: Astrobiology: Steps toward Origin of Life and Titan before Cassini, 36, 258

[185] Roser, J. E., Vidali, G., Manicò, G., & Pirronello, V. 2001, ApJL, 555, L61

[186] Roux, J. A., Wood, B. E., Smith, A. M., & Plyer, R. R. 1980, Arnold Engineering Development Center Int. Rep. AEDC-TR-79, Tech. rep., Arnold Air Force Base: AEDC

[187] Ruaud, M., Loison, J. C., Hickson, K. M., et al. 2015, MNRAS, 447, 4004

[188] Ruffle, D. P., & Herbst, E. 2000, MNRAS, 319, 837

[189] Ruffle, D. P., & Herbst, E. 2001, MNRAS, 322, 770

[190] Ruffle, D. P., & Herbst, E. 2001, MNRAS, 324, 1054

[191] Sandford, S. A., & Allamandola, L. J. 1990, ApJ, 355, 357

[192] Sandford, S. A., Allamandola, L. J., Tielens, A. G. G. M., & Valero, G. J. 1988, ApJ, 329, 498

[193] Satorre, M. ., Domingo, M., Millán, C., et al. 2008, Advances in Planetary Sciences: AOGS 2007, 56, 1748

[194] Schmidt, T. O. B., Neuhäuser, R., Briceño, C., et al. 2016, A&A, 593

[195] Schriever, R., Chergui, M., Kunz, H., Stepanenko, V., & Schwentner, N. 1989, The Journal of Chemical Physics, 91, 4128

[196] Schriever, R., Chergui, M., Ünal, ., Schwentner, N., & Stepanenko, V. 1990, J. Chem. Phys., 93, 3245

[197] Schriever, R., Chergui, M., & Schwentner, N. 1991, J. Phys. Chem., 95, 6124

[198] Schutte, W. A., Allamandola, L. J., & Sandford, S. A. 1993, Icarus, 104, 118

[199] Shen, C. J., Greenberg, J. M., Schutte, W. A., & van Dishoeck, E. F. 2004, A&A, 415, 203

[200] Shingledecker, C. N., Le Gal, R., & Herbst, E. 2017, Phys. Chem. Chem. Phys., 19, 11043

[201] Shimonishi, T., Onaka, T., Kato, D., et al. 2010, A&A, 514, 12

[202] Sievers, A. J., & Page, J. B. 1990, PhRvB, 41, 3455

[203] Slanger, T. G., & Black, G. 1978, J. Chem. Phys., 68, 1844

[204] Slanger, T. G., & Black, G. 1982, J. Chem. Phys., 77, 2432

[205] Slanger, T. G., Sharpless, R. L., Black, G., & Filseth, S. V. 1974, The J. Chem. Phys., 61, 5022

[206] Stief, L. J., Payne, W. A., & Klemm, R. B. 1975, J. Chem. Phys., 62, 4000

[207] Swings, P. & Rosenfeld, L. 1937, ApJ, 86, 483

[208] Taraschewski, M., Cammenga, H. K., Tuckermann, R., & Bauerecker, S. 2005, JPCA, 109, 3337

[209] Tarasova, E. I., Ratner, A. M., Stepanenko, V. M., et al. 1993, J. Chem. Phys., 98, 7786

[210] Teolis, B. D., Jones, G. H., Miles, P. F., et al. 2010, Science, 330, 1813

[211] Thiel, V., Belloche, A., Menten, K. M., Garrod, R. T., & Müller, H. S. P. 2017, A&A, 605

[212] Tielens, A. G. G. M., & Hagen, W. 1982, A&A, 114, 245

[213] Tielens, A. G. G. M. 2005, The Physics and Chemistry of the Interstellar Medium (Cambridge: Cambridge University Press), doi:10.1017/cbo9780511819056

[214] Tobin, J. J., Hartmann, L., Calvet, N., & D'Alessio, P. 2008, ApJ, 679, 1364

[215] Townes, C. H. 2006, in Astronomical Society of the Pacific Conference Series, Vol. 356, Revealing the Molecular Universe: One Antenna is Never Enough, Ed. D. C. Backer, J. M. Moran, & J. L. Turner, 81

[216] Tsegaw, Y. A., Góbi, S., Förstel, M., et al. 2017, J. Phys. Chem. A, 121, 7477

[217] van Broekhuizen, A., F., Groot, I. M. N., et al. 2006, A&A, 451, 723

[218] van de Hulst, H. C. 1948, Harvard Observatory Monographs, 7, 73

[219] van Dishoeck, E. F., Helmich, F. P., de Graauw, T., et al. 1996, A&A, 315, L349

[220] van Dishoeck, Ewine, F., & Blake, G. A. 1998, Annu. Rev. Astron. Astrophys., 36, 317

[221] van Dishoeck, Ewine, F., Jonkheid, B., & van Hemert, M. C. 2006, Faraday Discuss., 133, 231

[222] van Dishoeck, Ewine, F., Herbst, E., & Neufeld, D. A. 2013, Chem. Rev., 113, 9043

[223] Walsh, C., Millar, T. J., Nomura, H., et al. 2014, A&A, 563

[224] Watanabe, N., Nagaoka, A., Shiraki, T., & Kouchi, A. 2004, ApJ, 616, 638

[225] Weinreb, S., Barrett, A. H., Meeks, M. L., & Henry, J. C. 1963, Nature, 200, 829

[226] Whalley, E. 1977, CaJCh, 55, 3429

[227] Whalley, E., & Klug, D. D. 1979, JChPh, 71, 1513

[228] White, D. W., Gerakines, P. A., Cook, A. M., & Whittet, D. C. B. 2009, ApJS, 180, 182

[229] Whittet, D. C. B., Gerakines, P. A., Tielens, A. G. G. M., et al. 1998, ApJL, 498, L159

[230] Whittet, D. C. B., Cook, A. M., Chiar, J. E., et al. 2009, ApJ, 695, 94

[231] Whittet, D. C. B., Goldsmith, P. F., & Pineda, J. L. 2010, ApJ, 720, 259

[232] Yoshino, K., Esmond, J. R., Sun, Y., et al. 1996, JQSRT, 55, 53

[233] Yates, J. T. 1985, in Methods in Experimental Physics, ed. R. L. Park & M. G. Lagally, Vol. 22 (Academic Press), 425–464

[234] Yuan, C., & Yates, J. T. 2013, J. Chem. Phys., 138, 154302

[235] Yuan, C., & John T. Yates, J. 2014, ApJ, 780, 8

[236] Yuan, C., Cooke, I. R., & Yates, J. T. 2014, ApJL, 791, L21

[237] Zhang, K., Bergin, E. A., Blake, G. A., Cleeves, L. I., & Schwarz, K. R. 2017, Nature Astronomy 1, 0130

[238] Zins, E.-L., Joshi, P. R., & Krim, L. 2011, ApJ, 738, 175

[239] Zubko, V., Dwek, E., & Arendt, R. G. 2004, The ApJSS, 152, 211